Titre: Title:	Ductile Fracture of 13% Cr-4% Ni Martensitic Stainless Steels Used in Hydraulic Turbine Welded Runners
Auteur: Author:	Fayaz Foroozmehr
Date:	2017
Type:	Mémoire ou thèse / Dissertation or Thesis
Référence: Citation:	Foroozmehr, F. (2017). Ductile Fracture of 13% Cr-4% Ni Martensitic Stainless Steels Used in Hydraulic Turbine Welded Runners [Mémoire de maîtrise, École Polytechnique de Montréal]. PolyPublie. https://publications.polymtl.ca/2770/

URL de PolyPublie: PolyPublie URL:	https://publications.polymtl.ca/2770/
Directeurs de recherche: Advisors:	Yves Verreman, Denis Thibault, & Philippe Bocher
Programme: Program:	Génie métallurgique

UNIVERSITÉ DE MONTRÉAL

DUCTILE FRACTURE OF 13% CR-4% NI MARTENSITIC STAINLESS STEELS USED IN HYDRAULIC TURBINE WELDED RUNNERS

FAYAZ FOROOZMEHR

DÉPARTEMENT DE GÉNIE MÉCANIQUE

ÉCOLE POLYTECHNIQUE DE MONTRÉAL

MÉMOIRE PRÉSENTÉ EN VUE DE L'OBTENTION

DU DIPLÔME DE MAÎTRISE ÈS SCIENCES APPLIQUÉES

(GÉNIE MÉTALLURGIQUE)

FÉVRIER 2017

UNIVERSITÉ DE MONTRÉAL

ÉCOLE POLYTECHNIQUE DE MONTRÉAL

Ce mémoire intitulé :

DUCTILE FRACTURE OF 13% CR-4% NI MARTENSITIC STAINLESS STEELS USED IN HYDRAULIC TURBINE WELDED RUNNERS

présenté par : FOROOZMEHR Fayaz

en vue de l'obtention du diplôme de : Maîtrise ès sciences appliquées

a été dûment accepté par le jury d'examen constitué de :

Mme BROCHU Myriam, Ph. D., présidente

M. VERREMAN Yves, Ph. D., membre et directeur de recherche

M. THIBAULT Denis, Ph. D., membre et codirecteur de recherche

M. BOCHER Philippe, Ph. D., membre et codirecteur de recherche

M. CHEN Jianqiang, Ph. D., membre

M. BRAIDY Nadi, Ph. D., membre externe

DÉDICACE

A mes parents Mohammad et Farzaneh.

REMERCIEMENTS

En premier lieu, je dois remercier mon directeur de recherche, Prof. Yves Verreman, qui m'a fait confiance et m'a accepté au sein de son groupe de recherche. Je le remercie encore pour sa bienveillance, sa générosité, ses encouragements, ses conseils très précieux, et en un mot sa direction globale de la thèse. Je salue ici Dr. Jianqiang Chen qui m'a beaucoup aidé à réaliser mes essais mécaniques, surtout à mettre au point de l'essai J_{Ic}, et à dépouiller les données brutes. Sans lui, j'aurais perdu beaucoup de temps à réaliser mon premier essai J_{Ic}.

Je tiens à remercier mes codirecteurs, Prof. Philippe Bocher de l'École de la Technologie Supérieur (ÉTS) et Dr. Denis Thibault de l'Institut de Recherche d'Hydro-Québec (IREQ), pour les conseils métallurgiques très précieux et l'aide à interpréter les résultats fractographiques.

Je remercie Prof. Myriam Brochu de l'École Polytechnique de Montréal, pour sa coopération, sa gentillesse, et ses conseils très importants.

Je tiens à remercier Michel Sabourin et Benoît Papillon d'Alstom-Hydro, pour leur soutien technique et nous faire parvenir les informations importantes du côté pratique.

Je remercie Josée Laviolette, technicienne à l'École Polytechnique de Montréal, Étienne Dallaire, Manon Provencher, Marie-Andrée Ayotte, Alexandre Lapointe, et Carlo Baillargeon techniciens à l'IREQ, pour leurs soutiens techniques. Je salue ici Mathieu Paquin pour la fabrication de mon bloc de métal d'apport d'une qualité exceptionnelle.

Je remercie aussi Dr. Jacques Lanteigne de l'IREQ, pour nous faire parvenir ses expériences techniques et métallurgiques, surtout à propos de l'essai J_{Ic}.

Le soutien financier apporté par CRSNG, Hydro-Québec et Alstom-Hydro est remercié chaleureusement.

J'exprime ma plus profonde reconnaissance envers mes parents, Mohammad et Farzaneh, et mes sœurs, Foza et Foozieh pour leur soutien moral et financier au cours de mes études doctorales.

RÉSUMÉ

Les aciers inoxydables martensitiques 13% Cr-4% Ni sont largement utilisé dans la fabrication des roues de turbine hydrauliques grâce à leurs bonne résistance contre corrosion et érosion par cavitation, ainsi que leurs excellentes propriétés mécaniques. Les versions coulée et corroyée de ces aciers sont utilisées, et les procédés de fabrication et réparations sont réalisés par soudage. D'un autre côté, l'existence des fissures de fatigue dans les pièces sous charges cycliques est inévitable. Quand la fissure a atteint une longueur critique, elle se propage et la rupture totale de la pièce en service pourrait avoir lieu. Les défaillances catastrophiques pourraient être inhibées et la durée de vie de la roue de turbine hydraulique pourrait être améliorée si cette longueur critique de la fissure est connue (tolérance aux dommages). Mécanique de la rupture nous permet de calculer cette longueur critique de la fissure en déterminant une propreté intrinsèque du matériau intitulée « ténacité ». Donc, la ténacité est une propriété très importante à considérer dans le choix des matériaux.

Toutefois, la ténacité des aciers inoxydables martensitiques 13% Cr-4% Ni restait encore inexplorée. Des relations entre microstructure et propriétés mécaniques de ces aciers ne sont pas assez connues, et aucune étude exhaustive n'a été rapportée jusqu'à présent sur des effets des caractéristiques microstructurales comprise la distribution, la taille, et la nature des inclusions sur les propriétés mécaniques des aciers inoxydables martensitiques 13% Cr-4% Ni notamment pour les versions coulée, corroyée, et le métal d'apport. D'ailleurs, la zone affectée thermiquement (ZAT) est supposée d'être une source de faiblesse dans un joint soudé, cependant, son comportement à rupture n'a pas encore été étudié pour cette catégorie d'aciers inoxydables.

Dans cette étude, les microstructures et les propriétés mécaniques d'une version coulé, une version corroyée, et la soudure des aciers inoxydables martensitiques 13% Cr-4% Ni ont été étudiées. Les microstructures et les caractéristiques inclusionnaires étaient liées à des propriétés à la traction, à la ténacité J_{Ic}, et à la résiliences Charpy. Des essais de ténacités J_{Ic} ont également été effectués dans la ZAT à une distance d'un millimètre de la ligne de fusion.

Un bloc de rechargement de 450 × 250 × 60 mm a été fabriqué par soudage semi-automatique à l'arc avec fil fourré (procédé FCAW). La soudure déposée a été examinée dans les deux états de brut de soudage, et thermiquement traité à 600 °C pour deux heures. La densité surfacique, la

fraction volumique et la taille des inclusions, ainsi que l'espacement inclusionnaire ont été mesurés sur les sections métallographiques par microscopie optique, tandis que la taille des inclusions a été également mesurée par MEB. Les pourcentages d'austénite ont été mesurés sur les sections métallographiques par la diffraction des rayons X. En cas de l'acier corroyé, les pourcentages d'austénite ont été également mesurés en dessous du faciès de rupture J_{Ic} aux différentes épaisseurs. Les faciès de ruptures ont été examinés par la microscopie électronique à balayage (MEB), et la nature des inclusions a été déterminée par spectroscopie de rayons X à dispersion d'énergie.

L'acier corroyé a la meilleure combinaison de la résistance-ductilité/ténacité à la température ambiante. De plus, les plus hautes valeurs de ductilité à la rupture, la ténacité J_{Ic}, et la résilience Charpy ont été obtenues pour cet acier. La ténacité J_{Ic}, et la résilience Charpy des métaux de base ont été au moins cinq fois, et trois fois plus hautes que celles des métaux d'apport, respectivement.

La rupture est survenue de façon ductile pour les essais effectués à la température ambiante en cas des métaux de base et des métaux d'apport. L'amorçage prématuré des micro-vides sur les inclusions grossières ainsi que sur celles brisées a été la raison principale qui explique les plus faibles propriétés mécaniques (ductilité, ténacité J_{Ic}, et résilience Charpy) de l'acier coulé par rapport à l'acier corroyé. De l'autre côté, la formation des micro-vides sur les petites inclusions retarde la rupture jusqu'à ce que des déformations plus importantes atteignent ; ce qui augmente l'élongation à la rupture, la ténacité J_{Ic}, et la résilience Charpy. Par contre, les sites d'amorçages des micro-vides sont tellement nombreux en cas des métaux d'apport que la croissance des micro-vides est limitée par la coalescence, et bien moins d'énergies de ruptures sont absorbées.

D'ailleurs, différents comportements de propagations de fissure ont été observés entre les métaux de base et les métaux d'apport : la courbe de résistance de J a été bien plus raide pour les métaux de base. Pour les métaux de base et les métaux d'apport, les valeurs de J continuent à accroître jusqu'au dernier point de données, cependant, par rapport à des métaux de base on peut dire qu'un quasi-palier a été atteint pour les métaux d'apport. De plus, malgré utiliser de plus grand l'ouverture à la pointe de la fissure (crack tip opening displacement) plus petites propagations de la fissure ont été lieu pendent l'essai J_{Ic} des matériaux de base.

Une corrélation entre la résilience Charpy et la ténacité K_{Ic} couvrant des larges gammes de résilience Charpy et de ténacité K_{Ic} a été proposée pour des aciers martensitiques 13% Cr-4% Ni.

En cas des essais J_{Ic} réalisés dans la ZAT, les valeurs candidates de la ténacité (K_Q) ont été seulement obtenues. La ténacité a été plus haute que celle des métaux d'apport, mais plus basse que celle des métaux de base. Dans la majorité des cas, des propagations instables vers la soudure (sous la ligne de fusion) ont été survenues juste après avoir lieu des propagations stables d'environ un millimètre. Le comportement de résistance à la propagation stable de la fissure dans la ZAT a été similaire de celui des matériaux d'apport.

ABSTRACT

13% Cr-4% Ni martensitic stainless steels are widely used in the manufacture of hydraulic turbine runners due to their good resistance against corrosion and cavitation erosion, and high mechanical properties. Both cast and wrought versions of these steels are used, and the fabrication and repair processes are performed by welding. On the other hand, the existence of fatigue cracks in components under cyclic loading is inevitable. The propagation occurs if the crack length reaches a critical value, and a total breakdown of the in-operation component could take place. The catastrophic failures can be inhibited and the turbine runner lifetime can be improved if the critical crack length is known (damage tolerance). This critical crack length can be calculated by Fracture Mechanics defining an intrinsic property of the material entitled "fracture toughness". Therefore, fracture toughness is a very important property to be concerned.

However, fracture toughness of 13% Cr-4% Ni martensitic stainless steels still remains almost unexplored. The relations between the microstructure and mechanical properties of these steels are not well known as well, and no comprehensive investigation has been reported so far on the effects of the microstructural features including distribution, size, and types of inclusions on the mechanical properties of 13% Cr-4% Ni martensitic stainless steels, especially for the wrought version and the weld metal. Moreover, the heat affected zone (HAZ) is supposed to be a source of weakness in a welded joint, but its fracture behavior has not yet been studied for this category of stainless steels.

In this study, the microstructures and mechanical properties of a cast and a wrought 13% Cr-4% Ni martensitic stainless steels as well as those of their matching weld metal were studied. Microstructures and inclusion characteristics were related to tensile, fracture toughness J_{Ic}, and Charpy V-notch fracture energy. Fracture toughness J_{Ic} tests were also performed in the HAZ, one millimeter far from fusion line.

A semi-automatic flux cored arc welding process was used to fabricate a weld metal block of 450 × 250 × 60 mm. The deposited weld metal was tested in both as-welded and heat-treated conditions, and a heat treatment process at 600 °C for 2 hrs was used. The surface density, volume fraction, size and spacing of inclusions were measured on metallographic sections using optical microscopy, whereas the inclusion size was also measured using SEM. The austenite

contents were measured on metallographic sections using X-ray diffraction analysis. In the case of the wrought steel, the austenite contents were also measured on the ruptured J_{Ic} samples below the fracture surfaces at different depths. Fracture surfaces were examined by scanning electron microscopy, and inclusion types were determined by energy dispersive X-ray spectroscopy examinations.

The wrought steel showed the best combination of strength-ductility/fracture toughness at room temperature. In addition it had the highest ductility at fracture, fracture toughness J_{Ic} and Charpy V-notch (CVN) fracture energy. The fracture toughness J_{Ic}, and the CVN fracture energy of the base metals were at least five times, and three times higher than those of the weld metals, respectively.

Dimpled rupture occurred for the tests carried out at room temperature for both the base metals and the weld metals. Premature micro-voids nucleation on large inclusions as well as on ruptured ones was the main reason for the lower mechanical properties (ductility, fracture toughness J_{Ic}, and CVN fracture energy) of the cast steel as compared to the wrought one. On the other hand, the formation of micro-voids on small inclusions retards the fracture until higher strains are reached increasing the elongation at fracture, fracture toughness J_{Ic}, and CVN fracture energy. Inversely, micro-voids nucleation sites are so numerous in the weld metals that the growth of the nucleated micro-voids was limited by their premature coalescence and much less fracture energies are absorbed.

Moreover, different crack growth behaviors were observed between the base metals and the weld metals: the J resistance curve was much steeper for the base metals. The J values continue increasing until the last data point for the both steels, however, as compared to the base metals, it can be said that a quasi-plateau was reached for the weld metals. Additionally, despite using a larger crack tip opening displacement, smaller crack growths occurred during J_{Ic}-testing of the base metals.

A K_{Ic}-CVN correlation covering wide ranges of CVN fracture energy and fracture toughness K_{Ic} was proposed for 13% Cr-4% Ni martensitic stainless steels.

For the J_{Ic} tests carried out in the HAZ, candidate values of fracture toughness (K_Q) were only obtained. The fracture toughness was higher than that of the weld metals, but lower than that of

the base metals. In most cases, unstable crack propagation toward the weld metal occurred (beneath the fusion line) just after a stable crack growth of about one millimeter. The stable crack growth resistance behavior of the HAZ was similar to that of the weld metals.

TABLE OF CONTENTS

LIST OF TABLES

LIST OF FIGURES

LIST OF SYMBOLS

a	Crack length
a_0	Initial crack length
b_0	Initial ligament (W- a_0)
B	Total thickness of J_{Ic} specimen
B_N	Net thickness of J_{Ic} specimen (distance between roots of the side-grooves)
c_0	Inclusion size
E	Young's modulus
e_f	Elongation at fracture
e_u	Uniform elongation
f	Volume fraction of inclusions
$H(d)$	Harmonic mean value of inclusion diameters
J	Strain energy release rate
J_{el}	Elastic component of J
J_{Ic}	J-integral value at the initiation of stable crack growth
J_{pl}	Plastic component of J
J_Q	Candidate value of J_{Ic}
K	Stress intensity factor

K_{Ic}	Plane-strain fracture toughness
K_Q	Candidate value of K
P	Load
P_{max}	Maximum load
P_Q	Candidate value of load
R	Final radius of a spherical void
R_0	Initial radius of a spherical void
R^2	Coefficient of determination
S_T	Stress triaxiality
T	Tearing modulus
W	Width of J_{Ic} specimen

α	Stress concentration factor around an inclusion
β	Constant
γ	Austenite
γ_s	Surface energy
Δa_p	Physical crack extension
ΔK	Amplitude of stress intensity factor ($K_{max} - K_{min}$)
δ	Delta ferrite

ε	True strain in uniaxial tensile testing
ε_R	Plastic strain needed for growth of a spherical void
λ	Inclusion spacing
ν	Poisson ratio
0.2% σ_y	0.2% offset yield strength
σ_{UTS}	Tensile strength
σ_{void}	Required stress for void nucleation
σ_y	Yield strength
χ^2	Chi square

LIST OF ABBREVIATIONS

ACI	Alloy Casting Institute
ASTM	American Society for Testing and Materials
AW	As-Welded
AWS	American Welding Society
BCC	Body-Centered Cubic
BCT	Body-Centered Tetragonal
CReFaRRE	Consortium de Recherche en Fabrication et Réparation des Roues d'Eau (research consortium in manufacture and repair of the hydraulic turbine runners)

COD	Crack Opening Displacement
CT	Compact Tension
CVN	Charpy V-Notch
DBTT	Ductile-Brittle Transition Temperature
EDX	Energy Dispersive X-ray
ÉTS	École de Technologie Supérieure
FCAW	Flux-Cored Arc Welding
FCC	Face-Centered Cubic
FEM	Finite Element Modeling
HAZ	Heat Affected Zone
HCP	Hexagonal Close-Packed
HRC	Rockwell C Hardness
HT	Heat-Treated
IREQ	Institut de Recherche d'Hydro-Québec
J-R curve	J-Resistance curve
LEFM	Linear Elastic Fracture Mechanics
LPD	Load Point Displacement
M_s	The temperature at which martensite starts to form
MVC	Micro-Void Coalescence

NSERC	Natural Science and Engineering Research Council of Canada
RD	Rolling Direction
SEM	Scanning Electron Microscope
TD	Transverse Direction
TRIP	Transformation-Induced Plasticity
UNS	Unified Numbering System
WM	Weld Metal
XRD	X-Ray Diffraction

LIST OF APPENDICES

INTRODUCTION

Context

This project is one of the eights projects on the "Analysis of crack propagation in welded joints" in the CReFaRRE research consortium. These projects are supported by NSERC, Hydro-Québec, and Alstom Power Hydro. École Polytechnique de Montréal and ÉTS are the university partners, whereas IREQ, and Alstom Power Hydro are the industrial partners of this consortium. Cast (CA6NM), wrought (S41500), and filler metal (410NiMo) of 13% Cr-4% Ni martensitic stainless steels, as well as a low carbon content austenitic stainless steel (304L), and a carbon steel (A516) used in the fabrication of hydraulic turbine runners are used. Apart from the project defined for this thesis, the following topics are studied in these projects:

- Susceptibility to cold cracking during welding;
- Fatigue crack propagation in the base metal, in the HAZ, and in the weld metal;
- Influence of stress ratio, and tensile residual stress on the base metal resistance to fatigue crack propagation;
- Effect of different heat treatments, carbon content on the base metal resistance to fatigue crack propagation;
- Effect of constant and variable amplitude loading on fatigue crack propagation of the base metals determining the interaction between small and large loading cycles;
- Fatigue behavior of welded joints of partial penetration determining their fatigue life and comparing the crack growth with those predicted by Fracture Mechanics.

Mechanical properties of a material emanate from its microstructure. In other words, to study the mechanical properties of a material, its microstructural features have to be characterized first. Transformation-induced plasticity (TRIP) of the austenite is considered as an important mechanism improving the ductility, plane strain fracture toughness, and Charpy V-notch (CVN) fracture energy [1-3]. Inclusions play a very important role in ductile rupture. This is related to their content, size, distribution and nature in the microstructure [4-9].

Microscopic and macroscopic defects such as inclusions, and cracks resulting from fabrication process, especially in the case of a welding process, most often exist in an in-operation

component. If propagation occurs, these cracks reach a critical size and sudden break of the component takes place causing a lot of damage. Therefore, by knowing this critical crack size, catastrophic failures could be inhibited. This critical crack size can be obtained by Fracture Mechanics defining an intrinsic material property called “fracture toughness”. This important property is defined as the resistance of a material against unstable propagation of the sharpest possible notch, produced by fatigue cycling, in the presence of triaxial stresses. Accordingly, fracture toughness is a very important property to consider in the choice of materials, particularly for welded constructions.

Since measuring the plane strain fracture toughness involves a complex, time consuming and expensive procedure, especially in the case of fracture toughness J_{Ic}, there is a great interest to predict the plane strain fracture toughness using a much simpler test results commonly used in industry: the “Charpy impact test”. This test compares the fracture behavior of materials against a sudden break in the presence of triaxial stresses, however, the data cannot be used in Fracture Mechanics calculations.

Problematic

There is no complete database for mechanical properties of 13% Cr-4% Ni martensitic stainless steels and their welds in the literature, especially in the cases of fracture toughness J_{Ic} and CVN fracture energy of the wrought version and the weld metal deposited by flux-cored arc welding (FCAW) process. In addition, there is even less information about mechanical behavior of their heat affected zone (HAZ). Because of the complexity of its microstructure and its susceptibility to cold cracking in the presence of residual stresses, HAZ is suspected to be a source of weakness in welded joints [10]. Accordingly, performing fracture toughness tests in the HAZ along with that of the base metal and weld metal is of the great importance.

On the other hand, developing a K_{Ic}-CVN correlation for these martensitic stainless steels provides the opportunity to predict fracture toughness of the components after each heat treatment process by testing a small specimen which could be a help for quality control process.

General objectives

This thesis entitled “Ductile Fracture of 13% Cr-4% Ni Martensitic Stainless Steels Used in Hydraulic Turbine Welded Runners” is intended to provide an important data base of mechanical properties, especially in the case of fracture toughness, as well as microstructure-mechanical

properties relationships. In addition, proposing K_{Ic}-CVN correlations can be very useful for the industrial partners.

The Mechanical characterization of a cast and a wrought 13% Cr-4% Ni martensitic stainless steels, as well as a weld metal of the same chemical composition was the first objective of this project. To this purpose, tensile, fracture toughness J_{Ic} and CVN tests were performed to create an important data base for the basic mechanical properties of this grade of martensitic stainless steels. This is of great importance for both scientific and industrial sides. The second general objective was to find the relationships between microstructures/defect characteristics and the mechanical properties. This is a scientific objective, but it could be interesting for the industrial partners since it provides the opportunity for selecting materials of higher mechanical properties performing simple metallographic examinations.

Establishing a K_{Ic}-CVN correlation for both the base metals and the weld metals was the final objective of the industrial partners. Its main outgrowth is to have a precise idea about the fracture toughness just by performing a conventional CVN test saving a lot of time and hence, fast material selection.

Specific objectives

- Tensile, fracture toughness J_{Ic}, and CVN testing of a cast, and a wrought base metals in as-received condition (tempered), as well as a weld metal in both as-welded and heat-treated conditions to make systematic comparisons among these materials/ mechanical properties;
- Characterization of the microstructures and inclusion characteristics of the tested materials, and interpretation of their effects on tensile, fracture toughness J_{Ic}, and CVN fractures;
- Fractography of fracture surfaces in each case with attention paid to ductile fracture mechanism;
- Shedding light on different fracture mechanisms;
- XRD analysis of the phases present in the section perpendicular to J_{Ic} stable crack extension fracture surfaces (only base metals) to determine the TRIP effect region;
- Fracture toughness J_{Ic} testing with an initial fatigue crack close to the fusion surface.

Organization of the study

This thesis is organized into six chapters. A critical literature review is presented in the first chapter. A brief review on the formation, morphology, and strength of ferrous martensite is provided. Microstructure and mechanical properties of 13% Cr-4% Ni martensitic stainless steels are presented. Upper shelf K_{Ic}-CVN correlations are also discussed.

Materials tested in this study and experimental procedures are defined in the second chapter. A brief review on the base metals is given. Then, the weld metal block fabrication procedure using FCAW process is presented. The welding parameters and the semi-automatic welding procedure are described, and chemical compositions of the materials are provided. Afterwards, the experimental procedures are presented. First of all, metallographic examinations including inclusion characterization analyses are briefly described. Mechanical characterization procedures including tensile, fracture toughness $J_{Ic,}$ of the base metals and the weld metal, as well as those performed in the HAZ, and CVN tests are presented. Fractography and XRD analyses are described at the end of this chapter.

The results obtained on the base metals are collected in the third chapter. The microstructural and inclusion characteristics examinations are presented at first. Then, mechanical characterization and fractographic examinations are presented. This provides the opportunity to shed light on the effects of microstructural features on the mechanical properties. So, a detailed discussion on the microstructure/inclusion characteristics-mechanical properties relationships is provided afterward. These microstructural and mechanical findings are finally summarised in the "conclusions" section.

The fourth chapter addresses the weld metal characterization in terms of both microstructural and mechanical aspects. Results, discussion, and conclusions are presented in the same order than those of the third chapter.

A detailed discussion on all the results obtained in this study was provided in the fifth chapter. Briefly, the microstructural features, mechanical properties, and fracture surfaces of the base metals and those of the weld metal in both as-welded and heat-treated conditions are compared. Three relevant K_{Ic}-CVN correlations taken from the literature are compared and a new one is proposed for 13% Cr-4% Ni martensitic stainless steels. At the end of this chapter, results obtained from J_{Ic} tests performed in the HAZ close to the fusion boundary are also added.

Overall brief conclusions of all findings in this project are summarised in the final chapter. These conclusions could shed light on further researches that could be performed on 13% Cr-4% Ni martensitic stainless steels or similar materials.

CHAPTER 1 LITERATURE REVIEW

1.1 Microstructure of martensitic stainless steels

1.1.1 Martensitic transformation

Martensite forms undergoing a diffusionless transformation. In this kind of transformation, there is not enough time for diffusion of atoms and the transformation occurs by a so called “military” movement of all atoms in a distance of less than interatomic one (shear mechanism). The term “military” is used in contrast with the term “civilian” used for diffusional transformations. Shear mechanism could occur in all metals and alloys during cooling or heating if it takes place rapidly enough. During ferrous martensitic transformation, carbon atoms remain in solid solution occupying interstitial octahedral positions in iron BCC lattice structure. Therefore, a supersaturated solid solution of carbon atoms is formed. Solid solution carbon atoms expand uniformly the lattice parameter of austenite. However, this extension is not uniform in the case of a BCC structure. This leads to an increase in the lattice parameter in one direction (c) forming a BCT lattice structure. This torsion of the lattice parameter leads to a volume expansion of the transformed region [11, 12]. Effect of carbon content on lattice parameters of austenite and martensite phases are shown in Figure 1-1. As can be seen in this figure, the lattice “c” parameter is drastically increased by increasing the carbon content.

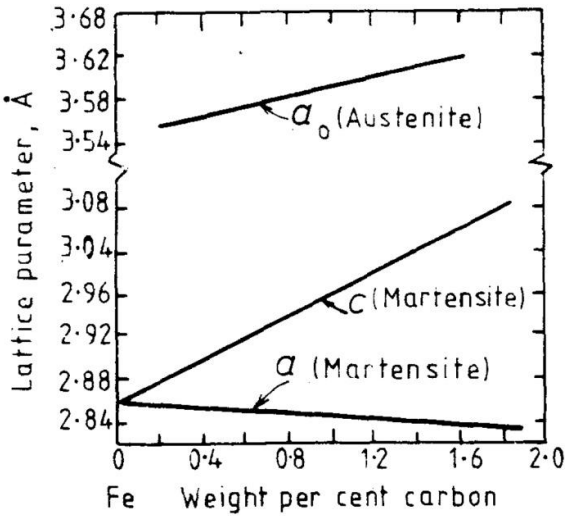

Figure 1-1: Effect of carbon content on lattice parameters of austenite and martensite [12]

The formation of martensite is complex, and it is not yet clearly understood. However, metallographic observations showed that the first martensite nuclei traverse along prior austenite grain (Figure 1-2). The martensite nuclei have a lens shape, and their density in an austenite grain seems to be independent of the grain size [12].

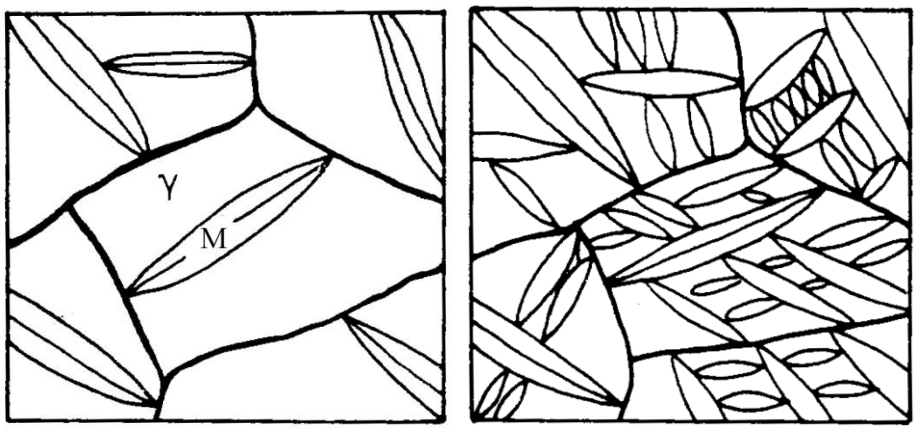

(a) (b)

Figure 1-2: Schematic representations of martensite formation: (a) the nucleus traverse along the prior austenite grain, (b) growth [12]

1.1.2 Effect of alloying elements

Cr: Chromium is the basic element in stainless steels. At least 10.5 wt% chromium is necessary to obtain a stainless steel. This minimum amount of chromium leads to the formation of a compact, adherent and protective layer of chromium oxide (Cr_2O_3) which separates steel from its environment preventing rust. Most martensitic stainless steels contain 12-14 wt% chromium which results in a lower corrosion resistance comparing with other grades, especially austenitic stainless steels which contain 16-25 wt% chromium. On the other hand, most martensitic stainless steels have lower price than other stainless steel grades due to their relatively lower alloying elements content. Since the mechanical properties and corrosion resistance of these steels decrease at temperatures higher than 650 °C, martensitic stainless steels are typically used at lower temperatures [13]. Chromium forms carbides and nitrides such as $M_{23}C_6$, M_7C_3, $M_{23}(C, N)_6$ et Cr_2N, where M is a mix of chromium and some portions of iron and molybdenum. $M_{23}C_6$ is formed in all stainless steels, but M_7C_3 is not common. Chromium is a ferrite-promoting element [13].

Iron-chromium equilibrium phase diagram is considered the basic phase diagram for martensitic stainless steels (Figure 1-3). Ferrite is the dominant phase and austenite exists in a confined region called "gamma loop" where its chromium content doesn't exceed about 13%. Austenite transforms into ferrite during cooling under equilibrium conditions. However, under most cooling conditions (except furnace cooling), austenite transforms to martensite even in heavy sections. This is the basis of producing martensitic stainless steels. These steels are considered as air hardening, that is to say, air cooling from austenite is sufficient to produce martensite [13, 14].

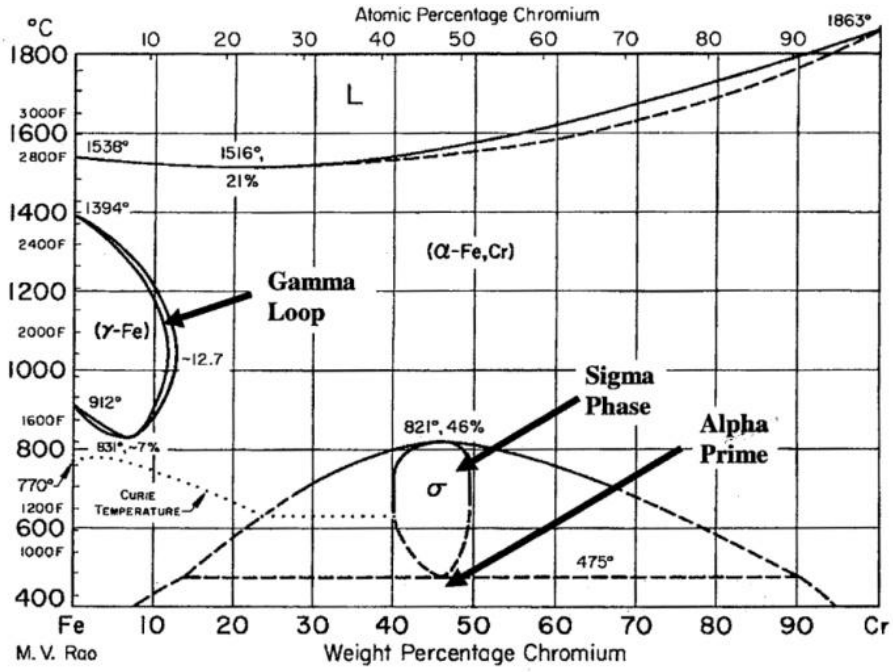

Figure 1-3: Iron-chromium equilibrium phase diagram [13]

C: The most important alloying element in steels is carbon [15]. In martensitic stainless steels, carbon forms $M_{23}C_6$ and M_7C_3 carbides. Hardness, and hence, susceptibility to cold cracking increase with carbon content. The maximum hardness of martensitic stainless steels containing less than 0.06% C, can reach up to 35 HRC. The hardness of steels for carbon contents between 0.06% and 0.3%, is in the range of 35-55 HRC. For carbon contents of exceeding 0.3%, the hardness will be between 55 and 65 HRC. Therefore, steels of the first category are less susceptible to cold cracking as compared to the two other groups.

Since carbon is a gamma-promoting element, its addition expands the austenite region of the Fe-Cr phase diagram. As shown in Figure 1-4, the nose of the gamma loop is expanded from 11% Cr to 21% Cr just by adding 0.036% C.

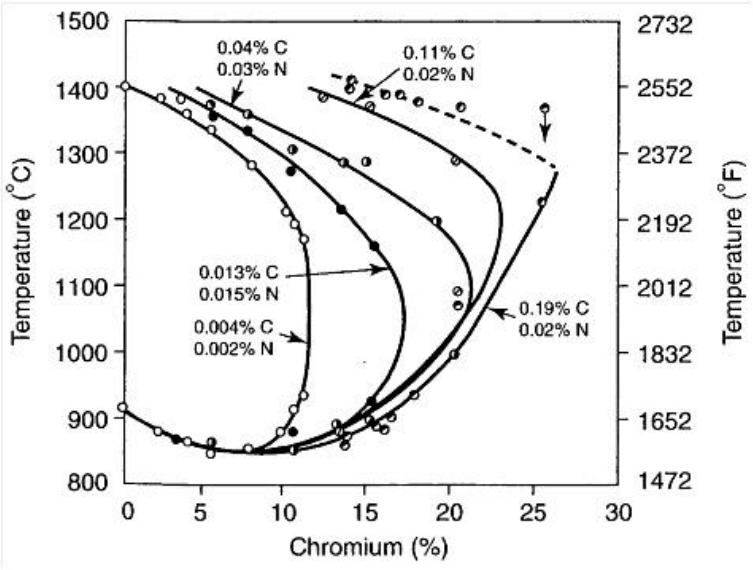

Figure 1-4: Effect of carbon on gamma loop expansion [13]

To examine the effect of carbon on Fe-Cr equilibrium phase diagram, Fe-Cr-C ternary systems for 13% Cr and 17% Cr are shown in Figures 1-5 (a) and (b), respectively. Note that in martensitic stainless steels, δ-ferrite has the same crystallographic structure as the α-ferrite (Body-Centered Cubic (BCC)), but it refers to iron crystals forming at high temperatures. As can be seen in Figure 1-5 (a), the extent of austenite is increased and ferrite stability domain is decreased. However, by increasing the chromium content in Figure 1-5 (b), the austenite domain is limited, but the ferrite domain is expanded. This is because chromium is a ferrite-promoting element stabilizing ferrite [13].

S: Sulfur forms low-melting point components segregating at grain boundaries. These components form liquid layers at grain boundaries causing an intergranular rupture during shrinkage in casting (hot shortness). Since martensitic stainless steels first solidify as delta ferrite and due to the good solubility of sulfur in delta ferrite, martensitic stainless steels are less susceptible to hot shortness than austenitic stainless steels [16]. However, low contents of sulfur improve machining, hot forming, and weldability of stainless steels. The extents of delta ferrite and austenite, as well as formation of intermetallic precipitations are not affected noticeably by low sulfur contents in Fe-Cr-Ni ternary system [15, 16].

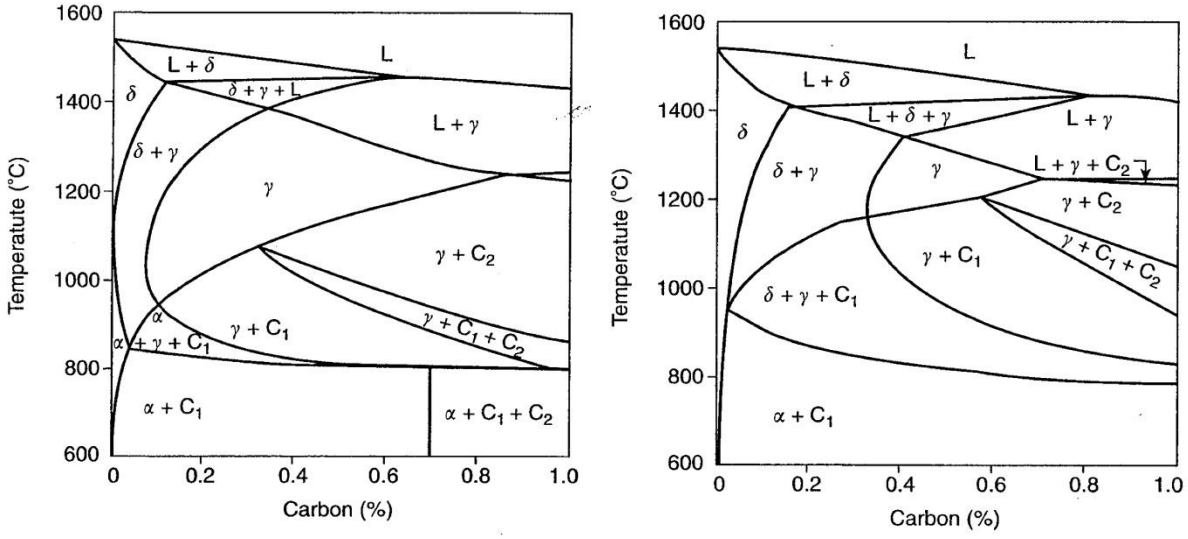

Figure 1-5: Fe-Cr-C ternary systems for (a) 13% Cr, and (b) 17% Cr [13]. C_1 and C_2 are $M_{23}C_6$ and M_7C_3 carbides, respectively

Mn: Generally, Mn is added to steels to prevent hot shortness by forming MnS (instead of iron sulfide). Mn is an austenite-promoting element. Its content in martensitic stainless steels is less than one percent [13, 16].

P: Phosphorus can form low melting point components with sulphides, silicides, and borides increasing the risk of hot shortness. However, this risk is negligible if phosphorus content is less than 0.025%. Phosphorus narrows the gamma loop [15].

Si: Silicon increases hot corrosion resistance of stainless steels. It is a ferrite-promoting element restricting the gamma loop. Silicon develops delta ferrite formation range and increase the sigma phase range. The formation of $M_{23}C_6$ carbides is facilitated by the presence of silicon. Fluidity of molten steel is improved by silicon and that is why silicon content of weld metal is sometimes higher than normal. Silicon forms intermetallic components such as FeSi, Fe_2Si Fe_3Si, Fe_5Si_3 and Cr_3Si segregating at grain boundaries causing structural embrittlement. In addition, silicon can increase the risk of hot shortness by forming low melting point components [13, 15, 16].

Ni: Nickel is a strong austenite-promoting element decreasing Ac_1 temperature (Table 1-1). Nickel improves toughness, but decreases the resistance against stress corrosion cracking (SCC). [13, 17].

Table 1-1: Effect of alloying elements on Ac_1 [17]

Alloying element	Ni	Mn	Co	Si	Mo	Al	V
Ac_1 change (°C) per wt%	-30	-25	-5	+25	+25	+30	+50

Mo: Molybdenum is a ferrite-promoting element and carbide former. It increases yield and tensile strengths at high temperature by secondary hardening [13].

N: Nitrogen is an austenite-promoting element extending the gamma loop; its effect on stabilizing the austenite is as important as the effect of carbon (Figure 1-4) [15]. In solid solution, it increases the strength of steel [13].

O: Oxygen forms non-metallic components, especially during welding, decreasing mechanical properties of stainless steels [15].

Cu: Copper is an austenite-promoting element. It improves corrosion resistance of stainless steels. Copper increases the strength of stainless steels by the formation of precipitates [13, 15].

1.1.3 13% Cr-4% Ni martensitic stainless steels

Basically, carbon and chromium are the main alloying elements of martensitic stainless steels. However, having high contents of carbon was the main reason for the majority of disadvantages of the chromium martensitic stainless steels such as poor weldability, susceptibility to cold cracking, and low toughness. As a result, in the late fifties a new generation of martensitic stainless steels with low contents of carbon entitled “soft martensitic stainless steels” was developed. Nickel was added to these alloys to remove the delta ferrite and improve toughness [13, 15]. However, most times, some supercooled delta ferrite remains along prior austenite grains; especially in the case of cast martensitic stainless steels. This is due to the segregation of ferrite-promoting elements during solidification stabilizing the delta ferrite at room temperature. Additionally, adding nickel stabilizes the gamma phase at lower temperatures.

Since the 1960s, different grades of soft martensitic stainless steels such as 13% Cr-1.5% Ni, 13% Cr-4% Ni, 16% Cr-6% Ni and 17% Cr-4% Ni have been produced [15]. Among these grades, 13% Cr-4% Ni is used to fabricate hydraulic turbine runners because of its good corrosion resistance, good resistance to cavitation erosion, excellent weldability, and good castability [2, 18, 19]. This steel is also used in compressor cones, pump bowls, and petrochemical industries [3]. Different phase stability zones of the stainless steel weld metals are

shown in Figure 1-6. As can be seen in this figure, the weld metal of 13% Cr-4% Ni martensitic stainless steels is located between fully martensite, and martensite and ferrite zones.

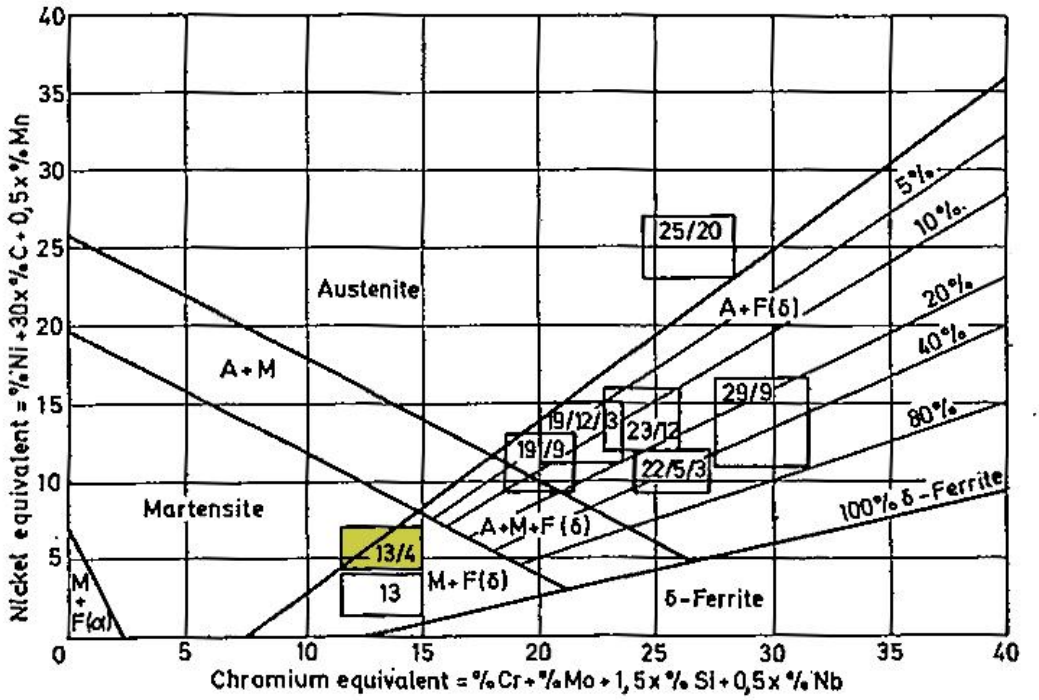

Figure 1-6: Shaeffler diagram showing different phase stability zones in terms of chromium equivalent and nickel equivalent for the weld metal of stainless steels (taken from [15]). Rectangular regions show various weld metals according to the percentages of Cr/Ni/Mo of the electrode types

Fe-Cr-Ni system for a Cr/Ni ratio of 3 is shown in Figure 1-7. The gamma loop is much more expanded comparing with the Fe-Cr system (Figure 1-3). The addition of 4% Ni resulted also to the decrease of Ac_1 temperature to about 631 °C for 13% Cr-4% Ni martensitic stainless steels.

In the as-quenched state, the microstructure of 13% Cr-4% Ni martensitic stainless steels is a combination of lath martensite and small amounts of delta ferrite. During subsequent tempering at around 600 °C, the martensite is partially transformed into stable austenite, forming a so-called "reformed austenite" phase. The reformed austenite is thermally stable even if the steel is quenched in liquid nitrogen (-196 °C) [3]. Tempering at higher temperatures would lead to the formation of thermally unstable austenite which would turn into fresh martensite during cooling [14, 15].

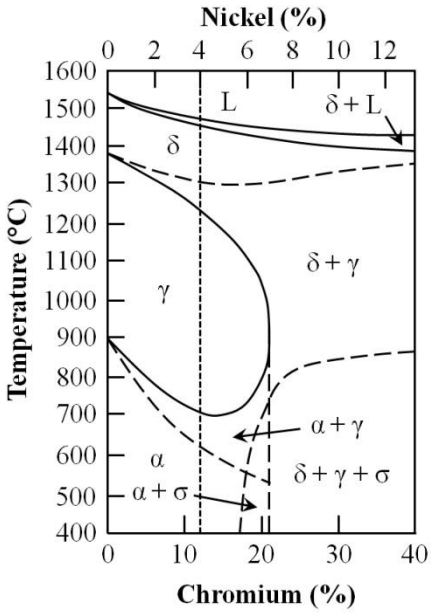

Figure 1-7: Phase diagram to study the Fe-Cr-Ni ternary system for a Cr/Ni ratio of 3 ([15])

1.2 Welding and post weld heat treatment of 13% Cr-4% Ni martensitic stainless steels

1.2.1 Welding

Hydraulic turbine runners components are usually assembled using flux-cored arc welding [20]. Schematic representation of FCAW process is shown in Figure 1-8. This is a self-shielding process; however, additional shielding gas can also be used. A flux cored tubular wire is used as a continuous consumable electrode whose the flux consists of materials providing self-shielding gases and slag, arc stabilizers, deposition rate enhancers, as well as alloying elements to improve the mechanical properties of the weld metal. This welding process is also referred as “open arc welding” since it is suitable for on-site welding due to the very good protection of the weld pool from the air by shielding gases generated from the flux-cored materials [21]. High weld metal quality under radiographic testing, high deposition rate, good appearance and smooth surface of the weld metal are other advantages of this welding process [22, 23]. Additionally, removal of the slag is fast and easy, and the welding process can be performed automatically [23, 24].

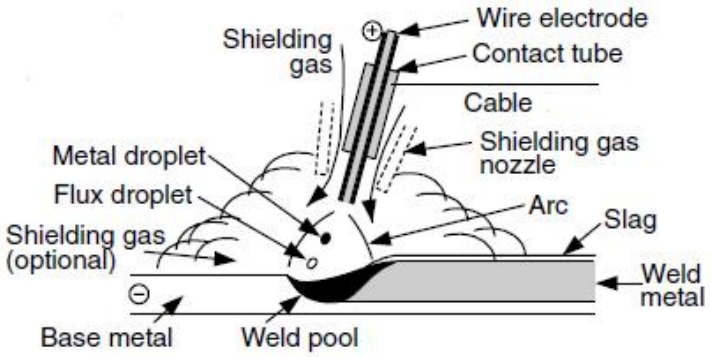

Figure 1-8: Schematic representation of FCAW process [25]

Nitrogen has deleterious effects on the mechanical properties of weld metal. Nitrogen forms sharp iron nitrides (Fe_4N) reducing severely the ductility. Therefore, Al, Ti, Zr, and Si are usually added to the flux-cored material to reduce nitrogen by forming nitrides. In addition, these elements also reduce oxygen content of the weld metal by forming oxides [25].

In the course of the welding process, the liquid solidifies as delta ferrite. Then, delta ferrite transforms into austenite, and finally austenite transforms into martensite during cooling to room temperature. At the end of the solidification, segregation of ferrite-promoting elements and/or austenite-promoting ones result in the formation of delta ferrite and/or retained austenite, respectively. Due to the concentration of the alloying elements, these phases are stable at room temperature.

Heat affected zone (HAZ) is of complex microstructures in 13% Cr-4% Ni stainless steels coming from various heat cycles applied to this region during welding procedure. HAZ regions regarding 13% Cr-4% Ni martensitic stainless steels constitutional diagram in terms of distance from fusion line is shown in Figure 1-9. Partial melting of primary delta ferrite occurs in a confined region just beside fusion line (zone (i)). A fully ferritic microstructure undergoing significant grain growth forms in zone (ii) due to the high-temperature applied to this region. Partial transformation of austenite to delta ferrite occurs in zone (iii). Zone (iv) is of a fully austenitic microstructure. Finally, tempered martensite partially transforms into austenite in zone (v) during heating [26-28].

1.2.2 Heat treatment

There are two general types of heat treatment processes for 13% Cr-4% Ni martensitic stainless steels: (i) conventional and (ii) double heat treatment. Note that these processes are used for both base and weld metals.

1.2.2.1 Conventional heat treatment and formation of reformed austenite

Conventional heat treatment process [29] of these steels consists of an austenitization at a minimum temperature of 1010 °C, quenching below 95 °C following by tempering between 565 °C and 620 °C (below A_{c1}). The tempering temperature has to be carefully chosen to obtain the best strength-ductility balance. During heat treatment, solid solution carbon atoms precipitate as carbides turning fresh martensite into tempered martensite. $M_{23}C_6$ and M_7C_6 are the most common carbides form in these alloys. The former has BCC lattice structure, and the latter has HCP one [30]. Therefore, the hardness and strength of the alloy decrease, and the ductility increases. In addition, austenite forms between martensite laths during this process [14, 30].

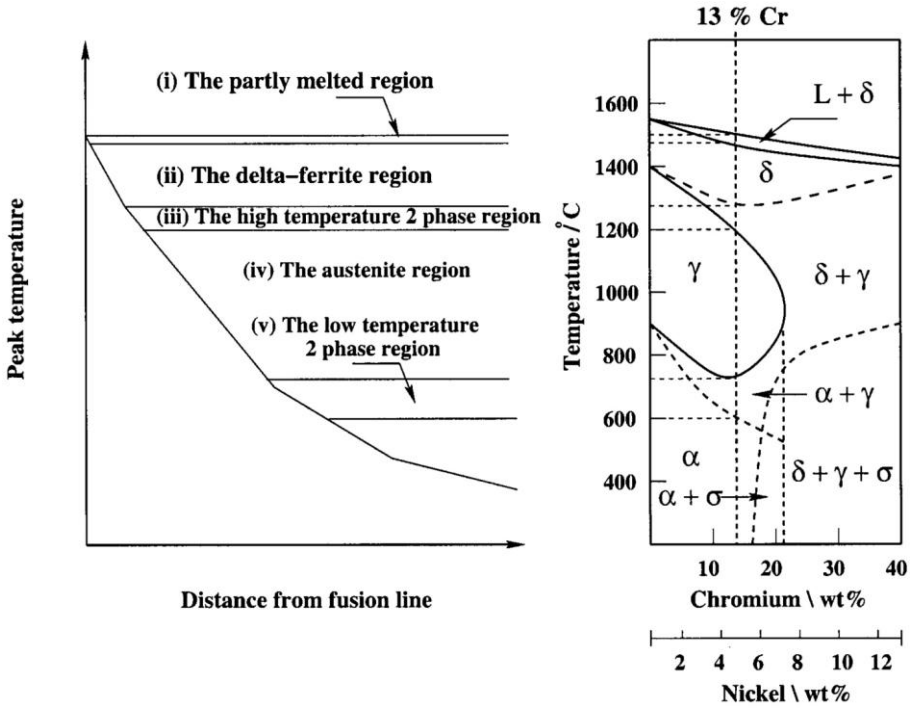

Figure 1-9: HAZ regions regarding 13% Cr-4% Ni martensitic stainless steels constitutional diagram [31]

One of the most important aspects of heat treatment of these alloys is the formation of austenite called “reformed austenite” which leads to the improvement of mechanical properties (see section 1.5.4). During tempering at around 570 °C up to about 630 °C [15], fine islets of reformed austenite form in prior austenite grain boundaries as well as between martensite laths [3, 19, 32]. The concentration of austenite-promoting elements, especially Ni, stabilizes the austenite until -196 °C [3]. Figures 1-10 (a) and (b) show reformed austenite in the wrought version (clear platelets), and in the weld metal (dark platelets) of 13% Cr-4% Ni stainless steels, respectively. As shown in (b), it can be clearly observed that the reformed austenite formed between martensite laths. The amount of reformed austenite depends on chemical composition of the alloy, and heat treatment process [15]. Note that the final amount of austenite measured using XRD is the total of retained austenite (from solidification), and reformed austenite (formed during tempering). Therefore, the term “austenite” is used to address the total amount of austenite (retained + reformed austenite) measured all over this thesis.

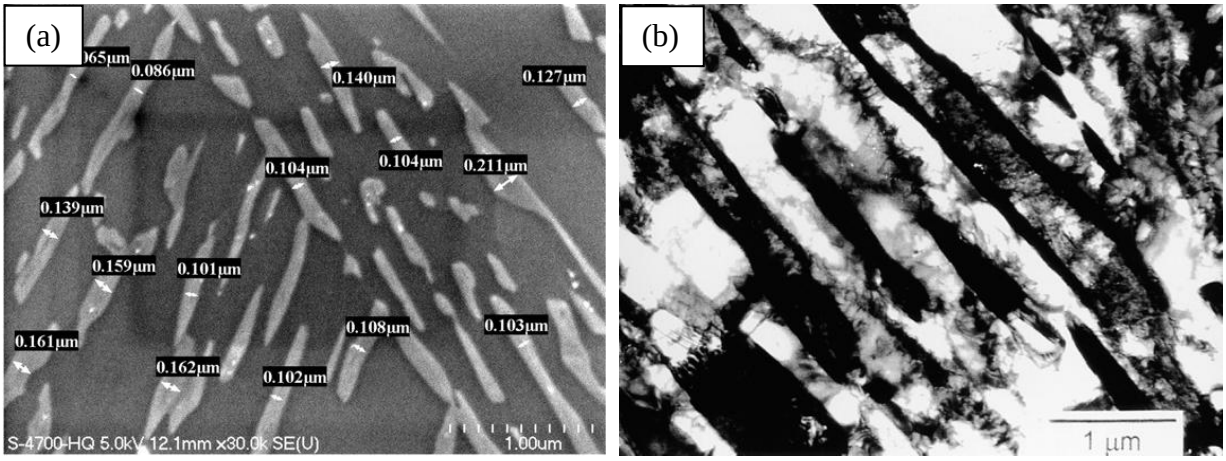

Figure 1-10: Reformed austenite in 13% Cr-4% Ni martensitic stainless steels: (a) SEM micrograph of 415 steel [19], and (b) TEM micrograph of 410NiMo steel [3]

There is an optimal tempering temperature to obtain the maximum possible reformed austenite. If the tempering process is performed at higher temperatures, higher reformed austenite contents will be re-transformed into martensite during cooling. A plot of percentage of austenite versus tempering temperature for a cast 13% Cr-4% Ni martensitic stainless steel is shown in Figure 1-11. The maximum amounts of austenite are obtained at 580 °C for both furnace cooled (23%) and water quenched (19%) specimens. Due to the lower cooling rate in the furnace, higher amounts of austenite were formed in this case (as compared to the water quenched specimen).

1.2.2.2 Double heat treatment

Obtaining the maximum possible amount of reformed austenite is provided by this process. A total austenite amount of 25% was obtained for the wrought version of 13% Cr-4% Ni martensitic stainless steels [33] using this heat treatment process. This kind of heat treatment consists of an initial tempering between Ac_1 and Ac_3, and a final one below Ac_1. By the first process, a considerable part of martensite transforms into reformed austenite, and the fresh martensite is tempered. However, part of this reformed austenite retransforms into fresh martensite during subsequent cooling. This fresh martensite is tempered by the final tempering process.

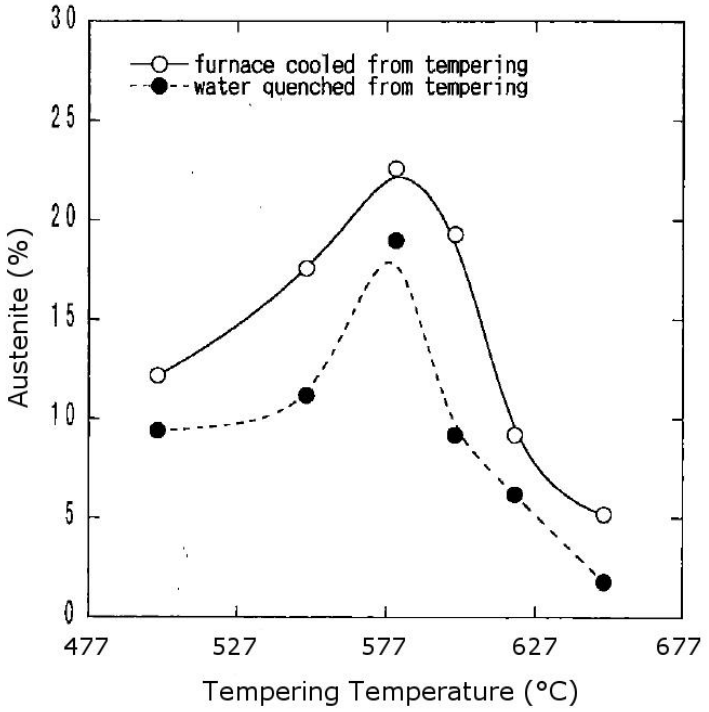

Figure 1-11: Percentage of austenite versus tempering temperature [34]

The following temperature ranges were proposed in ASTM A487/A487M [35] for double heat-treatment of 13% Cr-4% Ni stainless steels:

1- An intermediate tempering in a temperature range of 665 °C to 690 °C followed by quenching below 95 °C;

2- A final tempering in a temperature range of 565 °C to 620 °C followed by quenching below 95 °C.

1.3 Mechanical testing

1.3.1 CVN fracture energy

During Charpy V-notch (CVN) impact test, the energy absorbed by breaking a specimen with a V-shaped notch at its center is measured. This is a severe test having high rate of straining and high stress concentration at the tip of the V-notch. Schematic representations of a Charpy impact testing machine and a CVN specimen are shown in Figures 1-12 (a) and (b), respectively. The

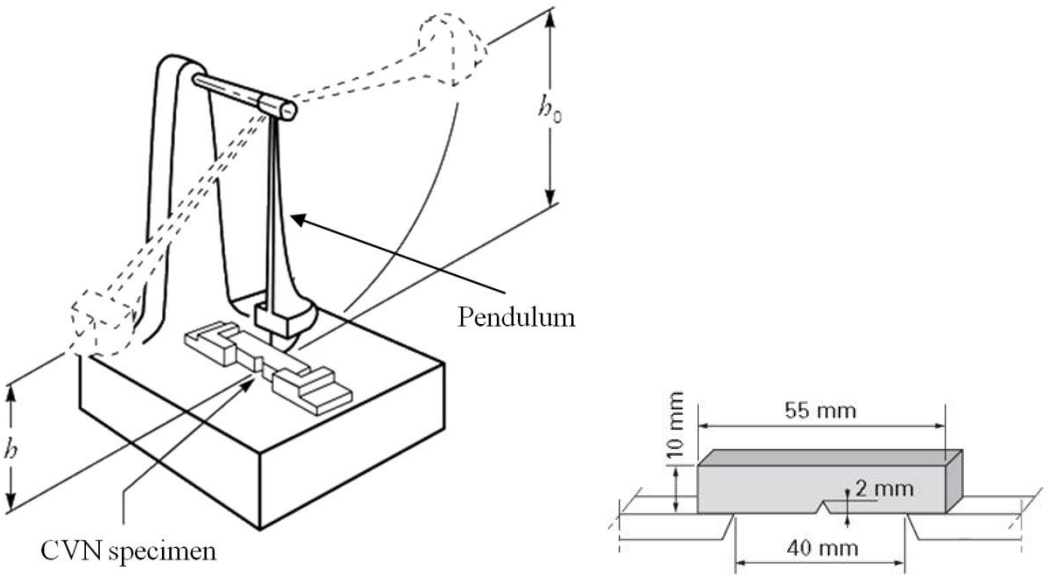

(a) (b)

Figure 1-12: Schematic representation of (a) Charpy impact testing machine [38], and (b) CVN specimen [37]

speed of the pendulum at the moment of impact is 5 to 5.5 m/s ($\dot{\varepsilon} = 10^3\ s^{-1}$) with maximum impact energy of 300 J. The V-notch specimen shown in (b) has an opening angle of 45 °, depth of 2 mm and a radius of curvature of 0.25 mm at its tip. The length, width and thickness of the specimen are 55 mm, 10 mm and 10 mm, respectively [36, 37].

A transition from ductile to brittle fractures occurs in the case of body-centered cubic (BCC) metals (Figure 1-13). This is related to the sensitivity of the Peierls-Nabarro force with the temperature in the BCC structure. However, the fracture mode doesn't change by decreasing the testing temperature in face centered cubic metals (FCC) metals. This is because in a FCC structure, there are various active slip systems even at low temperatures. Note that the ductile –

brittle transition temperature curve also does exist for hexagonal close packed (HCP) structures [39, 40].

The effect of carbon content on CVN fracture energy of carbon steels is shown in Figure 1-14. Ductile to brittle transition temperature decreases by decreasing the carbon content. Additionally, upper shelf CVN fracture energy increases by decreasing the carbon content. As can be seen in

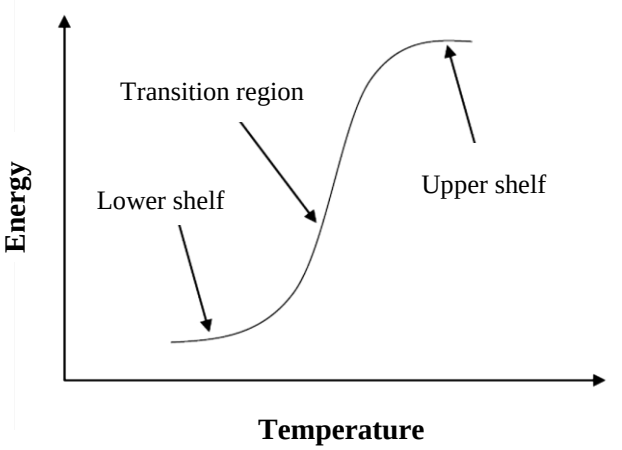

Figure 1-13 : Typical Charpy ductile-brittle transition curve of a BCC metal

this figure, martensitic stainless steels have low ductile to brittle transition temperature and high upper shelf CVN fracture energy.

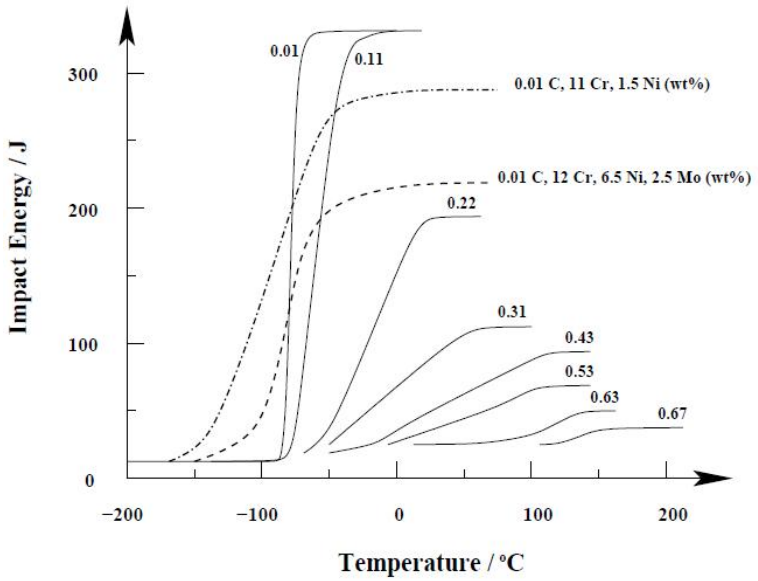

Figure 1-14: Effect of carbon content on CVN ductile-brittle transition curve of carbon steels; results of two martensitic stainless steels are also added (dashed lines) [26]

The Charpy impact test is a quick test commonly used in industry. However, the Charpy fracture energy is not an intrinsic property of the material, and it is just used to compare the fracture behavior of different materials and/or that of a material with respect to the temperature. Therefore, the Charpy fracture energy cannot be used for Fracture Mechanics calculations of in-operation components with sharp fatigue cracks. Accordingly, Fracture Mechanics provides a characteristic fracture property of materials entitled "fracture toughness K_{Ic}" described in the following section.

1.3.2 Fracture toughness K_{Ic}

Linear Elastic Fracture Mechanics (LEFM) describes the stress singularity at the tip of a sharp crack defining the stress intensity factor, K. Sudden crack propagation occurs when K reaches a critical value, K_c. This critical value of the stress intensity factor is considered as a material constant, "fracture toughness K_{Ic}", if the state of the stress at the crack tip is triaxial (plane strain state) and if the size of the crack tip plastic zone is small enough as compared to the dimensions of the specimen. However, in the case of ductile materials, using small laboratory specimens leads to significant plastic deformations and hence, LEFM approach is no longer applicable. In this case, the fracture parameter is defined as the release rate of the strain energy, J. Since sudden crack propagation does not occur in elastic-plastic condition, the critical value of the energy release rate, J_{Ic}, is defined at the initiation of stable crack propagation under plane strain condition. This initiation fracture toughness can be transformed to K_{Ic} using the following equation:

$$J_{Ic} = (1-\nu^2)\frac{K_{Ic}^2}{E} \tag{1-1}$$

where ν is Poisson ratio and E is Young's modulus.

1.3.3 Fracture toughness J_{Ic} measurement

Fracture toughness J_{Ic} testing procedures described in this section is in accordance with ASTM E1820 [41]. Much more details are given in the standard. Relative dimensions of a CT specimen for J_{Ic} test according to ASTM E1820 are shown in Figure 1-15. The standard proposes fatigue

pre-cracking to a total length between 0.45 W and 0.7 W at the bottom of the machined notch to create the sharpest possible notch creating minimum deformation.

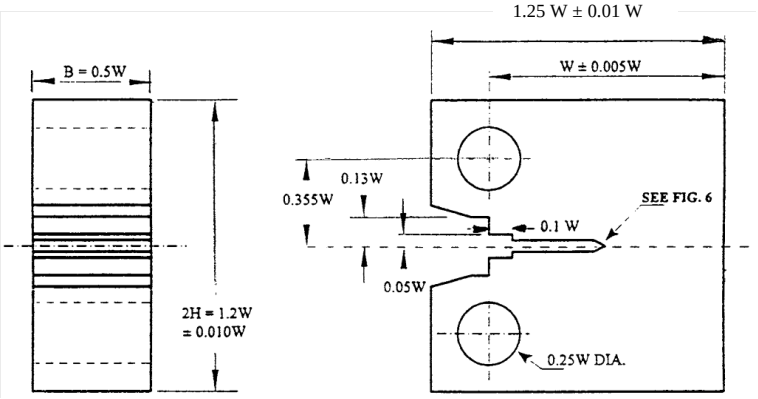

Figure 1-15: Relative dimensions of CT specimen for J_{Ic} testing according to ASTM E1820 [41]

Since direct measurement of crack extension is nearly impossible during the J_{Ic}-test, ASTM E1820 [41] proposes the use of compliance method. According to this method, crack extension is measured by means of partial unloading during registration of load, P, in terms of displacement, v. An example of force – displacement curve of a J_{Ic} test using the compliance method is shown in Figure 1-16. The lines no. 1 to no. 8 were produced during partial unloading and reloading. Their inverse slopes are defined as "compliance" (the slope is the stiffness of the specimen). The slope of these lines decreases as the crack propagates (the stiffness of the material decreases) and hence, the compliance increases. To plot the J-R curve and determine a candidate value of J_{Ic}, J_Q, the corresponding crack length and J value must be calculated for each partial unloading. Finally, after a crack advancement of about 2 – 3 mm, the J_{Ic}-test is finished, and the crack should be marked by heat tinting or fatigue cycling to measure the total crack size, and determine the state of stress (stress triaxiality) on its tip. Both initial and final crack lengths have to be measured at 9 equally spaced points on fracture surface.

To obtain the crack resistance curve, J vs. Δa, also called the J-R curve, J values are calculated for each crack extension, Δ*a*. The following equations are used to calculate J for each crack extension:

$$J = J_{el(i)} + J_{pl(i)} \tag{1-2}$$

where J_{el} and J_{pl} are the elastic, and plastic components of J, respectively,

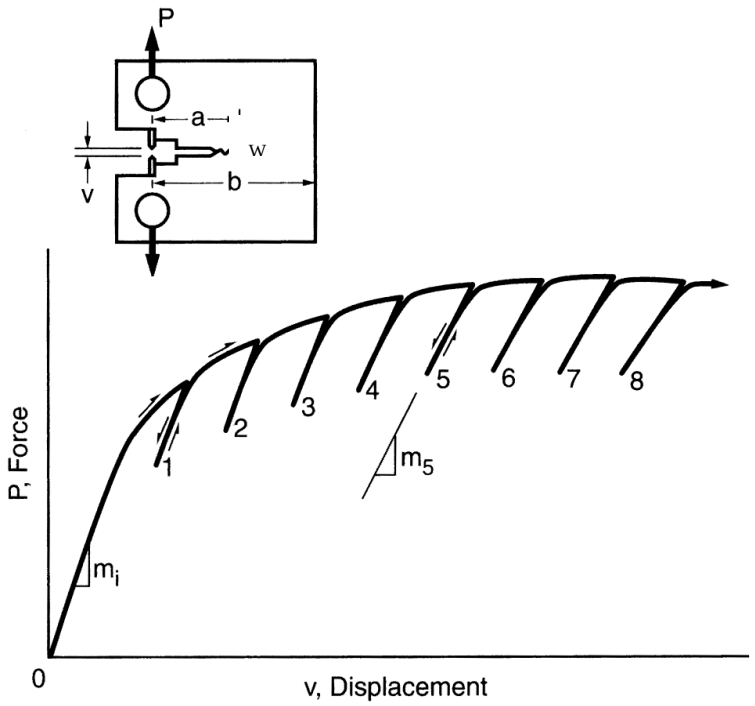

Figure 1-16: Force – displacement curve with partial unloadings during a J_{Ic} test [36]

and:

$$J_{el} = (1-\nu^2)\frac{K^2}{E} \tag{1-3}$$

where,

$$K = \frac{F}{(BB_N W)^{0.5}} f\left(\frac{a}{w}\right) \tag{1-4}$$

where, $f\left(\frac{a}{W}\right)$ is a geometry function, B_N is the net thickness for side-grooved specimens (distance between the roots of side grooves), and:

$$J_{pl} = \frac{\eta_{pl} A_{pl}}{B_N b_0} \tag{1-5}$$

where, $\eta_{pl\ (i-1)} = 2 + 0.522 b_{(i-1)}/W$, A_{pl} is the corresponding crack propagation area under force-displacement curve as shown in Figure 1-17, and b_0 is the initial ligament (W-a_0).

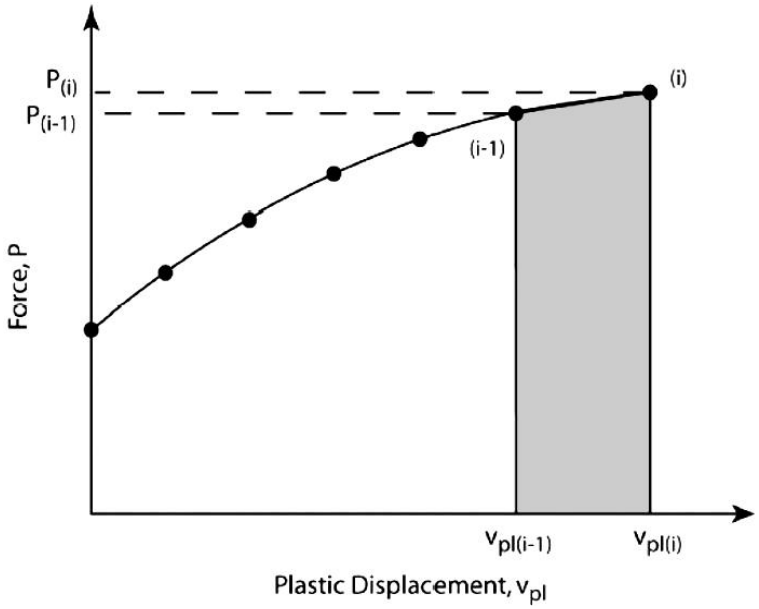

Figure 1-17: A_{pl} in resistance curve method [41]

The resistance of material against stable crack propagation is developed in J_{Ic} testing. The fracture toughness J_{Ic} is then determined at the onset of the stable crack propagation. A typical representation of J-R curve is shown in Figure 1-18. The following equation is used to construct the "blunting line" that represents the apparent crack advance only due to the plastic blunting at the crack tip:

$$J = 2\sigma_Y \Delta a \tag{1-6}$$

where:

$$\sigma_Y = \frac{\sigma_y + \sigma_{UTS}}{2} \tag{1-7}$$

and σ_y, and σ_{UTS} are the yield and the tensile strengths, respectively, obtained from uniaxial tensile test. Two parallel lines, called "exclusion lines" are drawn at 0.15 mm and 1.5 mm from the blunting line. A power law regression formula, $J = C_1 \Delta a^{C_2}$, is used to draw the J resistance

curve (J-R curve). Only the data points intercepted between the 0.15 mm and 1.5 mm exclusion lines are collected for this purpose (at least, five data points must be located between these exclusion lines). Intersection of the J-R curve and the offset line at 0.2 mm determines a candidate value of fracture toughness, J_Q.

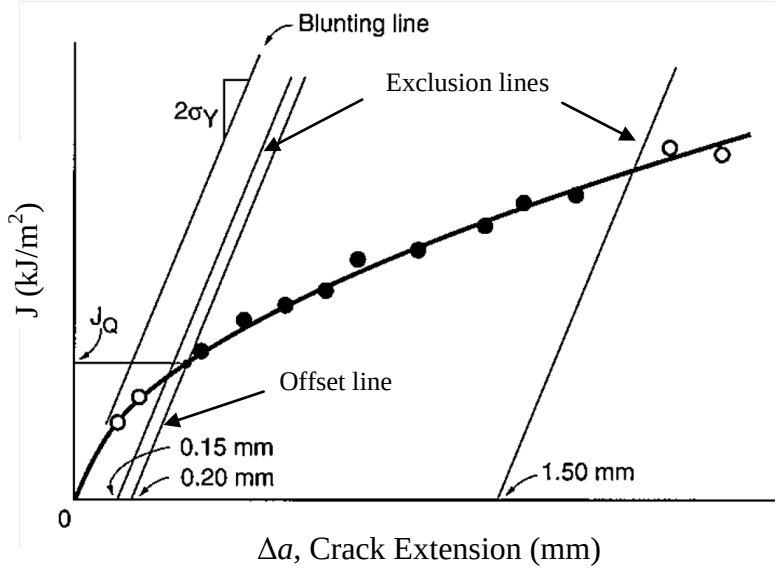

Figure 1-18 : Typical representation of J-R curve from a J_{Ic} test [36]

In order to qualify the measured J_Q as the fracture toughness J_{Ic}, the straightness requirements must be satisfied for both initial and final crack fronts. The difference between the predicted crack extension and the measured one must be less than $0.15\ \Delta a_p$. In addition, the two following conditions must also be satisfied:

$$B,(W-a_0)\rangle 10\left(\frac{J_Q}{\sigma_Y}\right) \tag{1-8}$$

The ASTM qualification requirements are described in detail in [41].

However, since J_{Ic} is a measure of fracture toughness at initiation of stable crack growth in ductile behaviors, the entire resistance of a material against stable crack propagation cannot be explained by this initiation fracture toughness. Accordingly, a more appropriate criterion explaining the resistance of a ductile material against stable crack growth, entitled “tearing modulus”, was defined for this purpose [6]:

$$T=\frac{E}{\sigma_y^2}\frac{dJ}{da} \tag{1-9}$$

The tearing modulus is a dimensionless criterion which is related directly to the slope of the resistance curve.

1.4 Fractography of ductile and brittle fractures

Ductile, cleavage, and intergranular fractures are the three main modes of fracture in metals. Microvoids formation on inclusions, cleavage crack propagation through grains (transgranular fracture), and crack propagation along grain boundaries (intergranular fracture) are schematized in Figures 1-19 (a), (b), and (c), respectively. These fracture modes are discussed in detail in the following sections.

1.4.1 Ductile fracture

Ductile rupture also called “dimpled rupture” occurs by the coalescence of micro-voids (Figure 1-20). This fracture mechanism entitled “micro-void coalescence (MVC)” starts by the nucleation of micro-voids continuing by the growth, and finally the coalescence of these voids as strain increases. Among these three steps, micro-void nucleation is the main one controlling ductile rupture. If it occurs in low numbers, important micro-voids growth will take place. If it occurs in large numbers, a premature coalescence will take place and the growth stage could be neglected [5]. Second phase particles and mainly non-metallic inclusions are the principal source of micro-void formation (Figure 1-20).

Investigations made by Rogers [42] showed that during tensile test, initial micro-voids formed at the center of the necked region. The coalescence of some of these micro-voids forms a crack. In some cases, this original crack propagates into slip planes forming angles of about 40° with the loading axis. This is the basis of the formation of void sheets. Micro-voids form into the deformed region (Figure 1-21 (a)), and the original crack propagates through these so called“void sheets” by splitting them up (Figure 1-21 (b)) [43]. As shown in Figure 1-22 (a), cup-cone fracture appearance is the result of the formation of two large void sheets at the final stage of tensile test. The cup-cone fracture occurs in duralumin, iron, and brass [42]. However, double-cup fracture was observed in pure metals such as Cu, Al, Ag, Au, and Ni [42] (Figure 1-22 (b)).

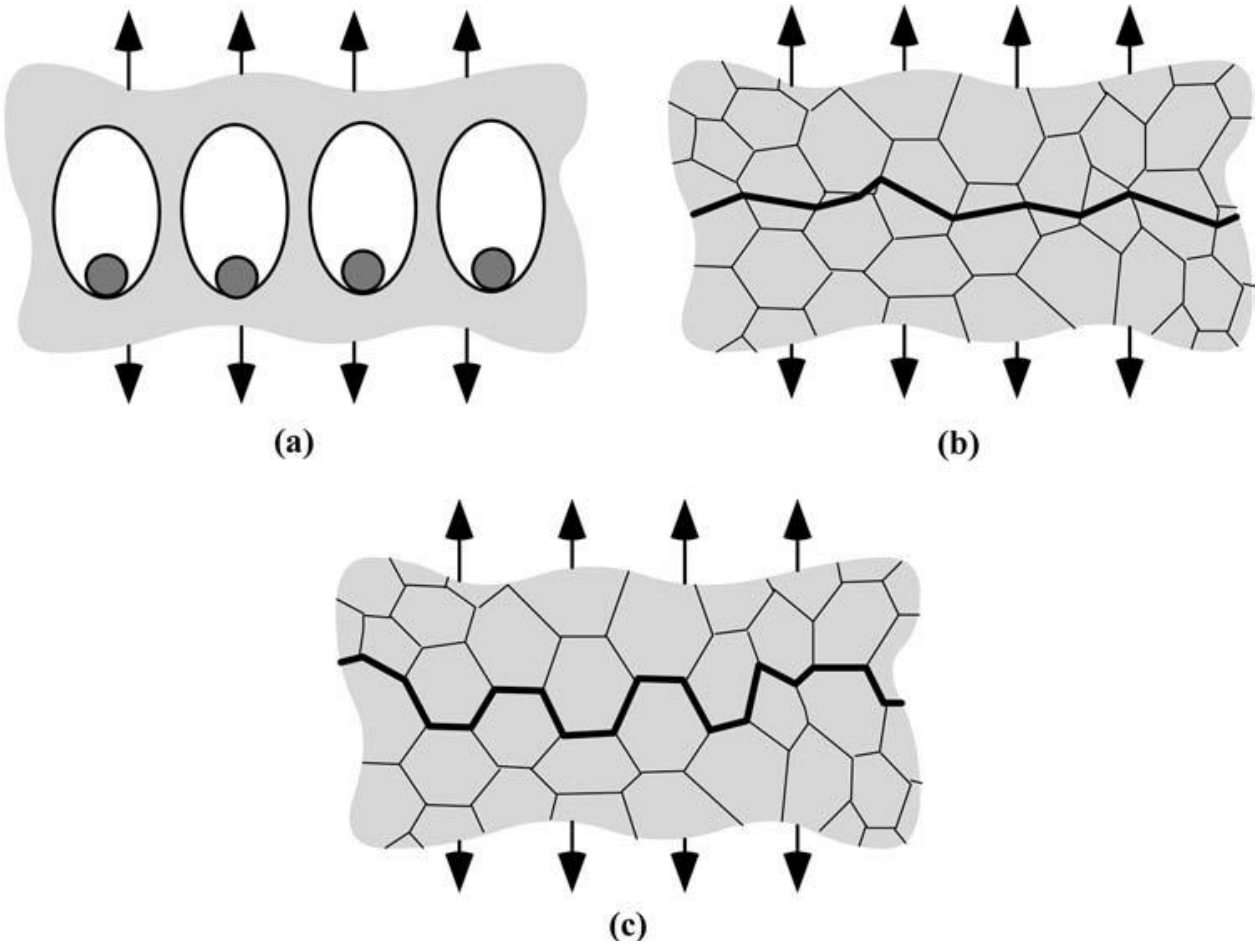

Figure 1-19: Schematic representations of fracture modes in metals: (a) ductile fracture (dimpled rupture), (b) cleavage, and (c) intergranular fractures (decohesive rupture) [6]

1.4.2 Cleavage fracture

Cleavage is a term used for brittle fracture occurring along crystallographic planes, perpendicular to the loading axis [44]. In this fracture mode, the atomic bonds break and crystallographic planes are separated during crack propagation. Very small energies are absorbed during cleavage fracture since rupture occurs only by breaking the atomic bonds along the lowest packing density crystallographic planes [6].

For BCC metals and alloys, brittle fracture occurs by cleavage. This kind of rupture is the most common fracture mechanism occurring at low temperatures since most of the slip systems are inactive. The cleavage fracture also occurs in HCP metals because of their limited slip systems.

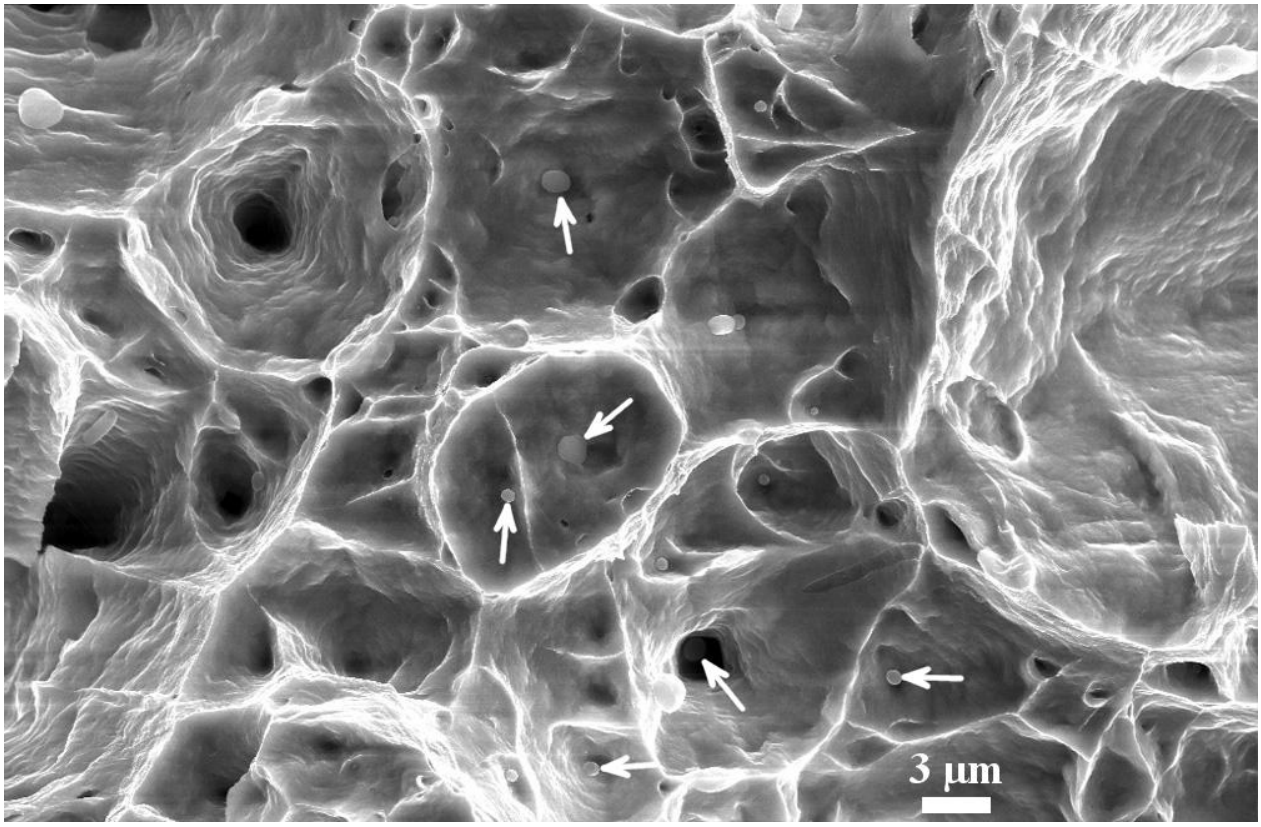

Figure 1-20: Dimpled rupture in austenitic stainless steel [37]. Some inclusions are shown by the arrows

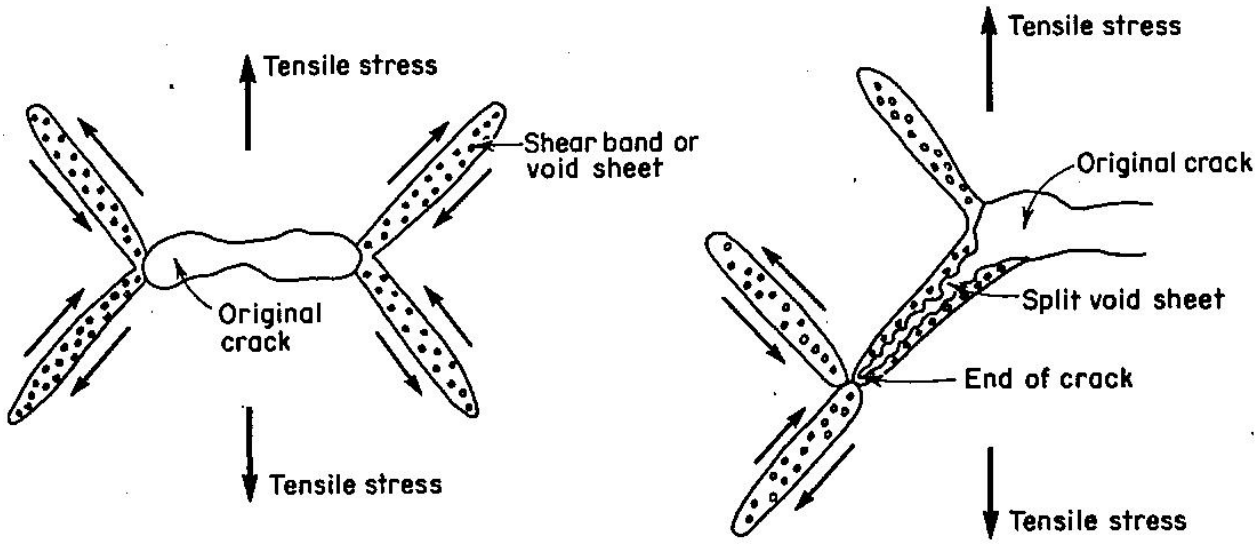

(a) (b)

Figure 1-21: (a) formation of void sheets, (b) crack propagation through the void sheets [43]

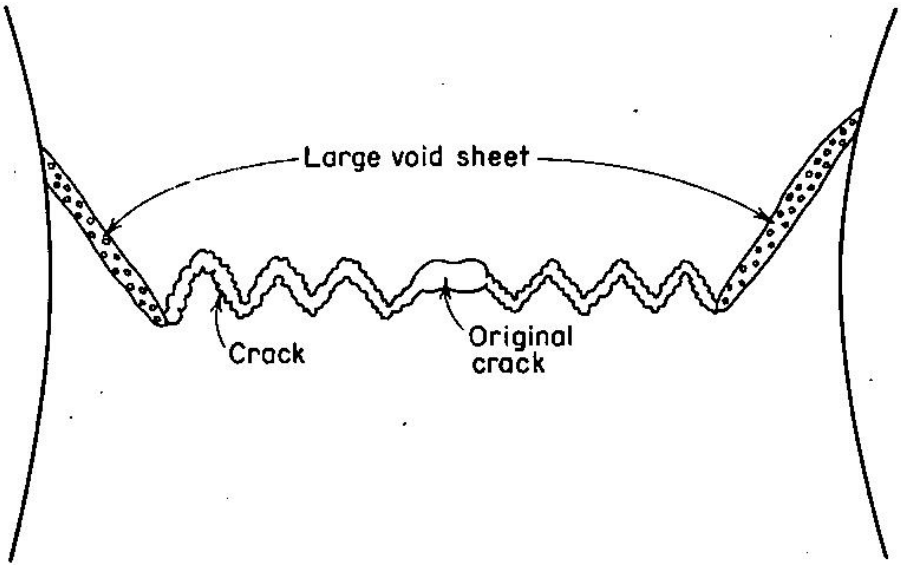

(a)

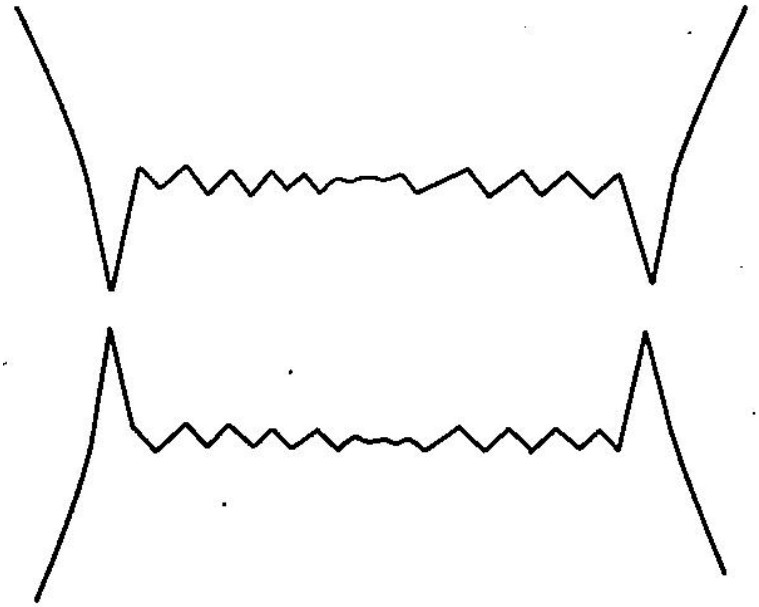

(b)

Figure 1-22: Schematic representations of (a) cup-cone, and (b) double-cup fractures [43]

However, cleavage does not usually occur in FCC metals since even at low temperatures various slip systems remains active [6].

The crack propagation occurs along (100) planes in BCC metals leading to a flat fracture appearance in a macroscopic scale [6, 44]. However, since each grain has different orientation in

polycrystalline materials, crack changes its direction at the grain boundaries to propagate along the most favorable crystallographic planes. A multi faceted cleavage fracture surface is shown in Figure 1-23. Each of these facets was formed from a single grain. One of the macroscopic characteristics of cleavage fracture is its shiny appearance due to the flat cleavage facets [44].

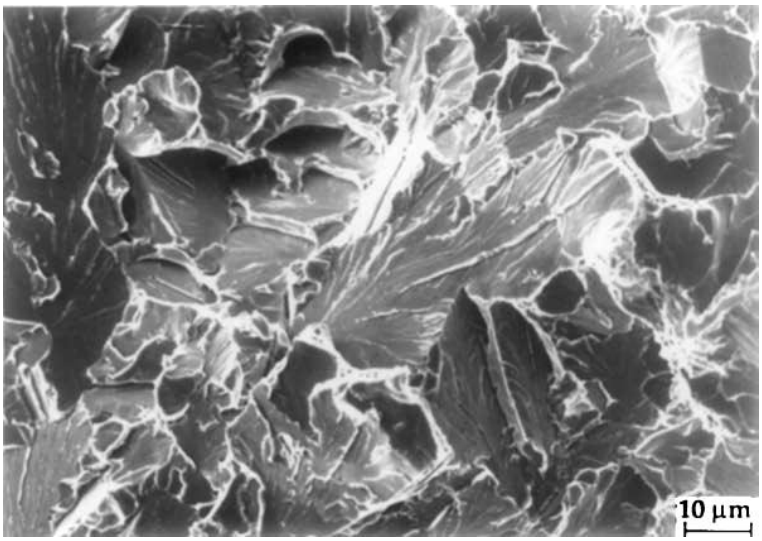

Figure 1-23: SEM micrograph of a multifaceted cleavage fracture surface [6]

In a microscopic scale, river patterns are other typical characteristics of cleavage fracture. Schematic representation of the river patterns formation, as well as an SEM micrograph of river patterns in a low carbon steel are shown Figures 1-24 (a) and (b), respectively. In a grain, crack propagates in different planes reaching a twist boundary[1], as shown in (a), since crack propagation occurs along the most favorable cleavage planes. This is the basis of river patterns formation.

1.4.3 Intergranular fracture

This kind of fracture called also as “decohesive rupture” is neither ductile nor cleavage occurring along grain boundaries. The fracture occurs due to the embrittlement of grain boundaries. In a microscopic scale, grains can be clearly observed since fracture occurred by decohesion of atoms

[1]- A twist boundary forms when crack intersects a grain boundary making some angles with its propagation plane [44].

along the grain boundaries, as shown in Figure 1-25 [6, 45]. For example, segregated sulfur leads to the grain boundary embrittlement in steels causing intergranular fracture [46].

1.5 Microstructure-mechanical properties relationships

1.5.1 Carbon content and grain size

The carbon is very important element in a martensitic microstructure. The morphology and strength of martensite as well as its strength is related to the carbon content of the alloy. As can be seen in Figure 1-26, in carbon steels, for carbon contents lower than 0.6%, "lath martensite" is formed. "Plate martensite" forms if carbon content exceeds 1.0%. The martensite that forms in steels containing 0.6%-1.0% carbon, is a mix of lath and plate one.

Since carbon content of most steels used in industry is less than 0.6%, lath martensite is of great importance and its microstructure should be studied in detail. As shown in Figure 1-27, lath martensite has three substructures: packet, block, and lath. In other words, martensitic transformation could be considered as a microstructural refining process. During this transformation, a prior austenite grain divides into packets. Each packet consists of several blocks, and each block divides into laths [49].

Morito et al. [50] showed that the lath martensite microstructure becomes finer by increasing the carbon content of the alloy (Figure 1-28). Lath martensite is a high strength microstructure. This is because several strengthening mechanisms accumulate in its strengthening [40]. Martensite is a supersaturated solid solution of carbon atoms, and the main strengthening mechanism involved in its high strength is "solid solution" mechanism [11, 40]. Furthermore, lath martensite is a fine microstructure consisting of packets, blocks, and very fine laths whose boundaries are important obstacles against dislocation movement. Therefore, "grain boundary strengthening" mechanism is also involved. Moreover, martensite has a high dislocation density of more than 10^{10} dislocations per cm^2 which results in high strengths.

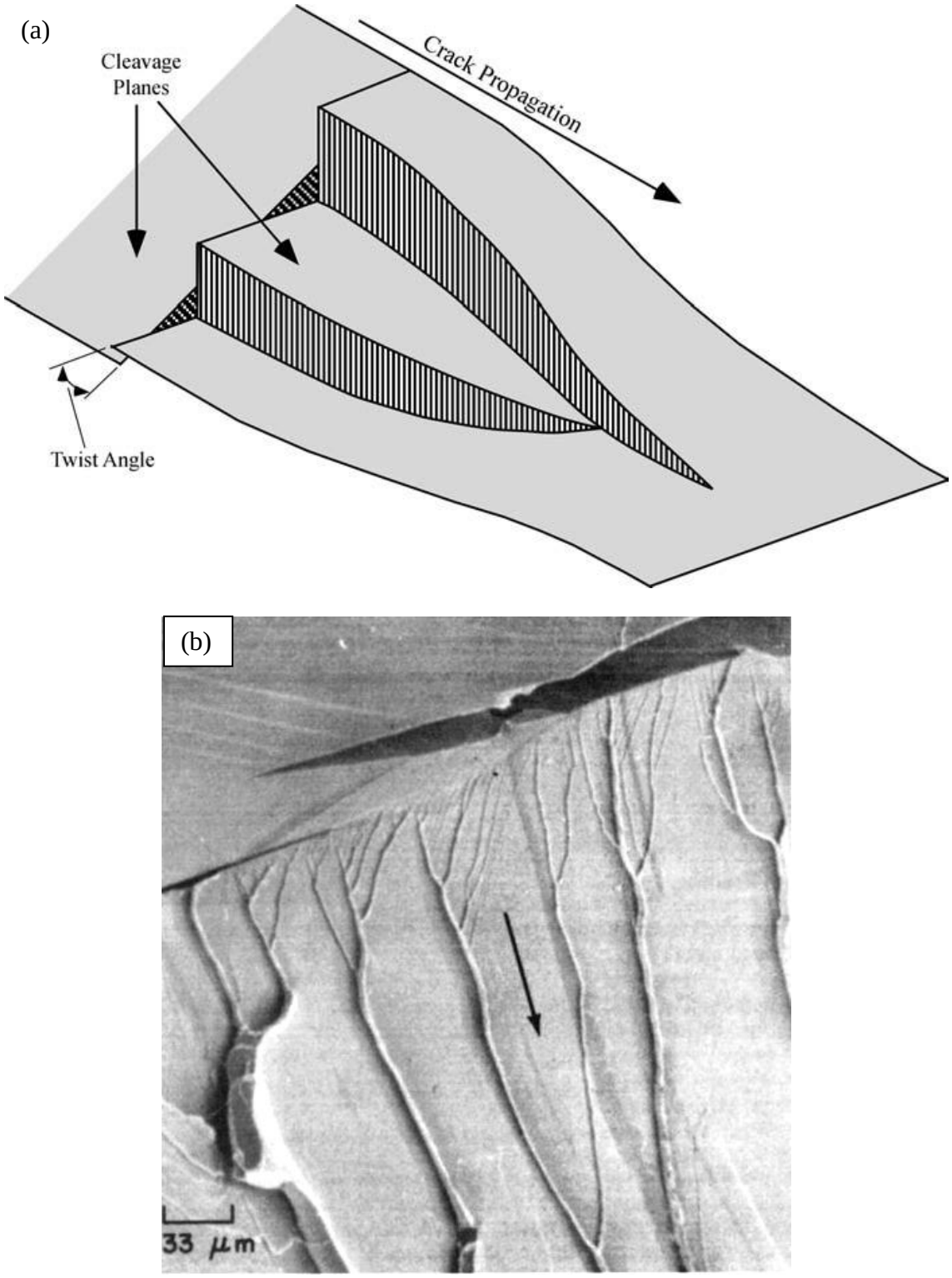

Figure 1-24: Formation of river patterns in a grain (a) schematic representation [6], and (b) in a low carbon steel [45]

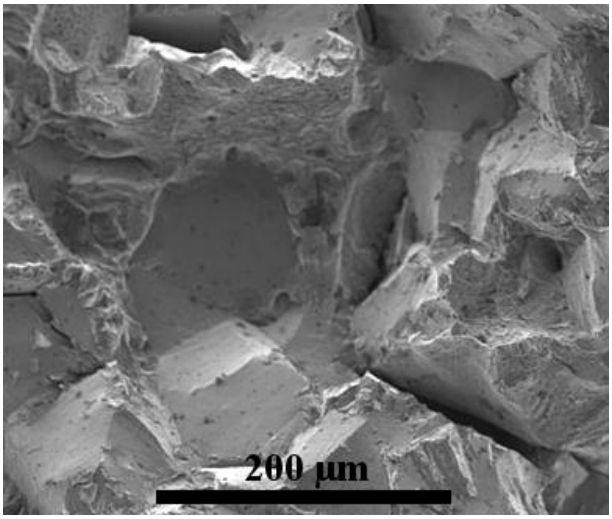

Figure 1-25: Intergranular fracture in a low alloy steel [47]

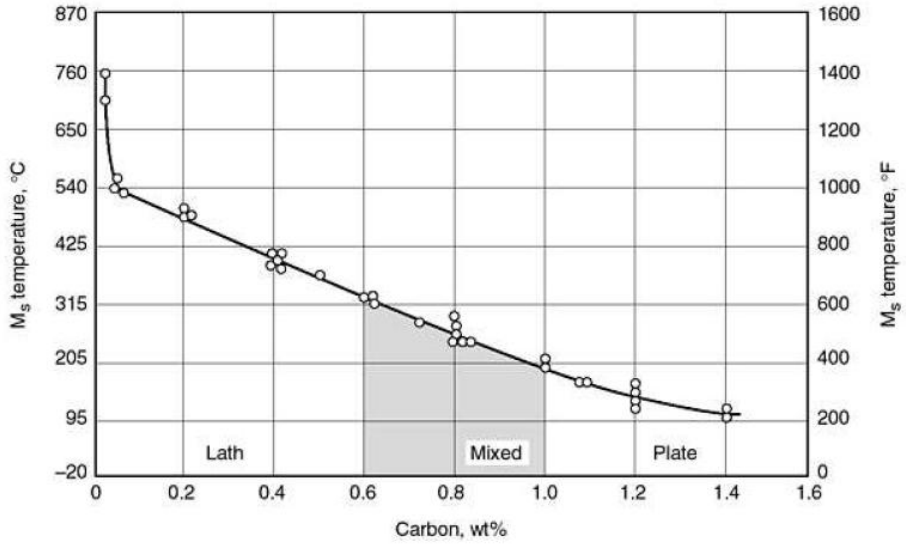

Figure 1-26: M_s and ferrous martensite morphology vs. carbon content [48]

The ductility is not highly affected by grain refinement as reported in [40]. The effect of prior austenite grain size on the fracture toughness K_{Ic} was studied by Stonesifer and Armstrong [51]. They showed that fracture toughness K_{Ic} is improved by decreasing the size of prior austenite grains. Wang et al. [52] showed that CVN fracture energy is not sensitive to the prior austenite grain size.

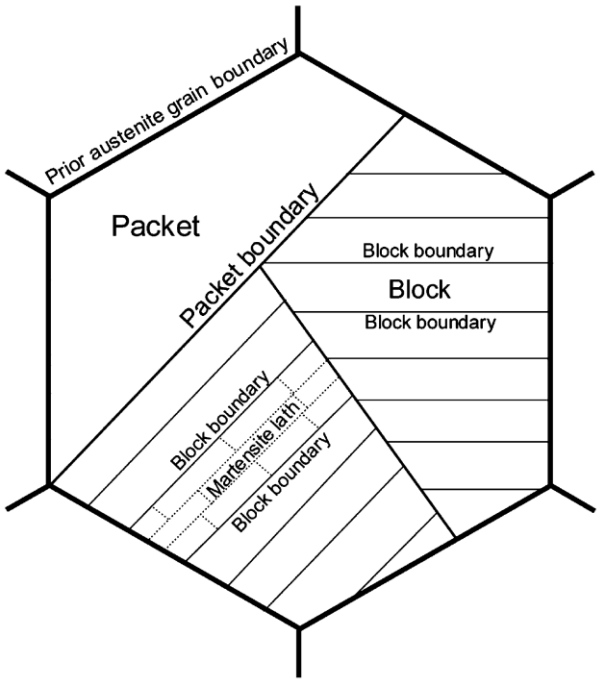

Figure 1-27: Lath martensite sub-structure [49]

1.5.2 Carbide formation

The formation of carbides results in the depletion of their surrounding matrix from chromium atoms (sensitization process). Carbides form at the prior austenite grain boundaries. This makes the passive film formed at the grain boundaries instable causing intergranular corrosion [53, 54].

On the other hand, carbides decrease the ductility and toughness [55]. This is because carbides are brittle and the large ones break during loading. Broken carbides are the crack initiation sites. The propagation of an existing crack can also be facilitated by these broken carbides [6, 56].

1.5.3 Delta ferrite

It is believed that the existence of supercooled delta ferrite at ambient temperature can have deleterious effects on the mechanical properties of the *chromium* martensitic stainless steels. Investigations conducted by Schäfer [55] showed that the presence of delta ferrite decreases the yield and tensile strengths of these alloys. This is because delta ferrite is softer than the martensitic matrix. The deleterious effect of the delta ferrite is more severe for yield strength than for tensile strength. Delta ferrite is also known to have deleterious effects on fracture toughness

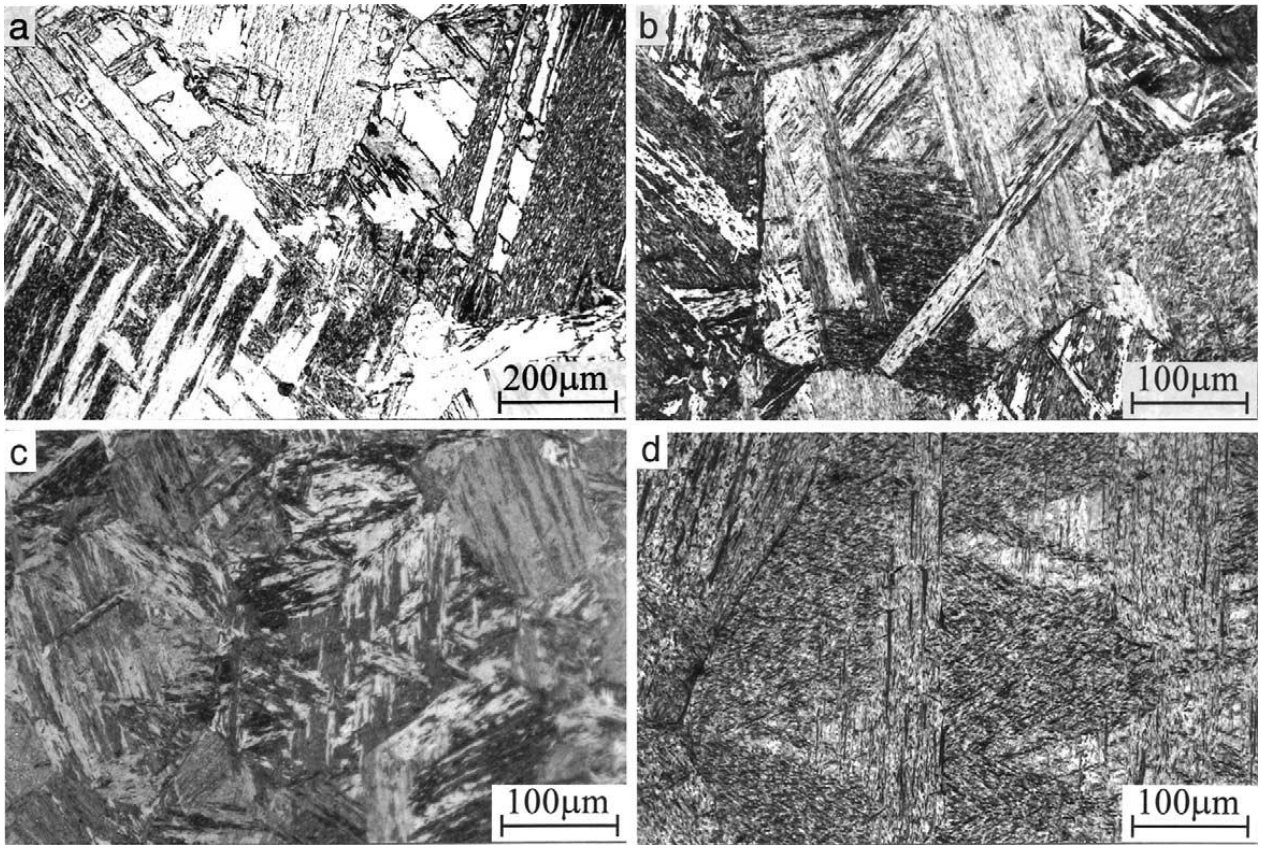

Figure 1-28: Lath martensite microstructure in carbon steels containing: (a) 0.0026% C, (b) 0.18% C, (c) 0.38% C, (d) 0.61% C [50]

and impact fracture energy [3, 57, 58]. Schäfer [55] observed that deleterious effect of delta ferrite on ductility and toughness is due to the presence of $M_{23}C_6$ carbides. Carbide precipitation at delta ferrite grain boundaries occurs during heat treatment, and act as crack initiation and propagation sites [56]. However, as mentioned in section 1.1.3, delta ferrite is removed from the microstructure of 13% Cr-4% Ni or its content is severely decreased by adding nickel.

1.5.4 TRIP effect of austenite

The austenite found in 13% Cr-4% Ni martensitic stainless steels is mechanically unstable and transforms into martensite by the so-called transformation-induced plasticity (TRIP) effect if deformations are applied [3, 19]. One of the important mechanisms leading to improve fracture toughness, CVN fracture energy, and ductility of 13% Cr-4% Ni martensitic stainless steels is the transformation of this metastable austenite [1-3]. Bilmes et al. [2, 3] studies showed that a

microstructure without delta ferrite, consisting of tempered martensite and uniformely dispersed reformed austenite results in a good combination of strength and ductility.

During crack propagation, the strain energy of the crack tip leads to the transformation of this *metastable* austenite into martensite and part of the energy which is needed to create new surfaces is absorbed by this transformation increasing the material toughness. Furthermore, compressive stresses produced by the volumetric expansion (about 4%) made by the formation of the martensite phase can close and deflect the crack tip [1]. All the mentioned mechanisms increase the material crack propagation resistance. TRIP effect of austenite during fracture toughness testing is shown in Figure 1-29. It has been shown by Thibault et al. [19] that TRIP effect of the austenite also takes place during fatigue crack propagation in cast and wrought 13% Cr-4% Ni martensitic stainless steels.

Effect of tempering temperature on austenite content, CVN fracture energy, yield, and tensile strengths are shown in Figure 1-30. In this figure, Au_1, Au_2, and Au_3 refer to retained austenite,

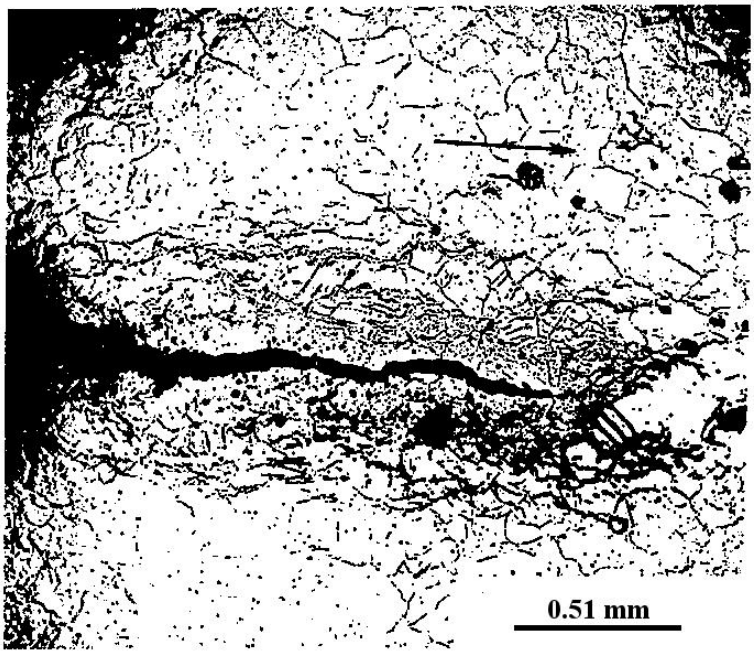

Figure 1-29: TRIP effect of austenite during fracture toughness testing [59]. Martensite formation is only observed around the crack

reformed austenite, and thermally unstable austenite retransformed into martensite during cooling, respectively. The maximum austenite content reaches up to 27% at 617 °C which consisted of 7% retained, and 20% reformed austenite. Up to the maximum amount of austenite,

CVN fracture energy increases, yield and tensile strengths decrease as martensite becomes more tempered and austenite content increases. However, CVN fracture energy decreased, but yield and tensile strengths increased by forming fresh martensite for tempering at temperatures higher than 617 °C.

1.5.5 Effect of (non-metallic) inclusions on ductile fracture

Density, size, spacing and nature of inclusions are of great importance. Higher inclusion density provides more nucleation sites for micro-void nucleation. Gurland and Plateau [9] assumed that the stress field around an spherical inclusion, and the resulted crack size have the same size as the inclusion size. Therefore, by considering the Griffith energy criterion i.e., the strain energy stored in the inclusion has to be equal to the surface energy needed for creating two new surfaces [60], they obtained the following equation:

$$\sigma_{void} = \frac{1}{\alpha}\left(\frac{E\gamma_s}{c_0}\right)^{0.5} \tag{1-10}$$

where σ_{void} is required stress for void nucleation, α is stress concentration factor around the inclusion, γ_s is surface energy needed to create new surfaces and c_0 is the inclusion size. This shows that as inclusion size increases, the stress needed for void nucleation decreases. Both matrix and inclusion were supposed to behave elastically. However, in ductile materials, the matrix deforms plastically before inclusion-matrix decohesion. The calculated σ_{void} was in a good agreement with experimental results of crack initiation around silicon particles in a copper-base composite.

Micro-voids initiate by matrix-inclusion decohesion and/or by inclusion rupture. In most cases, large inclusions fracture at low strains [6]. Cox and Low [61] reported that in AISI 4340 and 18 Nickel 200 Maraging steels, dimples nucleated at lower strains from larger inclusions. Therefore, void nucleation at lower stress, and accordingly lower strains, as well as inclusion rupture lead to a premature void formation on large inclusions at the early stages of straining. Firrao and Roberti showed that in mild steel, fracture toughness is affected by the spacing between the largest inclusions [62]. Other investigations confirmed that fracture toughness (K_{Ic}) improves when inclusion spacing increases [4, 7, 8]. This is because higher fracture energy is absorbed during the growth stage. However, note that the growth stage depends on the initiation stage, and to improve

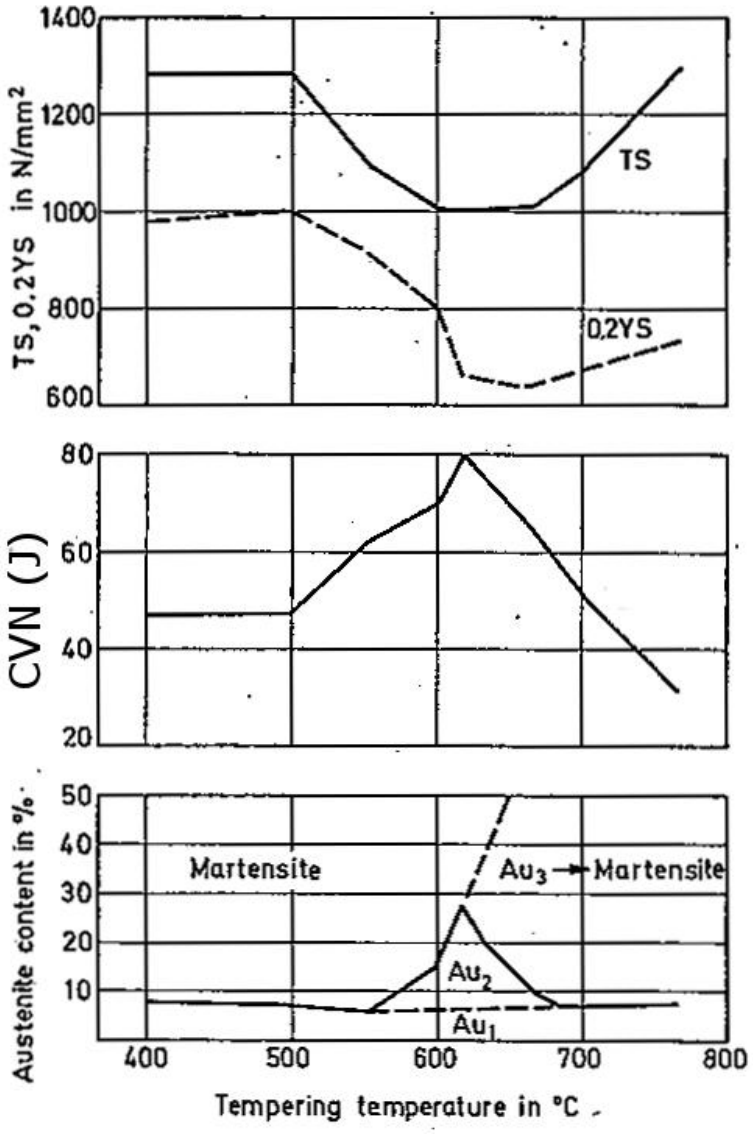

Figure 1-30: Effect of tempering temperature on austenite content, CVN fracture energy, yield, and tensile strengths [15]

toughness, it should decrease the initiation sites. That is to say, ductile rupture is controlled by the nucleation of micro-voids.

In 1969, a model was proposed for the growth of a spherical void in terms of the rate of stress triaxiality in a perfectly plastic matrix by Rice and Tracey [63]:

$$\frac{dR}{R} = \beta \exp\left(\frac{3\sigma_m}{2\sigma_{eq}}\right) d\varepsilon_R \tag{1-11}$$

where dR/R is the growth rate of an isolated spherical void, β is a constant equal to 0.283, σ_m is the hydrostatic stress, σ_{eq} is the Von-Mises equivalent stress, and ε_R is the plastic strain. Note that σ_m/σ_{eq} is defined as the stress triaxiality. As can be seen in this model, the increment in the plastic strain ($d\varepsilon_R$) decreases exponentially by increasing the stress triaxiality for a given growth rate of the radius of the void (dR/R).

In 1991, the constant, β, was modified by Huang [64] for different stress triaxiality rates:

$$\frac{dR}{R} = 0.427 \exp\left(\frac{3\sigma_m}{2\sigma_{eq}}\right) d\varepsilon_R \qquad \text{for} \quad \frac{\sigma_m}{\sigma_{eq}} \geq 1 \tag{1-12}$$

and

$$\frac{dR}{R} = 0.427 \left(\frac{\sigma_m}{\sigma_{eq}}\right)^{1/4} \exp\left(\frac{3\sigma_m}{2\sigma_{eq}}\right) d\varepsilon_R \qquad \text{for} \quad 1/3 \leq \frac{\sigma_m}{\sigma_{eq}} \leq 1 \tag{1-13}$$

The plastic strain needed for the growth of a spherical void (ε_R) to a certain radius can be obtained by integrating equations (1-11) and (1-12):

$$\varepsilon_R = 2.342 \ln\left(\frac{R}{R_0}\right) \exp\left(-\frac{3}{2} S_T\right) \qquad \text{for} \quad S_T \geq 1 \tag{1-14}$$

and

$$\varepsilon_R = 2.342\, S_T^{(-1/4)} \ln\left(\frac{R}{R_0}\right) \exp\left(-\frac{3}{2} S_T\right) \qquad \text{for} \quad 1/3 \leq S_T \leq 1 \tag{1-15}$$

Where R_0, and R are the initial and final radius of a spherical void, and S_T is the stress triaxiality.

Another parameter affecting the MVC mechanism is the nature of inclusions. Inclusions producing stronger bonding with the matrix and ones which are less disposed to rupture retard the nucleation of micro-voids [6].

1.6 K_{Ic}-CVN correlations

As mentioned in the introduction, there is a practical interest to predict fracture toughness K_{Ic} using CVN fracture energy values; K_{Ic} is a complex and time consuming test needing special equipments, whereas CVN test is much easier, quick, needing just a pendulum impact testing machine which is commonly used in the industry. However, major differences exist between

these tests. The K_{Ic} specimen is pre-cracked by fatigue cycling to obtain the sharpest possible notch, whereas the CVN specimen contains a 45° V-notch with a 0.25 mm root radius produced by machining. The second difference is in their strain rate. The strain rate in fracture toughness K_{Ic} test is about $\dot{\varepsilon} = 10^{-3}\, s^{-1}$, but that in CVN test is about $\dot{\varepsilon} = 10^{3}\, s^{-1}$ [37, 65]. The third difference is attributed to the nature of these tests; in K_{Ic} testing, the energy needed to initiate a crack is measured, whereas the total fracture energy (crack initiation + crack propagation) is measured in CVN testing [66].

Despite these differences, many efforts have been done to make K_{Ic}– CVN correlations from 1970 until now. Generally, there are two kinds of correlations:

1. K_{Ic} – CVN upper shelf correlations;
2. K_{Ic} – CVN transition region correlations.

Some methods have been developed to minimize the major differences existing between K_{Ic} and CVN tests by making more precise K_{Ic} predictions like using precracked Charpy specimen (having the sharpest possible notch), and by performing slow bend Charpy (to decrease the rate of straining). In fact, these methods are only useful for K_{Ic}– CVN correlations in the transition region because the effects of the major differences between K_{Ic} and CVN tests are less important in the upper shelf region as discussed below.

In sufficiently ductile materials, the specimen deforms plastically during a CVN test in the upper shelf region. Furthermore, this plastic deformation is very large leading to important blunting of a fatigue crack. Therefore, the lower stress intensity at the tip of this blunted crack results in a state of deformation similar to that of conventional machined notch [67]. As a result, the effect of notch acuity can be neglected for K_{Ic} – CVN upper shelf correlations.

Investigations made by Barsom and Rolfe [68] showed that a K_{Ic} transition-temperature curve similar to that of Charpy test does exist for a low alloy steel. A schematic representation of K_{Ic} and CVN transition curves is shown in Figure 1-31. As can be seen in this figure, higher strain rate in CVN test leads to shift the transition curve towards higher temperatures. There is a large temperature offset between K_{Ic} and CVN curves in the transition region, but the upper shelf values are approximately in a same temperature region. This shows that the difference between strain rate of K_{Ic} and CVN tests doesn't have a large effect on K_{Ic} – CVN upper shelf correlation.

In this research, where CVN absorbed energy is almost at its maximum value at room temperature, the goal is to predict upper shelf K_{Ic} values using upper shelf CVN fracture energies. The K_{Ic} prediction should not be affected markedly by the notch acuity and strain rate.

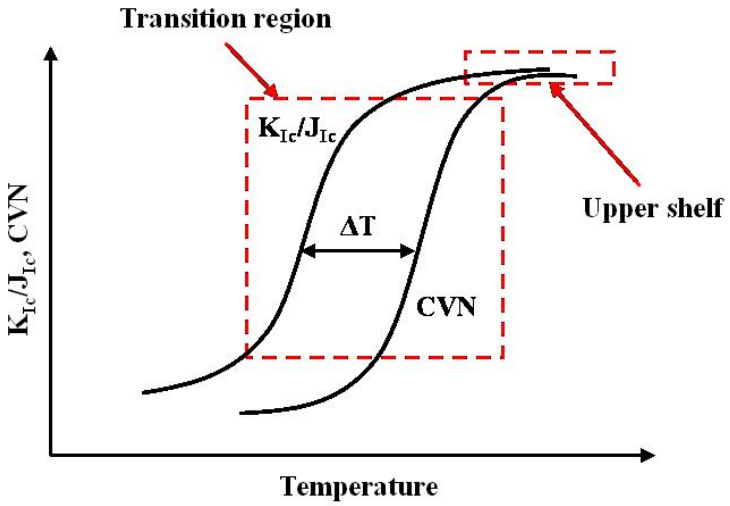

Figure 1-31: Schematic representation of temperature offset (ΔT) caused by difference in rate of straining between K_{Ic} and CVN tests

Since 1970, many efforts have been made to correlate CVN fracture energy to fracture toughness K_{Ic} in the upper shelf regime for various materials. Most of these correlations were empirically developed for specified ranges of yield strengths. The first correlation was made by Rolfe and Novak [69] in 1970 for low alloy steels with yield strengths in the range of 760-1700 MPa:

$$\left(\frac{K_{Ic}}{\sigma_y}\right)^2 = 0.64\left(\frac{CVN}{\sigma_y} - 0.01\right) \qquad (1\text{-}16)$$

where σ_y is the yield strength in MPa, CVN is the fracture energy in Joules, and K_{Ic} is the fracture toughness in MPa√m. Actually, Rolfe and Novak [69] showed that a simple empirical correlation does exist between K_{Ic} and CVN fracture energy if the values are normalised by the material yield strength. This correlation was established for steels having high strengths but low upper shelf CVN fracture energy values. As shown in Table 1-2, steels used for this correlation have yield strengths between 760 MPa and 1700 MPa, and CVN values between 31 J and 121 J. In 1973, correlation of Rolfe – Novak was used by Begly and Toolin [70] for a Ni-Cr-Mo-V alloy steel with bainitic microstructure having a yield strength of 727 MPa and an upper shelf CVN

absorbed energy of 81 J. Results showed a good agreement between predicted and measured K_{Ic} values. CVN value of steel used by Begly and Toolin [70] was in the range of the ones used by Rolfe and Novak [69], but the yield strength was 33 MPa lower. On the other hand, in 1977 investigations made by Iwadate et al. [71] confirmed that correlation of Rolfe-Novak can be used for a wider range of yield strengths and CVN absorbed energies. They used 4 alloy steels of 2 ¼ Cr-1Mo grade and a Ni-Mo-V rotor steel. The yield strength of the materials was between 390 MPa and 590 MPa, and their CVN values were between 105 J and 212 J.

After Rolfe and Novak, in 1971, Auld, Wald and Bertolo developed a correlation for ultra-high strength steels with yield strengths between 1610 MPa and 1980 MPa, and CVN fracture energies between 15 J and 29 J [72]. Similar to the correlation of Rofe-Novak, they normalised K_{Ic} values and CVN fracture energies by the yield strengths. In 1976, Thorby and Ferguson developed a correlation for low alloy steels having yield strength ranging from 400 MPa to 560 MPa [73]. They established an empirical correlation between K_{Ic} and CVN absorbed energy per unit area.

Schindler [74] in 2000, and Wallin et al. [75] in 2002 directly correlated the fracture toughness J_{Ic} value to the CVN fracture energy. An analytical correlation was made by Schindler to predict the fracture toughness J_{Ic} using uniform elongation (provided by tensile testing) and CVN fracture energy, whereas in the correlation of Wallin et al., CVN fracture energy, yield strength and the temperature at which the CVN test was performed were taken into account. 112 J-R curves have been analyzed by Wallin et al. to establish the correlation, but unfortunately they didn't mention which kind of material has been used.

In British Standard (BS 7910:2005) [76], an empirical K_{Ic}-CVN correlation for ferritic steels of maximum yield strength of 480 MPa is proposed. A very conservative K_{Ic} will be predicted by this correlation. A summary of the K_{Ic} – CVN upper shelf correlations is given in Table 1-2.

Table 1-2: A review of K_{Ic} – CVN upper shelf correlations (SI units)

Author	Year	Materials	σ_y (MPa)	CVN (J)	Correlation
Rolfe-Novak [69]	1970	Low alloy steels + Maraging steels	760-1700	31-121	$\left(\frac{K_{Ic}}{\sigma_y}\right)^2 = 0.64\left(\frac{CVN}{\sigma_y} - 0.01\right)$
Ault-Wald-Bertolo [72]	1971	Low alloy steels	1610-1980	15-29	$\left(\frac{K_{Ic}}{\sigma_y}\right)^2 = 0.18\frac{CVN}{\sigma_y} - 0.0011$
Thorby-Ferguson* [73]	1975	Low alloy steels	400-560	5-125	$K_{Ic} = 15\left(\frac{CVN}{A}\right)^{0.534}$
Schindler [74]	2000	Analytical	-	-	$K_{Ic} = \sqrt{\frac{3.92 e_u^{1/3} (CVN) E}{(1-\nu^2)}}$
Wallin et al. [66]	2002	112 materials	-	-	$K_{Ic}^2 = 0.53 E (CVN^{1.38}) 0.2^m$ $m = 0.133(CVN^{0.256}) - \frac{\sigma_y}{4664} + 0.03$
British Standard [76]	2005	Ferritic steels	< 480	-	$K_{Ic} = 0.54(CVN) + 55$

*- A is the area of the CVN specimen in cm^2.

1.7 Conclusions

A review on physical and mechanical metallurgy of martensite and 13% Cr-4% Ni martensitic stainless steels was made to have the necessary knowledge to undertake the research work of this thesis. These steels possess a complex microstructure and high mechanical properties. The microstructure consists of lath martensite, delta ferrite and in most of the time austenite. These steels are of high strength, high fracture toughness K_{Ic}, and high CVN fracture energy.

The most important microstructural parameters affecting the mechanical properties of 13% Cr-4% Ni martensitic stainless steels are carbon and austenite contents. Carbon is the most important alloying element affecting the strength of martensite. TRIP effect of austenite improves the ductility, fracture toughness, and CVN fracture energy. Additionally, non-metallic inclusions are the most important microstructural features affecting ductile rupture in steels. The literature review shed light on the features which should be considered studying microstructure and ductile rupture of 13% Cr-4% Ni martensitic stainless steels.

Fracture toughness J_{Ic} is an intrinsic property of the material provided by Elastic-Plastic Fracture Mechanics, and it is used for crack propagation predictions. Special equipments are needed to perform a J_{Ic} test, which is a complex, and time consuming test. In this study, fracture toughness J_{Ic} of the cast version, and for the first time in the literature, those of the wrought version, and the weld metal (in the as-welded and heat-treated conditions) of 13% Cr-4% Ni martensitic stainless steels is provided. The J-R curves are plotted and stable crack propagation properties of the base and weld metals of 13% Cr-4% Ni martensitic stainless steels are discussed. Finally, existing upper shelf K_{Ic}-CVN correlations were reviewed.

Microstructure, mechanical properties (tensile, fracture toughness J_{Ic}, and CVN fracture energy), and upper shelf K_{Ic}-CVN correlation of 13% Cr-4% Ni martensitic stainless steels base and weld metals are studied in the next chapters considering features/results discussed in the literature review.

CHAPTER 2 MATERIALS AND EXPERIMENTAL PROCEDURES

2.1 Materials

2.1.1 Chemical compositions

A cast (CA6NM) and a wrought (S41500) 13% Cr-4% Ni martensitic stainless steels base metals as well as their matching filler metal (E410NiMo) were used in this study. CA6NM, S41500 and 410NiMo nomenclatures were defined by ACI (Alloy Casting Institute), UNS (Unified Numbering System), and AWS (American Welding Society), respectively. Similar heat treatment procedures were used for the base metals: austenitization and tempering processes were performed at 1050 °C and 1000 °C, and 610 °C and 600 °C for CA6NM steel and 415 steel, respectively. The chemical compositions of the studied materials are shown in Table 2-1. Measurements were performed using inductively coupled plasma-emission atomic spectrometry (C and S were measured by combustion). The composition requirements according to ASTM A743 [29], ASTM A240 [77] and AWS A5.22/A5.22M [78] are also added. All the values are verified by these standard requirements.

Table 2-1: Chemical compositions of the studied materials (wt%)

Designation	C	Mn	P	S	Si	Cr	Ni	Mo
CA6NM steel	0.016	0.50	0.019	0.007	0.26	12.79	3.49	0.55
ASTM A743	0.06 (max)	1.00 (max)	0.04 (max)	0.03 (max)	1.00 (max)	11.5-14.0	3.5-4.5	0.40-1.0
415 steel	0.028	0.73	0.022	0.002	0.34	13.021	3.91	0.56
ASTM A240	0.050 (max)	0.50-1	0.030 (max)	0.030 (max)	0.60 (max)	11.5-14	3.5-5.5	0.5-1
410NiMo steel	0.027	0.04	0.01	0.0093	0.48	12.1	4.67	0.61
AWS A5.22/A5.22M	0.06 (max)	1.0 (max)	0.04 (max)	0.03 (max)	1.0 (max)	11.0-12.5	4.0-5.0	0.4-0.7

2.1.2 Fabrication of the E410NiMo weld metal block

A semi-automatic Flux-Cored Arc Welding (FCAW) process was used to deposit a weld metal block of 450 × 250 × 60 mm. Welding process was performed in flat position. A 50 mm thick

CA6NM steel block was used as the substrate material. Welding parameters are given in Table 2-2.

Table 2-2: FCAW parameters used in this study

Pre-heat (°C)	Inter-pass (°C)	Current (A)	Voltage (V)	Torch speed (mm/s)	Deposition rate (g/s)	Heat input (J/mm)	Protection gas
180	200	218	22.5	4.5	1.125 g/s	1090	25% CO_2 + 75% Ar

Welding assembly, CA6NM substrate steel and the first weld beads are shown in Figure 2-1. After each welding pass, the slag was removed and the next bead was deposited in a time interval of about 10 minutes to reach an inter-pass temperature of 200 °C.

In order to use the most homogenous part of the deposited block, heat-treated by adjacent beads, thicknesses of about 20 mm and 10 mm were removed from all four sides, and from the surface, respectively. After cutting a section for preparing J_{Ic} samples in the HAZ, the weld metal was separated from the substrate. This separation was performed at a distance of about 4 mm from the fusion line to remove the diluted part of the block at the interface of the weld metal and CA6NM substrate steel. The cutting plan of the weld metal block is given in Appendix A. The welded block was tested in both as-welded and heat-treated conditions. Heat treatment process was performed at 600 °C for 2 hrs. A holding time of 10 min/inch was added to consider the thickness effect. The holding time was obtained by welding the thermocouples at different locations of the cut sections.

2.2 Mechanical testing

2.2.1 Tensile and CVN tests

Tensile tests were carried out according to ASTM E8/E8M [79] using cylindrical specimens of 5 mm diameter. In order to determine the possible anisotropy of 415 steel due to the rolling process, the tests were performed in the rolling and transverse directions (RD, TD). Three tests were performed for each material/orientation.

Notched bar specimens were used for the CVN tests and the tests carried out in accordance with ASTM E23 [80]. In the case of 415 steel, the tests were performed using specimens with the L-T

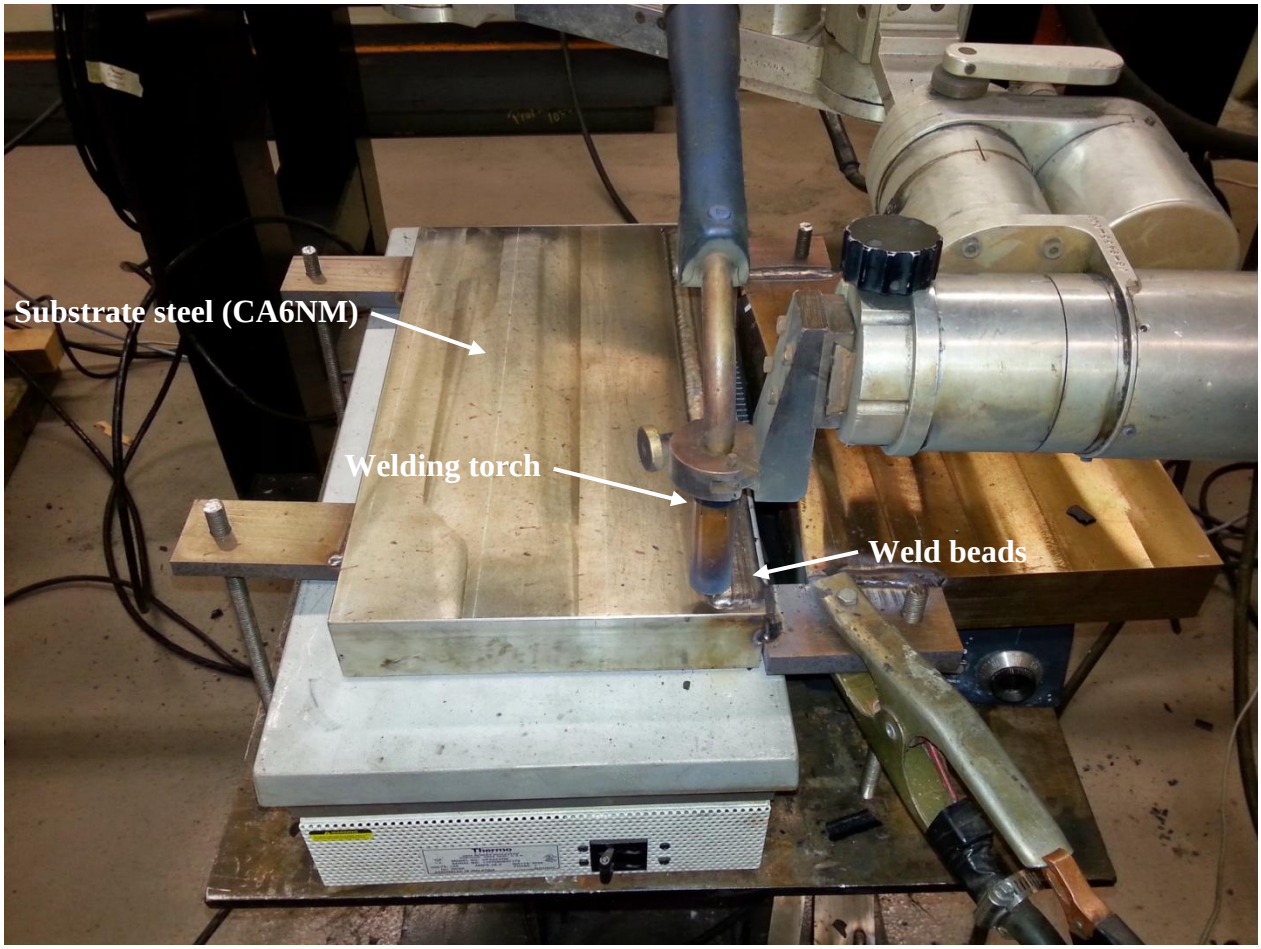

Figure 2-1: Welding assembly of the semi-automatic FCAW process

orientation. To draw complete Charpy ductile-brittle transition curves, CVN tests were carried out at 8 temperatures from 80 °C to -190 °C. Three tests were performed per material/temperature i.e., 24 tests were carried out for each material.

2.2.2 Preliminary J_{Ic} testing

The single specimen test method using CT specimens was selected to perform the J_{Ic} fracture toughness tests of this study according to the guidelines described in ASTM 1820 (section 1.3.3).

Preliminary J_{Ic} tests have been made by Chen et al. [81, 82] on a 13% Cr-4% Ni martensitic stainless steel similar to the cast base metal to be studied (CA6NM steel) in order to determine the best test conditions including the specimen geometry. They have compared the behavior of 50.8 mm wide specimens: smooth and 12.7 mm thick, side-grooved and 12.7 mm thick, and side-grooved and 25.4 mm thick.

They showed that only the 25.4 mm thick side-grooved specimens result in a valid fracture toughness J_{Ic} according to ASTM E-1820 requirements [41]. Fracture surface of one of these specimens is shown in Figure 2-2. The stable crack extension is marked by heat tinting at 450 °C for 2 hrs (the brown band). As can be seen in this figure, both fatigue and J_{Ic} stable crack fronts were straight. All the standard crack straightness and specimen size requirements were satisfied, and fracture toughness J_{Ic} of 266 kJ/m^2 (K_{Ic} equivalent of 242 MPa$\sqrt{m}$) was measured.

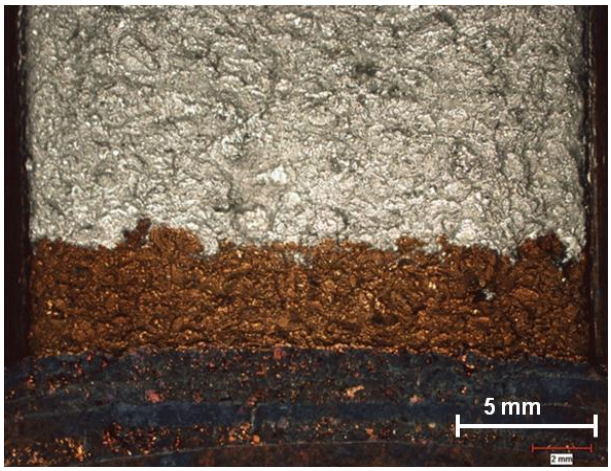

Figure 2-2: Fracture surface of a 25.4 mm thick side-grooved specimen [81]

However, the standard requirements were not satisfied using 12.7 mm thick specimens for both smooth and side-grooved specimens. As shown in Figure 2-3 (a), a flat crack extension only occurred at the center of the smooth specimen. This is because stress triaxiality took place at the center, while most of the specimen volume is in plane stress condition leading to the formation of lateral expansions. As shown in (b), the J_{Ic} stable crack growth was modified by machining the side-grooves, but an important curvature is observed and the crack front straightness conditions were still not satisfied.

Moreover, Chen et al. [81] showed that both 12.7 mm and 25.4 mm thick side-grooved specimens have similar J-R curves at the early stages of the test (Figure 2-4). This resulted in a J_Q/K_Q value very close to that obtained by testing 25.4 mm thick specimens (256 kJ.m^{-2}/237 MPa$\sqrt{m}$ vs. 266 kJ.m^{-2}/242 MPa$\sqrt{m}$).

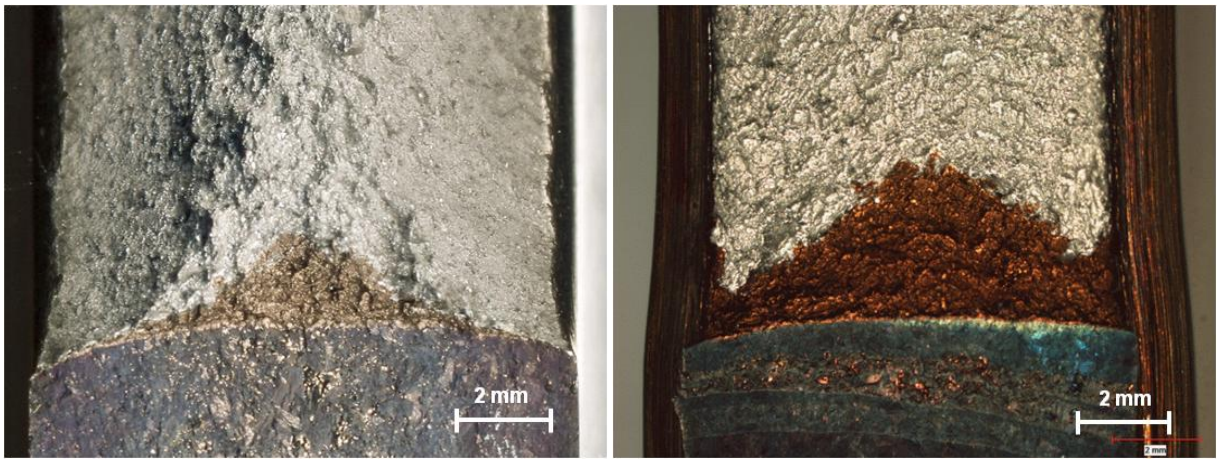

(a) (b)

Figure 2-3: Fracture surfaces of 12.7 mm thick specimens: (a) smooth specimen, and (b) side-grooved specimen [81]

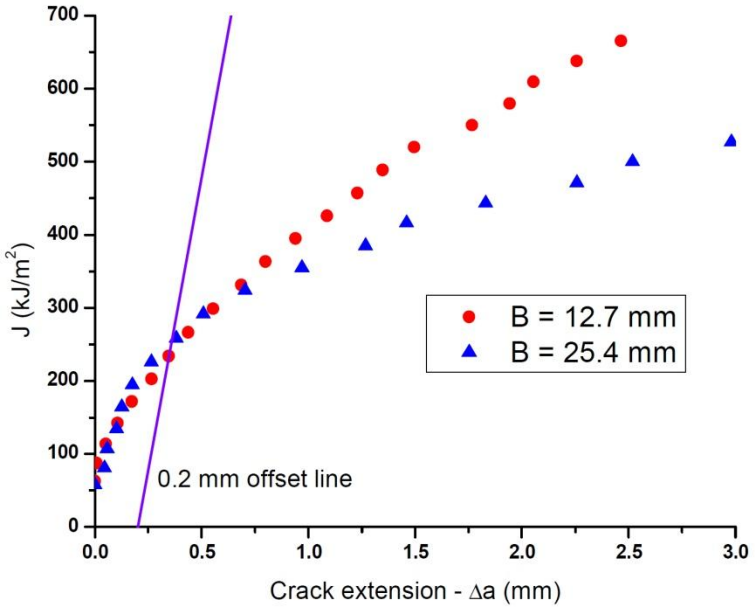

Figure 2-4: J-Δa plot obtained from 12.7 mm and 25.4 mm side-grooved specimens [81]

In addition, in order to decrease the test preparation time, Chen et al [81] showed that side-grooves can be machined before fatigue pre-cracking. The fatigue crack length can be monitored by elastic compliance using a clip-on gages instead of using optical microscopes. Using this procedure, a straighter fatigue crack front was obtained for the specimen side-grooved before pre-cracking (Figure 2-5 (b)), and there is no step between the fatigue precracking and ductile tearing planes. Moreover, no significant difference was measured between the J_{Ic} values.

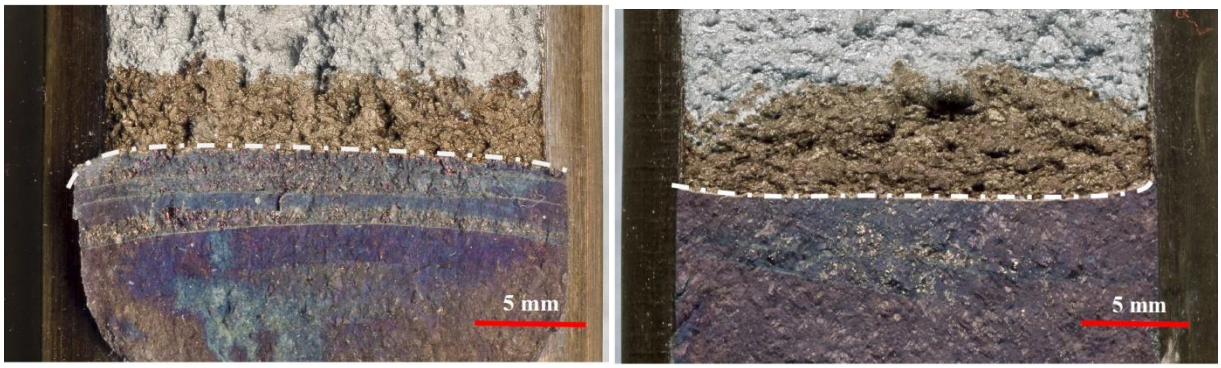

Figure 2-5: Fracture surfaces of specimens pre-cracked (a) before, and (b) after machining the side-grooves [81]

Figure 2-6 shows a technical drawing of the 25.4 mm thick side-grooved J_{Ic} specimen that has been used in this study. The plane strain conditions and a high stress triaxiality factor are maintained over the entire specimen thickness [83].

2.2.3 Detailed J_{Ic} test parameters

Fast track da/dN fatigue crack propagation and fast track J_{Ic} fracture toughness programs were used to perform fatigue pre-cracking and J_{Ic} test, respectively. Fatigue pre-cracking was performed after machining of the side-grooves to an initial crack length/width (a_0/W) ratio of 0.55. Constant ΔK values of 14 and 12 MPa$\sqrt{m}$ were used for the base metals and the weld metal, respectively, using a stress ratio of 0.1 and a loading frequency of 20 Hz.

Clip-on gages were used to record the total displacement. Elastic unloadings of 10% of the actual maximum load were used to predict the crack size by compliance and obtain the resistance curve. Since CA6NM steel has a high fracture toughness, the unload sequences were started at a large enough displacement of 0.5 mm. This parameter is recalled as “load point displacement (LPD) start point”. Then, to have enough load/unload sequences for evaluating the corresponding resistance curve a displacement increment of 0.075 mm was chosen, “LPD increment”. These parameters are very important and must be carefully selected especially for low fracture toughness materials, like 410NiMo, since evaluating an appropriate resistance curve is not possible for high values of LPD start point and LPD increment values. The former will result in a sudden propagation, and the latter will result in insufficient data points. Therefore, an LPD start point of 0.2 mm was used, and Load/unload sequences were continued with an LPD increment of

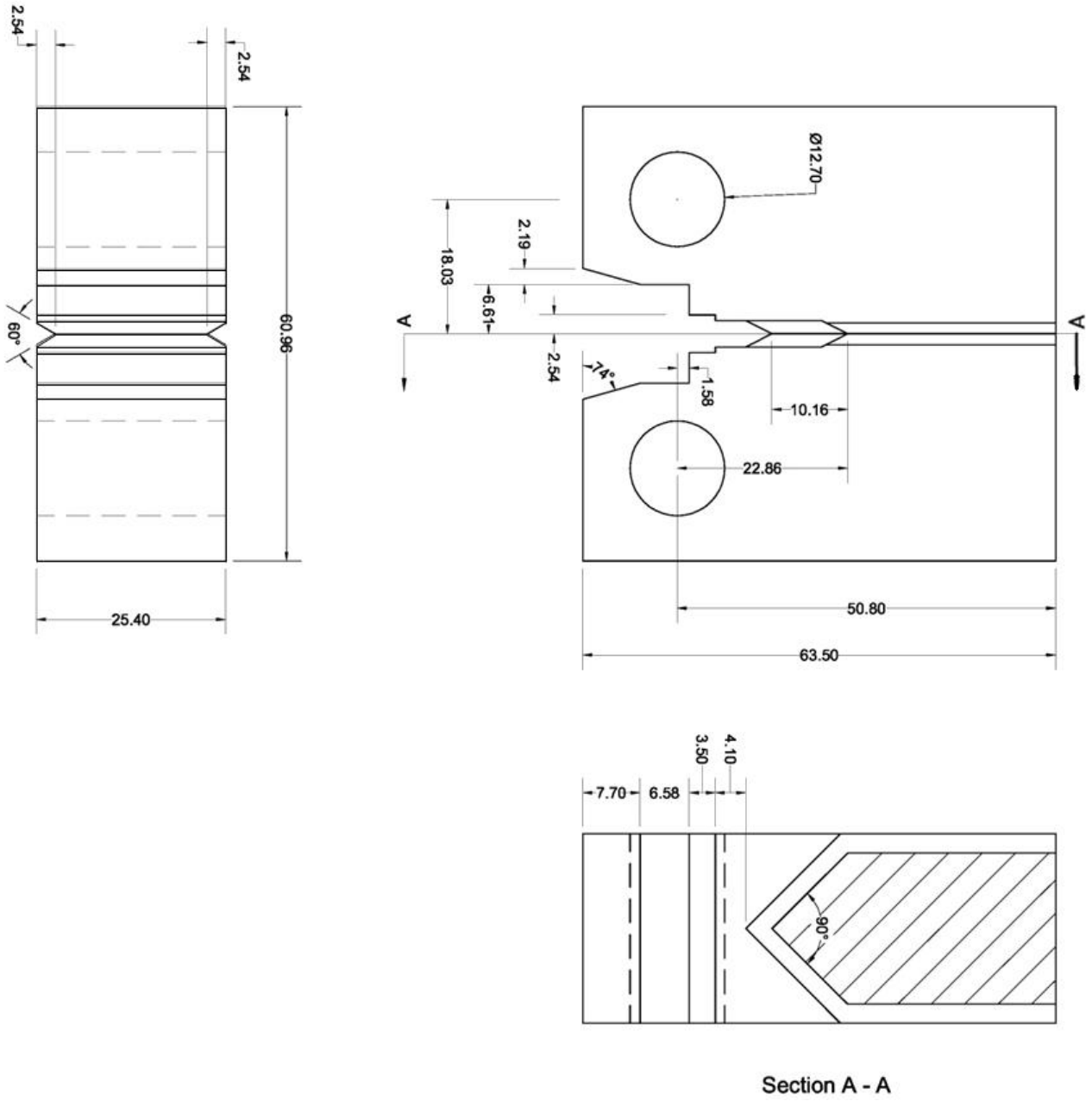

Figure 2-6: Technical drawing of the J_{Ic} specimen used in this study

0.03 mm. Finally, about 25 and 10 loading/unloading were performed to obtain the J resistance curves of the base metals and those of the weld metals, respectively.

In order to mark the J_{Ic} crack extension front, both heat tinting and fatigue cycling processes were used. For the heat tinting process, specimens were treated at 450 °C for 2 hrs. For fatigue cycling processes of the base metals, a constant ΔK value of 35 MPa$\sqrt{m}$ with a stress ratio of 0.5, and for

those of the weld metals, a constant ΔK value of 33 MPa√m with a stress ratio of 0.3 were used. These high values of stress intensity factors and stress ratios were needed to propagate the crack into the plastic zones produced in front of J_{Ic} crack extensions. A loading frequency of 20 Hz was used for fatigue cracking.

Crack front straightness was verified for both fatigue pre-cracking and J_{Ic} crack extension fronts measuring the crack lengths at 9 equally spaced points in accordance with ASTM E1820.

Three specimens per material/condition were tested. In the case of the wrought steel, specimens were machined with an L-T orientation and one more specimen was machined with a T-L orientation to examine the probable anisotropy between these orientations.

2.2.4 Fracture toughness J_{Ic} tests in the HAZ

The tests were performed in both as-welded and heat-treated conditions. A similar heat-treatment to the one used for the weld metal was performed. Compact tension (CT) specimens of the same dimensions of those used for the J_{Ic} testing of the base metals and the weld metal were also used. Three tests were performed for each condition. For the first test carried out in the as-welded condition, a smooth specimen was used, and the crack starter notch was put along the fusion line. A schematic representation of the J_{Ic} specimen used for this test is shown in Figure 2-7. However, since crack deviation occurred during fatigue pre-cracking and J_{Ic}-testing, side-grooved J_{Ic} specimens were used for the five other specimens (two specimens for the as-welded, and three other ones for the heat-treated conditions). The crack starter notch was put one millimeter far from the fusion line to observe material behavior during J_{Ic} crack propagation in the HAZ close to the fusion line.

The same J_{Ic}-test procedures/parameters as those of the weld metal J_{Ic} tests were used. Samples surfaces were polished and etched before and after the tests to put the crack starter notch at the desired location, and to examine the crack propagation path, respectively. Etching was performed using a Kalling's 2 solution (5 g $CuCl_2$, 100 mL HCl and 100 mL ethanol).

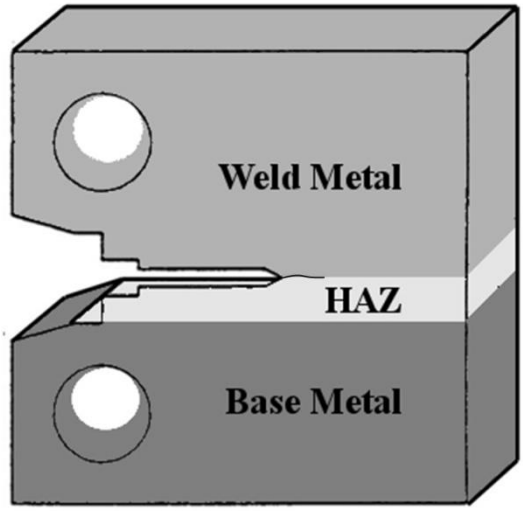

Figure 2-7: Schematic representation of the J_{Ic} specimen, crack starter notch along the fusion line

2.2.5 Summary of the performed mechanical tests

A summary of the mechanical tests performed in this study is provided in Table 2-3.

Table 2-3: A summary of the performed mechanical tests

Material	Metallurgical condition	Test		
		Tensile	CVN	Fracture toughness J_{Ic}
CA6NM	Tempered	3	24	3
415	Tempered	6 (3T + 3L)	24 (L-T)	3 (L-T) + 1 (T-L)
410NiMo	As-welded	3	24	3
	Heat-treated	3	24	3

2.3 Metallurgical investigations

2.3.1 Metallography

In order to observe the microstructures by optical microscopy, samples were ground using 240, 400, 600 and 800 grit sand papers, respectively. Ground surfaces were polished by 6, 3 and 1 diamond suspensions, respectively. Inclusion characteristics (surface density, volume fraction, size, and spacing of inclusions) were analyzed on the polished sections by optical microscopy. A low-level 50X magnification was used for the base metals since large inclusions existed in their microstructures affecting the inclusion volume fraction and the mechanical properties. Inversely, because of very small size of inclusions, a relatively high magnification of 500X was used in the

case of the weld metal. Five optical micrographs were chosen all over the polished surface of each material, and a total surface of 14 mm^2 and 0.15 mm^2 was examined for each of the base metals, and the weld metal, respectively. An automatic image analyzing software was used and at least 150 and about 2000 inclusions were examined for each of the base metals, and the weld metal, respectively. According to [4], $\lambda = 0.89 R_0 f^{-1/3}$ relationship was used to calculate inclusion average spacing, λ, where $R_0 = (\pi/4)H(d)$, *H(d)* is the harmonic mean value of inclusion diameters and *f* is the volume fraction of inclusions. Examples of the analyzed images are shown in Appendix B.

A modified Fry's etching solution (150 mL distilled water, 1 g $CuCl_2$, 50 mL HCl, and 50 mL HNO_3) was used to reveal the microstructures, and measure prior austenite grain sizes (in the case of the base metals) [19]. CA6NM and 415 steels samples were slightly etched to reveal the prior austenite grain boundaries. The grain sizes were measured in T-S, S-L, and L-T planes in the case of 415 steel since there can be some anisotropy induced by rolling process. Equivalent circle diameters were calculated from measured grain areas and an arithmetic mean of 100 grain diameters was defined as the prior austenite grain size for each material/orientation. To this purpose, 15 optical micrographs at 100X and 45 ones at 200X were examined for CA6NM steel and 415 steel, respectively. Examples of the measured prior austenite grains are shown in Appendix C.

2.3.2 Fractography and X-ray diffraction analysis

A scanning electron microscope (SEM) equipped with an energy dispersive X-ray (EDX) spectrometer was used to investigate fracture surfaces and chemical nature of inclusions. More than 270, 155, and 32 SEM micrographs at different magnifications, and 147, 82, and 16 EDX spectrums were examined for the base metals, the weld metals, and ruptures occurred in the HAZ, respectively.

The inclusion size was also measured on the fracture surfaces of tensile, fracture toughness J_{Ic}, and CVN specimens. Since automatic measurements were not possible in these cases; magnifications of more than 500X were used to increase the precision of these manual measurements. More than 100 inclusion sizes were measured for each alloy fracture surfaces.

Only intact inclusions were examined (fractured inclusions and those overlapping dimple walls were ignored).

In order to examine the contribution of the TRIP effect on the mechanical properties, austenite contents were measured on metallographic sections of the tested materials by means of quantitative X-ray diffraction (XRD). Additionally, in order to determine the region where TRIP occurs in J_{Ic}-testing of the base metals, austenite contents were also measured on cut planes perpendicular to the J_{Ic}-crack. To this purpose, two 20×10×2 mm samples were cut (one from the cast steel and one from the wrought steel) as represented in Figure 2-8. A surface of 7 mm^2 was large enough to properly diffract each austenite measurement region shown in (b).

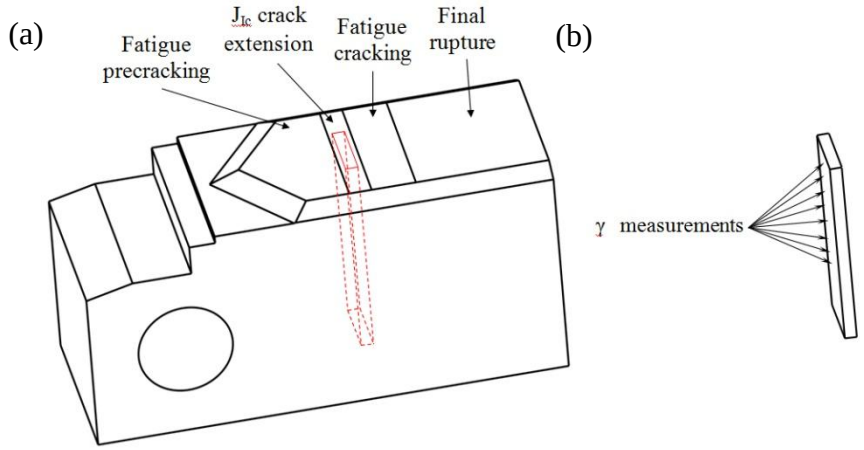

Figure 2-8: (a) position of the cut sample (dotted rectangular prism) in a J_{Ic} fractured specimen and (b) austenite (γ) measurement regions on the cut sample, as shown by the arrows

Diffraction peak intensities were evaluated using the Rietveld method [84]. A diffractometer equipped with a copper tube and a nickel filter was used. Diffraction patterns were obtained in the range $40° < 2\theta < 140°$ with a step size of 0.05°. Other experimental details regarding the quantitative austenite measurement procedures are reported in [19]. All of the samples used for austenite measurements were cut by an automatic cut-off machine. 0.5 mm thick saw blades with a cut speed of 0.05 mm/s were used to prevent transformation of austenite during the cutting process. Cut samples were ground by 1200 grit sand papers and etched in a 30% HCl + 30% HNO_3 + 40% H_2O solution for 10 minutes. These samples were etched again in HCl for 30 seconds. The surfaces of metallographic sections were 63 mm^2 and 84 mm^2 for CA6NM steel and

415 steel, respectively. Three samples were prepared from each material to measure the initial austenite content.

CHAPTER 3 RESULTS AND DISCUSSION: BASE METALS

3.1 Microstructure

The typical microstructure of the lath martensite can be observed in Figure 3-1 for both steels. Packets and blocks of martensite laths can be seen in both microstructures. As shown in this figure, CA6NM steel has a coarse microstructure as compared to 415 steel. This is confirmed by the prior austenite grain size measurements provided in Table 3-1. The prior austenite grain size of CA6NM steel is on average 85% larger than that of 415 steel. The prior austenite grain size of 415 steel is approximately equal in the three T-S, S-L and L-T cutting planes. It seems not be affected by the rolling process and the grains can be considered as equiaxed.

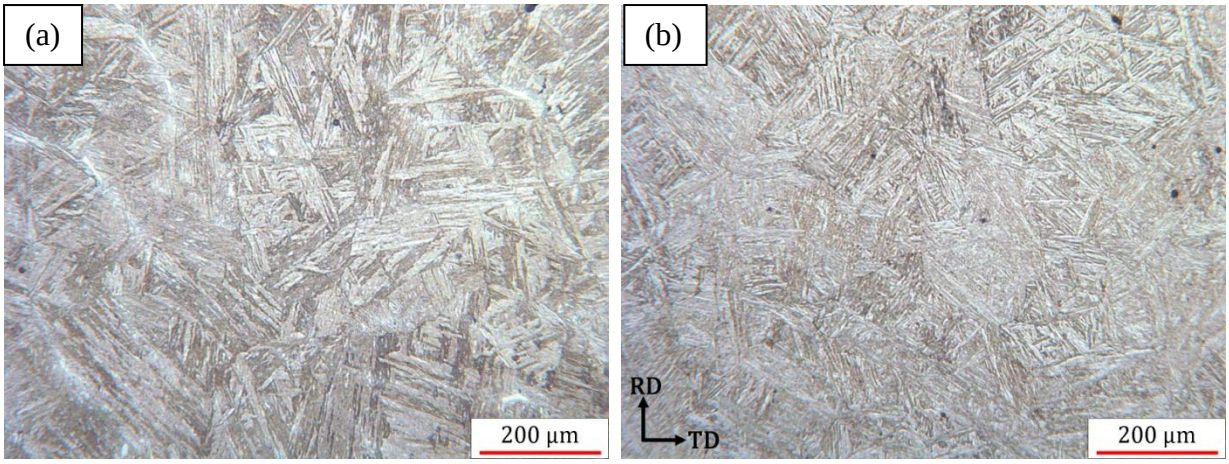

Figure 3-1: Optical micrographs of (a) CA6NM steel and (b) 415 steel

Table 3-1: Prior austenite grain size of the studied materials

Material	Cutting plane	Mean grain size (µm)
CA6NM steel	-	163.2 ± 67.2
415 steel	(T-S)	90.5 ± 34.6
	(S-L)	88.9 ± 40.1
	(L-T)	85.8 ± 38.1

Both microstructures shown in Figures 3-1 (a), and (b) consist of tempered martensite and finely-dispersed islands of reformed austenite. The austenite phase in the martensite matrix is so fine that it cannot be observed by optical microscopy; higher magnifications are needed. Observations made by SEM on the same materials but from different batches showed that the austenite phase is in the form of lamellae located within the laths of the martensitic matrix [19, 32].

The initial austenite contents measured on metallographic sections of CA6NM and 415 steels are reported in Table 3-2. Both values can be considered as equal, however, the standard deviation is relatively high in the case of CA6NM steel. There is a heterogeneous distribution of reformed austenite that originates from heterogeneous concentrations of austenite-promoting elements in the cast microstructure.

Table 3-2: Initial austenite contents in the studied materials

Designation	Reformed austenite (%)
CA6NM steel	19.1 ± 6.4
415 steel	19.5 ± 2.2

Delta ferrite was only observed in the CA6NM samples. This is illustrated in Figures 3-2 (a) and (b). Parallel elongated traces of delta ferrite are displayed in (a) while stringers of delta ferrite are observed along the prior austenite grains in (b).

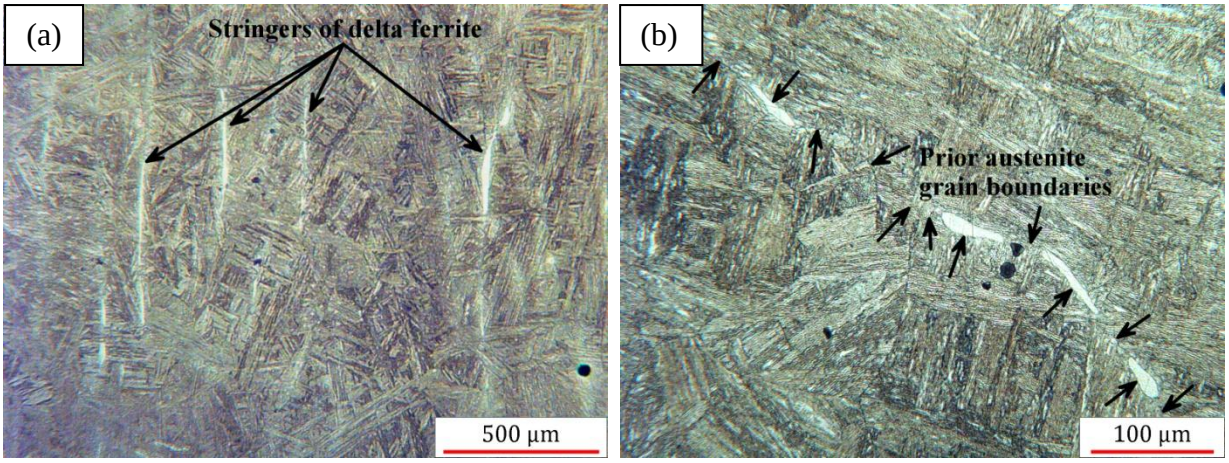

Figure 3-2: Optical micrographs of delta ferrite traces in CA6NM steel; (a) Parallel elongated traces, and (b) stringers along the prior austenite grains

The surface density, volume fraction, mean diameter, and inclusion average spacing of CA6NM and 415 steels are shown in Table 3-3. Higher density and larger size of inclusions were resulted to a higher inclusion volume fraction in CA6NM steel. The surface density of inclusions is about 35% higher for CA6NM steel whereas its volume fraction is more than twice as much as that of 415 steel. The calculated inclusion spacings in both steels are approximately equal. Note that the measured area fraction of inclusions were directly used as the volume fraction sine the area fraction of the phase of interest is equal to its volume fraction [85]. In this study, the inclusion volume fractions were measured with a high degree of accuracy since an automatic image analyzer software was used (more details are given in [85]).

Table 3-3: Inclusion characteristics of the base metals

Designation	Surface density (No./cm^2)	Size (mean diameter, μm)	Volume fraction (%)	λ (μm)
CA6NM steel	1630 ± 368	9.98 ± 8.62	0.22 ± 0.12	37.07 ± 5.73
415 steel	1210 ± 242	7.18 ± 6.42	0.09 ± 0.02	36.05 ± 3.68

Size distributions of inclusions on the metallographic sections of the studied materials are shown in Figure 3-3. The relative frequency of inclusions having diameters of more than 10 μm in CA6NM steel is more than twice as much as those in 415 steel (31% vs. 14%).

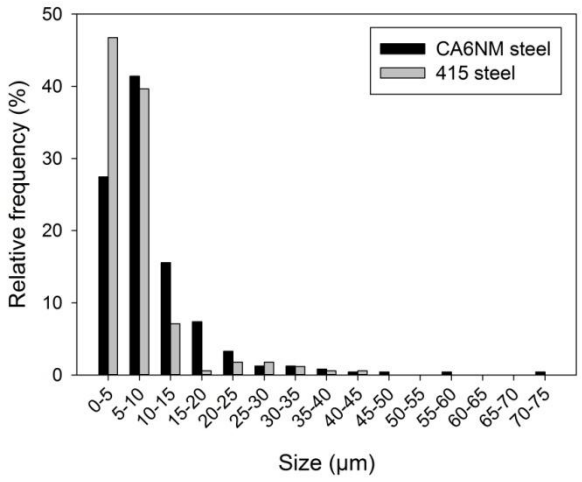

Figure 3-3: Size distributions of inclusions measured on metallographic sections

3.2 Tensile properties

Tensile curves of the base metals are shown in Figure 3-4. The tensile properties of the two steels and ASTM requirements are shown in Table 3-4. All of the results substantiate the standard requirements. However, the yield and tensile strengths of CA6NM steel are only slightly higher than the standard minimum values (25 MPa and 14 MPa, respectively). The 415 steel has a higher ductility than the CA6NM steel. Both elongation at fracture and reduction of area are larger in 415 steel. There is no strong anisotropy in this wrought steel since RD and TD properties are close to each other.

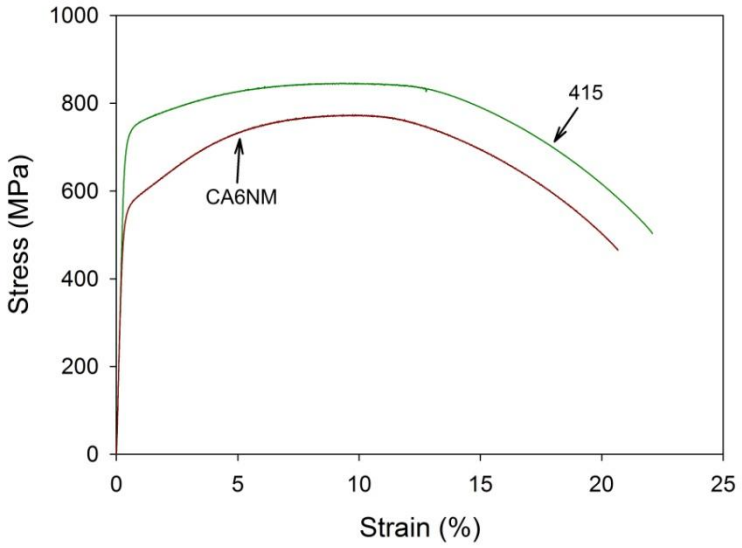

Figure 3-4: Tensile curves of the base metals

Table 3-4: Tensile properties and ASTM requirements for CA6NM and 415 steels.

Designation	0.2% σ_y (MPa)	σ_{UTS} (MPa)	e_u (%)	e_f (%)	Reduction of Area (%)
CA6NM steel	575 ± 13	769± 7	9.5 ± 0.4	19.4 ± 1.7	63.0 ± 3.8
ASTM A743 (min) [29]	550	755	-	15	-
415 steel (RD)	725 ± 0	843 ± 4	9.3 ± 0.4	21.7 ± 1.0	70.4 ± 1.8
415 steel (TD)	705 ± 9	835 ± 7	8.6 ± 0.6	19.8 ± 0.3	71.0 ± 1.4
ASTM A240 (min) [77]	620	795	-	15	-

3.3 Fracture toughness

3.3.1 J_{Ic} and CVN properties

J-Δa plots and fracture toughness J_{Ic} and the equivalent K_{Ic} values of the base metals are shown in Figure 3-5 and Table 3-5, respectively. Since the slope of 0.2 mm offset line depends on the sum of the yield strength and the tensile strength (see section 1.3.2), there are two offset lines in this figure (one for CA6NM steel, and one for 415 steel). One test was rejected for each material since crack straightness requirements were violated. In the case of 415 steel, COD predicted crack lengths requirements were also severely violated, and the data points are not shown in Figure 3-5. In the case of CA6NM steel, the resistance curves are very similar and the tests are very reproducible. The resistance curves are also similar for the wrought steel and the tests have a good reproducibility, but the difference is more pronounced in the cast steel. The J_{Ic} test carried out in T-L orientation, gave fracture toughness J_{Ic} and K_{Ic} equivalent of 437 kJ/m^2 and 310 MPa√m, respectively (Table 3-5). Therefore, similar to the tensile properties, no significant anisotropy is observed between L-T and T-L orientations in terms of fracture toughness. As can be seen in Table 3-5, the wrought steel has higher fracture toughness than the cast one.

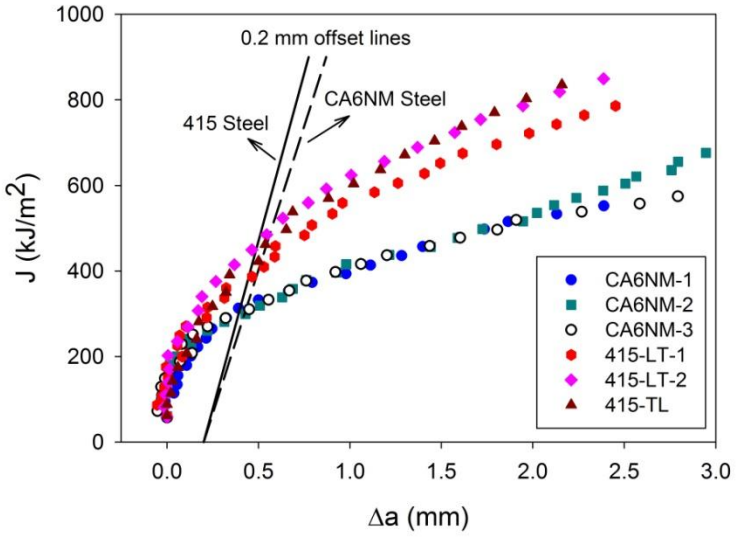

Figure 3-5: J-Δa plots of the base metals tested in this study

CVN ductile-brittle transition curves of the two steels are shown in Figure 3-6. Both steels show approximately similar transition and lower shelf behaviors but large differences are observed in the upper shelf region. The upper shelf CVN fracture energy is 49% higher for 415 steel. In a similar way, the fracture toughness J_{Ic} value of 415 steel is 39% higher than that of CA6NM steel, as provided in Table 3-6.

Table 3-5: Fracture toughness J_{Ic} and the equivalent K_{Ic} values of the base materials

Material	Test	J_{Ic} (kJ/m^2)	K_{Ic} ($MPa\sqrt{m}$)
CA6NM steel	CA6NM-1	308	260
	CA6NM-2	290	252
	CA6NM-3*	296	255
415 steel L-T	415-LT-1	366	284
	415-LT-2	466	320
	415-LT-3**	183	201
415 steel T-L	415-TL	437	310

*-Non-valid test since crack straightness requirements were violated.

**-Non-valid test because crack straightness and predicted crack lengths requirements were severely violated (due to a large macroscopic defect stopping the fatigue crack).

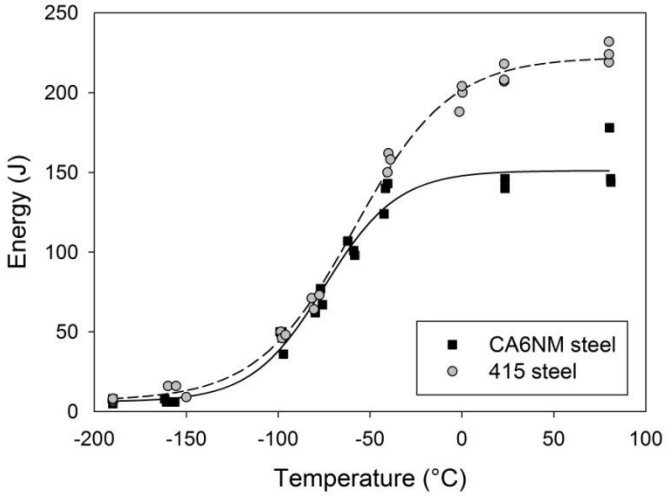

Figure 3-6: CVN ductile-brittle transition curves of CA6NM and 415 steels

Plane strain fracture toughness, CVN upper shelf fracture energies, tensile strengths, and ductilities of the studied materials are given in Table 3-6. Fracture toughness values of 415 steel correspond to the tests performed in L-T orientation. Both steels have high fracture toughness values and high upper shelf CVN fracture energies. 415 steel which has the highest ultimate tensile strength, also has the highest CVN fracture energy and fracture toughness J_{Ic}. Regarding a qualitative definition of fracture toughness which is the area under stress-strain curve of the tensile test, fracture toughness of a material can be considered as a combination of the yield strength, tensile strength, and the ductility [38]. This is in a good agreement with the measured J_{Ic} values since 415 steel has a higher fracture toughness J_{Ic}, and a higher combination of the tensile strength and the ductility than those of CA6NM steel (Table 3-6).

Table 3-6: Plane strain fracture toughness properties, CVN fracture energies, and tensile properties of the studied materials

Material	J_{Ic} (kJ/m^2)	K_{Ic} (MPa$\sqrt{m}$)	CVN (J)	0.2% σ_y (MPa)	σ_{UTS} (MPa)	e_f (%)
CA6NM steel	299 ± 13	256 ± 6	142 ± 3	575 ± 13	769 ± 7	19.4
415 steel	416 ± 71[1]	302 ± 25[1]	211 ± 6[1]	725 ± 0[2]	843 ± 4[2]	21.7[2]

[1]Measured in L-T orientation.

[2]Measured in RD.

3.3.2 Spread of the TRIP effect

The evolution of austenite content with the distance from J_{Ic} fracture surface of 415 steel is shown in Figure 3-7. It confirms the presence of the TRIP effect as it was already reported in [1-3, 15, 19] for 13% Cr-4% Ni martensitic stainless steels. The solid line shows the initial austenite content measured on metallographic sections of the as-received material and the dashed lines show its maximum and minimum values. Measurements have been taken every two millimeters until a constant value (the initial austenite content of the material) is reached. This determines the region where the austenite had transformed into martensite by TRIP effect. Three measurements have been done at a given distance.

In the case of CA6NM steel, due to a large variation in the measurements, no clear plateau was found and the estimation of the TRIP effect region was not possible. On the other hand, the homogeneous distribution of the reformed austenite in the microstructure of 415 steel provides the opportunity to estimate the extent of the region where the austenite had transformed into

martensite by TRIP. As shown in Figure 3-7, the values measured from 6 mm to 14 mm correspond to the initial austenite content of 415 steel and, it can be concluded that TRIP effect occurs down to a depth of 6 mm. Elastic-plastic FEM analysis made by Chen [83] showed that the TRIP effect occurred in the major part of the plastic zone where enough deformations took place.

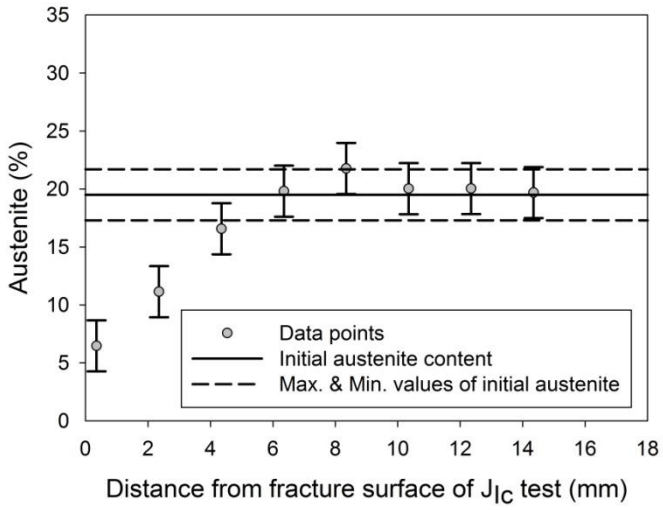

Figure 3-7: Evolution of γ content from J_{Ic} fracture surface of 415 steel

3.4 Fractographic examinations

3.4.1 Tensile tests

Typical fracture surfaces of CA6NM and 415 steels are shown in Figures 3-8 (a) and (b), respectively. Both fracture surfaces represent dimpled rupture, but their appearances are different. In the case of CA6NM steel, the fracture surface only consists of dimples, while the void sheets are also observed in 415 steel. In the right image, a secondary crack was formed due to the coalescence of some micro-voids. This crack propagated and connected the other micro-voids by void sheets formation.

The inclusion size measured on the fracture surfaces is provided in Table 3-7. The mean diameter is 25% larger than that measured on metallographic sections (Table 3-3) in the case of CA6NM steel. Contrarily, inclusions half as large as those measured on metallographic sections are found on the 415 steel fracture surfaces.

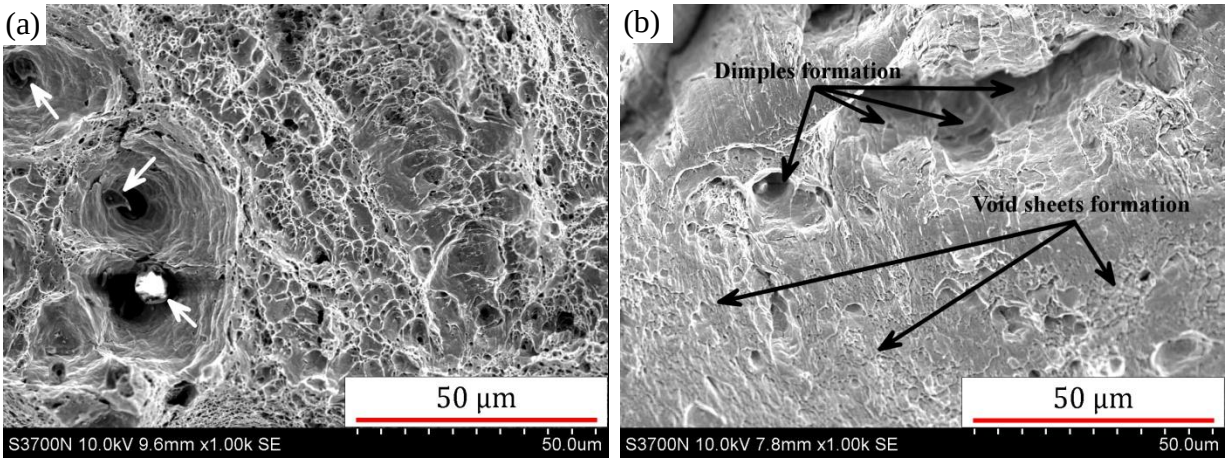

Figure 3-8: Tensile test fracture surfaces of (a) CA6NM steel and (b) 415 steel; some intact/broken inclusions and micro-voids are shown by the arrows

Table 3-7: Inclusion size measured on fracture surfaces of tensile test samples

Material	Number of measured inclusions	Size (mean diameter, µm)
CA6NM steel	49	12.47 ± 8.30
415 steel	30	3.60 ± 2.24

The size distributions of inclusions measured on the tensile test fracture surfaces of CA6NM and 415 steels are shown in Figure 3-9. Fifty five percent of inclusions are of more than 10 µm in diameter in the case of CA6NM steel, whereas the relative frequency of these large inclusions is only 3% in the case of 415 steel.

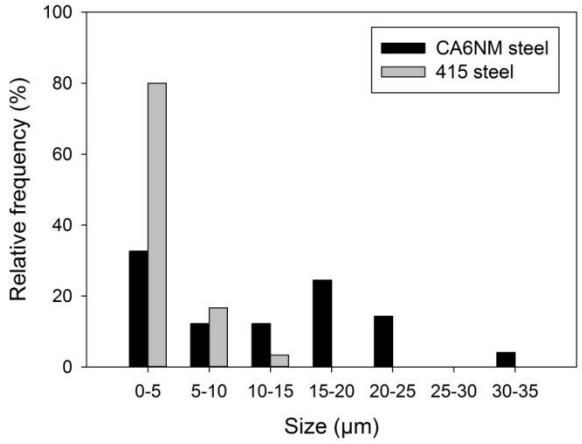

Figure 3-9: Size distributions of inclusion measured on tensile tests fracture surfaces

On the other hand, it is interesting to mention that all inclusions observed on 415 steel fracture surfaces were intact whereas some were fractured on CA6NM steel fracture surfaces. It shows that there is only one operating mechanism for dimple nucleation on 415 steel i.e., decohesion of matrix-inclusion, but another source of micro-void nucleation on CA6NM steel is the fracture of inclusions.

3.4.2 Fracture toughness J_{Ic} and CVN tests

Typical regions from the J_{Ic} fracture surfaces of CA6NM and 415 steels are shown in Figures 3-10 (a) and (b), respectively. Both fracture surfaces are typical of dimpled rupture. The dimples are significantly larger in CA6NM steel. Broken inclusions as well as intact ones are observed on the CA6NM steel fracture surface, whereas all inclusions observed on the 415 steel fracture surface have been found to be intact.

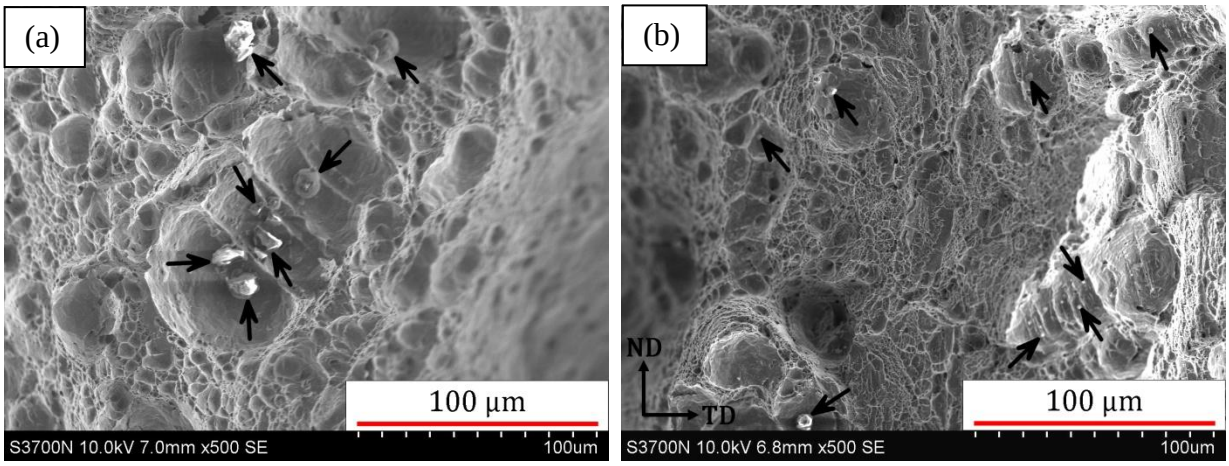

Figure 3-10: J_{Ic} fracture surfaces of (a) CA6NM steel and (b) 415 steel; some intact/broken inclusions are shown by the arrows

Regions from the CVN fracture surfaces of the tested materials at 23 °C are shown in Figures 3-11 (a) and (b). The fracture surfaces are very similar to the J_{Ic} ones in terms of inclusion size and dimples nucleation. As provided in Table 3-8, the inclusion size is also similar between J_{Ic} and CVN fracture surfaces for a given material; however, the inclusion size is at least 3 times larger in CA6NM steel.

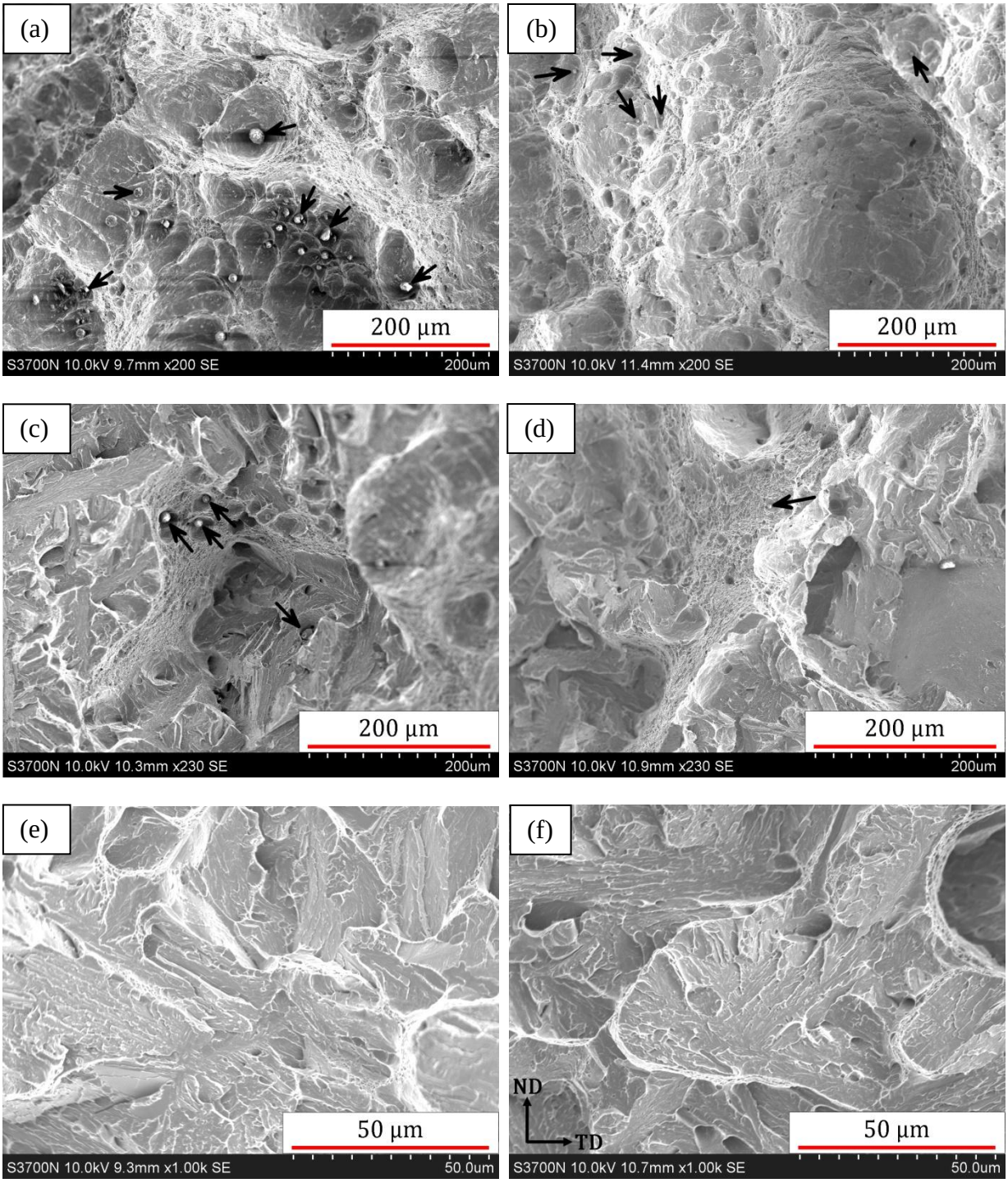

Figure 3-11: CVN fracture surfaces of CA6NM (a, c, e) and 415 (b, d, f) steels tested at 23 °C, -80 °C, and -190 °C; some intact/broken inclusions are shown by the arrows in (a) to (d)

Table 3-8: Inclusion size measured on the fracture surfaces of J_{Ic} and CVN tests (performed at room temperature)

Material	Test	Number of measured inclusions	Size (mean diameter, µm)
CA6NM steel	J_{Ic}	40	12.66 ± 6.75
	CVN	29	14.83 ± 5.89
415 steel	J_{Ic}	46	3.93 ± 2.73
	CVN	35	4.42 ±1.15

The distributions of inclusion sizes measured on the J_{Ic} and CVN tests fracture surfaces performed at room temperature are shown in Figures 3-12 (a) and (b), respectively. In the similar manner as the tensile tests, inclusions of more than 10 µm in diameter were much more numerous on J_{Ic} and CVN fracture surfaces of CA6NM steel (63% and 79%, respectively) than those on J_{Ic} and CVN fracture surfaces of 415 steel (2% and 0%, respectively). A comparison between these inclusion sizes measured on J_{Ic} and CVN fracture surfaces, and those measured on metallographic sections (Table 3-3) shows that the dimples are mostly nucleated from larger inclusions on CA6NM steel, whereas smaller inclusions act as nucleation sites for 415 steel dimples suggesting that the density of large inclusions may control the fracture process.

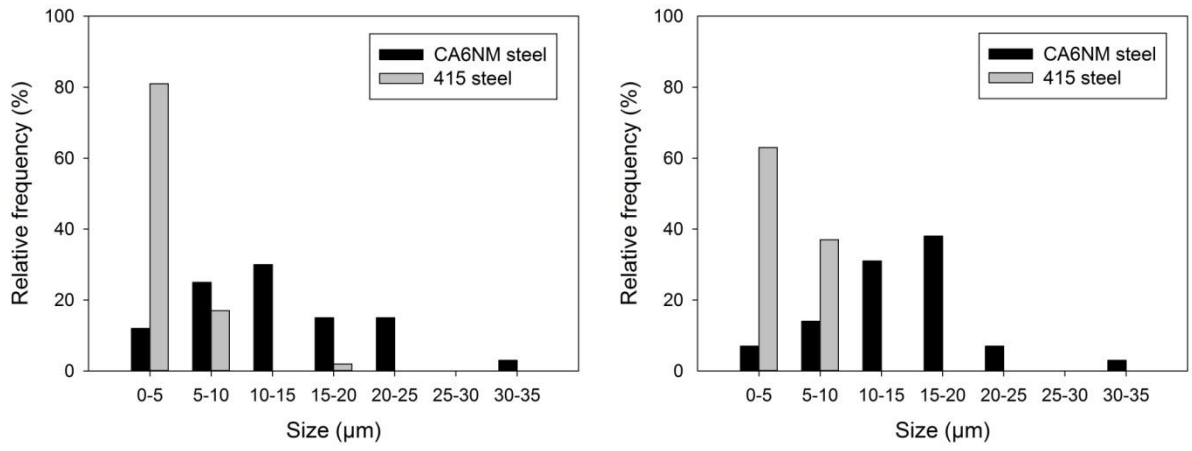

(a) (b)

Figure 3-12: Size distributions of inclusions measured on (a) J_{Ic} and (b) CVN fracture surfaces

In Figure 3-11, micrographs (c) to (f) are also added to study the mechanisms involved in the tests carried out at -80 °C and -190 °C. Semi-cleavage (formation of dimples + cleavage rupture) and pure cleavage fractures are found in both steels for the tests carried out at -80 °C, and

-190 °C, respectively. For semi-cleavage fracture mode at -80 °C (micrographs (c) and (d)), larger inclusions are observed again on the CA6NM steel fracture surface.

3.4.3 Inclusion types

All inclusions observed on fracture surfaces were spherical, except some elongated ones found in CA6NM steel. Overall 5 elongated inclusions of about 60 µm in length among hundreds of spherical ones observed on tensile, J_{Ic}, and CVN fracture surfaces. A summary of the types of inclusions detected on fracture surfaces is given in Table 3-9. Inclusions are categorized in three main types: Si-rich, Mn-rich, and Al-rich components. Silicon oxide is the dominant component of Si-rich type. However, remarkable amounts of manganese sulfide (MnS) also exist in this type of inclusion. The major part of Mn-rich inclusions is composed of MnS; some inclusions of this type could be considered as MnS, but portions of silicon oxide and aluminum oxide are found in most of these inclusions. An important portion of Al-rich inclusions consists of aluminum oxide; large amounts of magnesium oxide and calcium oxide were also detected in the inclusions of this type. Very low amounts of MnS are detected in Al-rich inclusions.

Table 3-9: Types of inclusions detected on the fracture surfaces of the base metals

Material	Test	Inclusion type		
		Si – rich component	Mn-rich component	Al – rich component
CA6NM steel	Tensile	✓	✓	
	J_{Ic}	✓	✓	
	CVN	✓	✓	
415 steel	Tensile	Not detected*		
	J_{Ic}			✓
	CVN			✓

* Due to the small size of inclusions and inclusion/dimple wall overlapping, precise detection of inclusion types was not possible.

Briefly, the major differences between the types of inclusions detected in CA6NM steel and 415 steel are the proportions of these three types of oxides. Silicon oxide as well as MnS is the dominant components of CA6NM steel inclusions whereas the majority of 415 steel inclusions are of aluminum oxide.

SEM micrographs of Si-rich and Mn-rich complex inclusions observed in CA6NM steel as well as their EDX chemical spectrums are shown in Figures 3-13 (a) and (b), respectively.

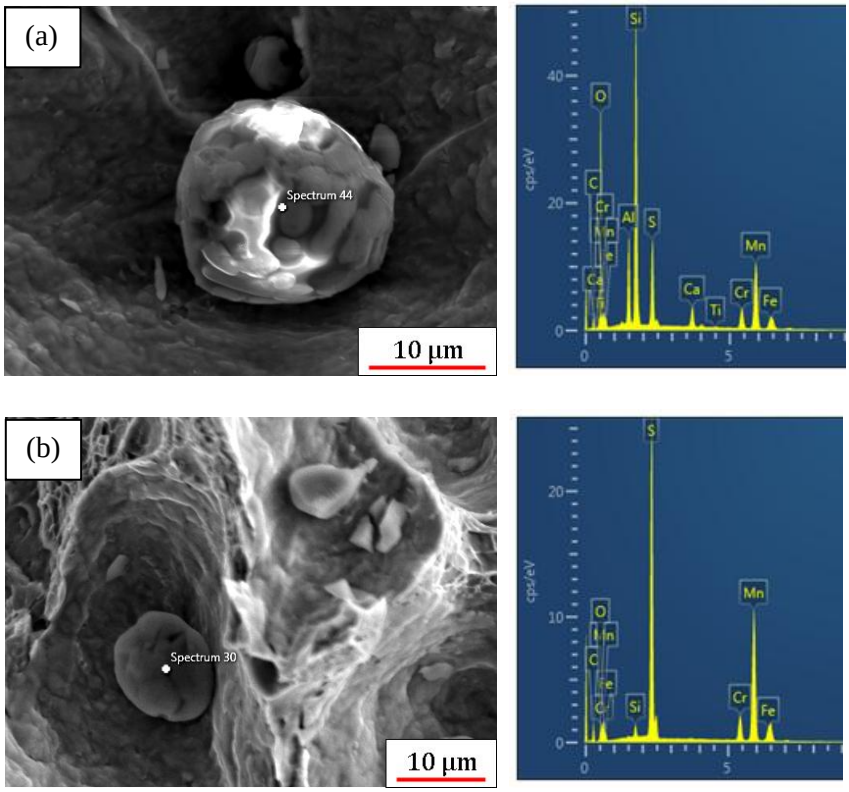

Figure 3-13: Typical complex inclusions observed on the fracture surfaces of CA6NM steel with EDX spectrums at the right: (a) Si-rich inclusion and (b) Mn-rich inclusion

3.5 Discussion

The main purpose of this section is to discuss the superior mechanical properties of the 415 steel based on the microstructural features. An increase of 75% in the carbon content of the 415 steel (Table 3-1) can be a reason why its strength is higher than that of the CA6NM steel since yield stress of martensite is proportional to the square root of solid solution carbon atoms [11, 40].

On the other hand, prior austenite grain size is 45% finer in the 415 steel, as shown in Table 3-1, however, the ductility is not highly affected by grain refinement as reported in [40], and based on investigations by Stonsifer and Armstrong [51], this 45% decrease should only result in an increase of 3% in the fracture toughness K_{Ic}. The finer microstructure in the 415 steel cannot be the main reason for 12%, 39% and, 49% improvements in elongation at fracture, fracture toughness J_{Ic}, and CVN fracture energy, respectively. On the other hand, no carbide (broken or intact) was observed on the tensile, fracture toughness J_{Ic}, and CVN fracture surfaces. Therefore, it can be concluded that these are only inclusions that initiate micro-voids and the role of carbides

can be ignored. Inclusions play a major role in the ductile fracture of metals and differ in content, size, and nature between the two base metals. In order to shed light on how these differences affect the mechanical properties, their behaviors during rupture will be discussed below.

The fracture mechanism of all the tests carried out at ambient temperature was micro-void coalescence for both steels, However, SEM micrographs showed that the main differences between the two steels in their fracture appearances at microscopic scale are the inclusion size distribution (Figure 3-9 and Figure 3-12), including the inclusion size (Table 3-7 and Table 3-8), the existence of intact or broken inclusions, and the nature of inclusions (Table 3-9). Large inclusions of more than 10 μm in diameter were readily observed on CA6NM steel fracture surfaces whereas these inclusions were rarely detected on 415 steel fracture surfaces. The local densities of these large inclusions measured on tensile, J_{Ic} and CVN fracture surfaces were 55% (Figure 3-9), 63% (Figure 3-12 (a)), and 79% (Figure 3-12 (b)), respectively, in the case of CA6NM steel, but their existence could be considered as negligible (3% or less) on 415 steel fracture surfaces. In addition, the formation of dimples was facilitated by the rupture of inclusions [6] in CA6NM steel. Large dimples besides very fine ones existed on CA6NM fracture surfaces, whereas uniform dimple distributions were observed in the case of 415 steel. Therefore, the premature formation of micro-voids on inclusions broken during loading and on intact inclusions of more than 10 μm in diameter occurred in a large number in the case of CA6NM steel. These micro-voids grew and became larger as deformation increases; at a certain deformation level, a second series of micro-voids nucleated from smaller inclusions. At this stage, large micro-voids were connected together by smaller ones i.e., micro-void coalescence occurred and final rupture took place. On the other hand, in the case of 415 steel, the number of inclusions of more than 10 μm in diameter is very low, and the only way for micro-void formation is the decohesion of the matrix-inclusion interface. In other words, it can be said that most inclusions in 415 steel have more or less the same chance for micro-void nucleation. As a result, the formation of micro-voids occurred on most inclusions at approximately the same strain level. Hence, more uniform dimples were formed and the local inclusion density may control the fracture mechanism.

Briefly, the inclusion sizes given in Table 3-3 (measured on metallographic sections) are different from that provided in Table 3-7 and Table 3-8 (measured on tensile, J_{Ic}, and CVN fracture surfaces). In the case of CA6NM steel, this difference shows that large inclusions (larger than 10

μm) drive the rupture as they are the basis of dimples initiated at lower strains. On the other hand, in 415 steel, large inclusions seem not to play an essential role on void nucleation and it is rather the frequency of inclusions that drives the nucleation mechanism as numerous inclusions smaller than 10 μm in diameter were found on 415 steel fracture surfaces. The higher density of particles on fracture surfaces than on a random surface generated in the alloy suggests that the local inclusion density, and not the inclusion size, may have controlled the fracture mechanism in 415 steel.

According to the above discussion, it can be said that a high frequency of premature micro-voids formation in CA6NM steel decreased the elongation at fracture, the fracture toughness J_{Ic}, and the CVN fracture energy. On the contrary, the formation of micro-voids on smaller inclusions retard their formation and growth at higher strains increasing the elongation at fracture, the fracture toughness J_{Ic} and the CVN fracture energy values of 415 steel.

For the CVN tests performed at -80 °C (Figures 3-11 (c) and (d)), cleavage is dominant and few dimples were observed among cleavage facets. MVC was happening between regions that generate cleavage facets, but the amount of ductile fracture is negligible. On the other hand, at -190 °C, as shown in Figure 3-6, both steels absorb the same fracture energy, and fractures occurred by pure cleavage despite of larger inclusions in CA6NM steel, as shown in Figures 3-11 (e) and (f). Cleavage crack propagation occurs along favorably oriented crystallographic planes [6]. Therefore, even at low temperatures, there can be some misoriented regions which cannot produce cleavage. These regions break at the final stage of rupture with dimples features, and the most important part of the energy is absorbed during the growth of these dimples [86].

However, inclusions act for the initiation stage as stress raisers and the inclusion size does not play a significant role and this is only the shape which contributes to rupture, since very small plastic deformation is required for cleavage. Nearly the same fracture energy was observed in the cases of the tests performed at -80 °C and lower (Figure 3-6), it can be concluded that different inclusion size of CA6NM and 415 steels did not affect the fracture energy.

There still remains one question; what is the contribution of the different nature of inclusions detected on CA6NM and 415 steels fracture surfaces? Both large inclusions of more than 10 μm in diameter and small ones (those of less than 10 μm in diameter) were found to be broken on CA6NM steel fracture surfaces. These broken inclusions were Si-rich and Mn-rich. All inclusions

were Al-rich on 415 steel fracture surfaces and even large ones were intact (not broken). Therefore, it seems that the low resistance of Si-rich and Mn-rich inclusions against rupture promote micro-void formation since rupture of inclusions makes the micro-void nucleation easier [6]. It has been shown that MnS promote micro-void nucleation [87]. Therefore, it seems that the hight amounts of MnS in the Si/Mn-rich inclusions (see section 3.4.3) were eventually promoted the lower resistance of these types of inclusions. Accordingly, it can be said that the absence of low resistant inclusions also contributed to improve the mechanical properties of the 415 steel.

3.6 Conclusions

The main purpose of this chapter was to characterize the effects of microstructure and inclusion characteristics on the mechanical properties of a cast and a wrought 13% Cr-4% Ni martensitic stainless steels. Tensile, fracture toughness J_{Ic}, and CVN tests were performed. The size, surface density, volume fraction, and spacing of inclusions were determined on metallographic sections. The size and the nature of inclusions were determined on fracture surfaces using SEM-EDX. Austenite contents were measured on metallographic sections as well as below J_{Ic} fracture surfaces using XRD. The following conclusions have been drawn:

- As compared to the wrought steel, the CA6NM steel has higher surface density and mean diameter of inclusions. The inclusion volume fraction is about 2.5 times higher, whereas the calculated inclusion spacing is approximately equal for both steels.
- The yield stress, tensile strength, elongation at fracture, fracture toughness J_{Ic}, and CVN fracture energy (at room temperature) of the cast steel are all lower than those of the wrought one.
- For both steels, dimpled rupture occurs for the tests carried out at room temperature. The fracture modes for low temperature CVN tests are a mix of dimples and cleavage, and pure cleavage, however, cleavage is the dominant mechanism and both steels absorb the same fracture energies.
- The inclusion size measured on fracture surfaces is at least three times larger in the case of the cast steel. The majority of inclusions detected on fracture surfaces of tensile, J_{Ic}, and CVN tests are larger than 10 µm. On the contrary, almost all the inclusions on the wrought steel fracture surfaces have diameters smaller than 10 µm.

- Si/Mn-rich and Al-rich complex inclusions are the two main types of defects detected on the fracture surfaces of the cast and the wrought steels, respectively. The Si/Mn-rich inclusions are ruptured, whereas Al-rich inclusions are found to be intact in the case of the wrought steel. The Si/Mn-rich inclusions were found to have a lower resistance against rupture and against micro-void nucleation as compared to Al-rich inclusions. Ruptured Si/Mn-rich inclusions and those having diameters larger than 10 μm are the main sites of micro-void nucleation in the cast steel. Inversely, micro-voids nucleate from intact Al-rich inclusions which nearly all of those are of less than 10 μm in diameter in the case of the wrought steel.
- The higher mechanical properties of the wrought steel are come from a lower inclusion volume fraction, more numerous inclusions having diameters lower than 10 μm, and a more resistant inclusion type (Al-rich) against rupture and against micro-void formation.
- At the crack tip in a J_{Ic} specimen, the spread of the zone where TRIP occurs in the wrought steel is about 6 mm in a direction perpendicular to the fracture surface. Outside this zone, the strains are not high enough to transform the austenite into martensite.
- The most effective way to improve the mechanical properties of castings made of 13% Cr-4% Ni martensitic stainless steels is to decrease as much as possible the volume fraction and especially the size of the non-metallic inclusions in the microstructure. Very fine inclusions homogenously dispersed and spaced as far apart as possible will result in the highest elongation at fracture, plane strain fracture toughness, and CVN fracture energies.

CHAPTER 4 RESULTS AND DISCUSSION: WELD METALS

4.1 Microstructure

The martensitic microstructures of the weld metal for the as-welded, and heat-treated conditions are shown in Figures 1-4 (a), and (b), respectively. Fresh martensite is observed in (a), and tempered one is observed in (b). Delta ferrite and austenite exist in both microstructures. The existence of delta ferrite was confirmed by Mokhtabad Amrei [28] worked on a similar weld metal deposited by FCAW process using the same filler metal wire as the one used in this study.

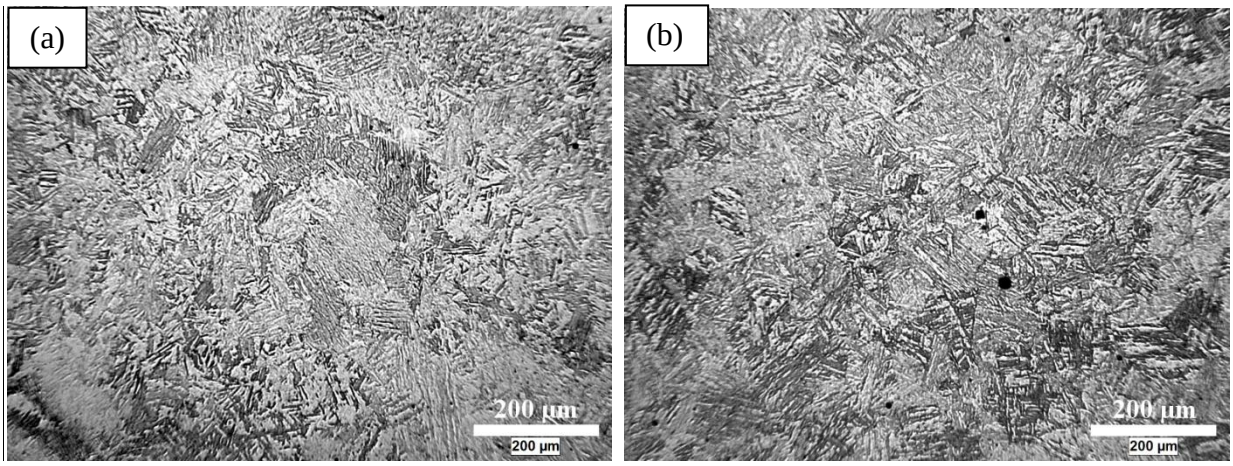

Figure 4-1: Microstructure of the weld metal in (a) the as-welded, and (b) heat-treated conditions

Due to the very small size of austenite islands, this phase cannot be observed by optical microscopy. Initial austenite contents of the weld metals measured by XRD are shown in Table 4-1.The austenite content of the tempered microstructure is four times as much as that of as-welded one. As noted in the section 2.1.2, the heat treatment performed at 600 °C for 2 hrs.

Table 4-1: Initial austenite contents of the weld metals

Designation	Austenite (%)
410NiMo-AW	2.4 ± 1.0
410NiMo-HT	10.0 ± 0.6

The surface density, volume fraction, size, and inclusion average spacing of defects in the weld metal are shown in Table 4-2. The surface density and the volume fraction of inclusions are relatively high in the weld metal. The inclusions mean diameter is smaller than one micrometer, but they are very closely spaced. It is expected that the ductility, fracture toughness J_{Ic}, and CVN

fracture energy of the weld metal were highly affected by these defects existing in the microstructure.

Table 4-2: Inclusion characteristics of the weld metal

Designation	Surface density (No./cm^2)	Volume fraction (%)	Size (mean diameter, μm)	λ (μm)
410NiMo	$(1.29 \pm 0.25) \times 10^6$	1.10 ± 0.14	0.76 ± 0.02	1.89 ± 0.10

4.2 Tensile properties

The tensile curves as well as the tensile properties of the weld metal in the as-welded (AW) and heat-treated (HT) conditions are shown in Figure 4-2 and Table 4-3, respectively. As expected, the as-welded material is more resistant but, less ductile.

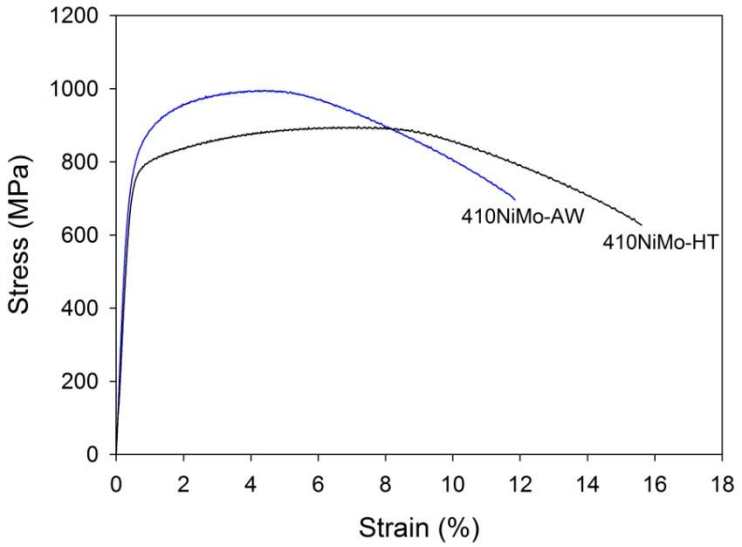

Figure 4-2: Tensile curves of the weld metals

Table 4-3: Tensile properties of the weld metals

Designation	0.2% σ_y (MPa)	σ_{UTS} (MPa)	e_u (%)	e_f (%)
410NiMo-AW	783 ± 5.8	1007 ± 10.3	4.4 ± 0.1	10.5 ± 1.2
410NiMo-HT	765 ± 5	895 ± 4	6.8 ± 0.3	15.2 ± 0.4
AWS A5.22/A5.22M (min)	-	760	-	15

4.3 Fracture toughness K_{Ic} and CVN properties

The J-R curves and plane strain fracture toughness values of the weld metal in the as-welded and heat-treated conditions are shown in Figure 4-3 and Table 4-4, respectively. The offset lines are overlapped since the yield strength and the tensile strength between the as-welded and heat-treated weld metals are close (Table 4-3). The curves show similar behaviors, and fracture toughness values show a very good reproducibility especially for the heat-treated condition for which equal values were obtained.

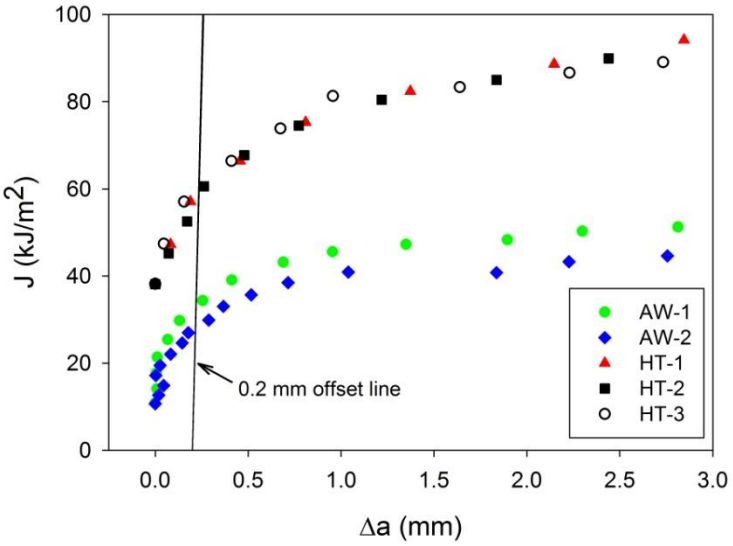

Figure 4-3: J-Δa plots of the weld metals

Table 4-4: Plane strain fracture toughness values of the weld metal in AW and HT conditions

Material	Test	J_{Ic} (kJ/m^2)	K_{Ic} (MPa√m)
410NiMo-AW	AW-1	34	86
	AW-2	28	79
	AW-3*	-	89
410NiMo-HT	HT-1	59	114
	HT-2	59	114
	HT-3**	58	113

*-Unstable crack propagation occurred (see Figure 4-4).

**-Only three data points located between the exclusion lines.

Moreover, in the J_{Ic} testing of the weld metal which had much lower fracture toughness than the base metals, unstable propagations could occur. Load-displacement curve of the preliminary J_{Ic} test of the as-welded weld metal is shown in Figure 4-4. As can be seen in this figure, the load-displacement curve falls suddenly after the second load/unload sequence since unstable crack propagation occurred. Since developing the J-R curve, and hence, determining a valid J_Q was not possible in this case, K_Q could be determined directly similar to the K_{Ic} test approach. Accordingly, as shown in Figure 4-4, an offset line of 95% of the slope of the linear part of the curve was drawn and the candidate load, P_Q, was determined. A K_Q of 89 MPa√m was obtained according to ASTM E399 [88].

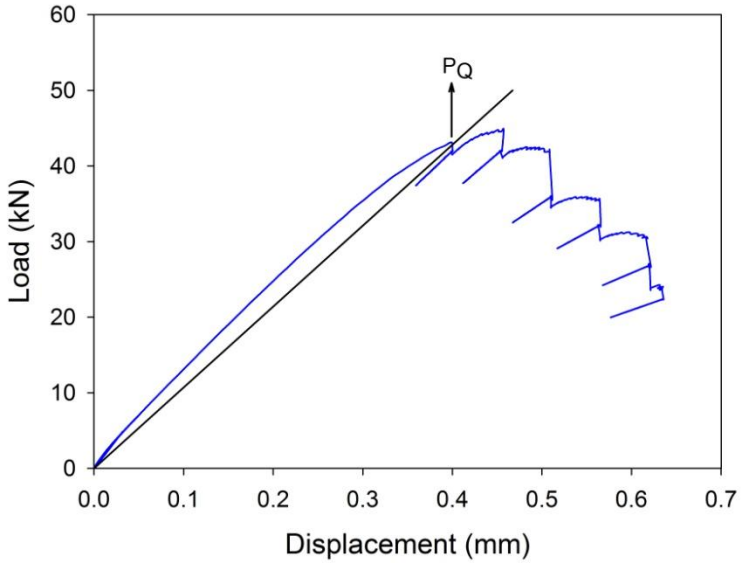

Figure 4-4: Load-displacement curve recorded during fracture toughness J_{Ic} test of the weld metal in as-welded condition

For K_Q to be qualified as a K_{Ic} value [88], two conditions have to be satisfied. The first condition to be met is that the P_{max}/P_Q ratio should be lower than 1.10, where P_{max} is the maximum load in the load-displacement graph. Therefore, unstable crack propagation is guaranteed to be occurred. This condition is satisfied since a P_{max}/P_Q ratio of 1.04 was obtained. For the second condition, the specimen has to be thick enough to satisfy the plane strain condition,

$$B \geq 2.5\left(\frac{K_Q}{\sigma_y}\right)^2 \qquad (4\text{-}1)$$

This gives a thickness of 32 mm, while a 25.4 mm thick specimen was used. It is not a large violation of the plane strain condition, and it is interesting to mention that the K_Q obtained above is close to the K_{Ic} value obtained from a J_{Ic} test (Table 4-4).

Figure 4-5 shows the CVN ductile-brittle transition curves of the weld metal in the two metallurgical states. As expected, the weld metal in heat-treated condition has higher CVN fracture energy than that in as-welded condition. The heat-treated material absorbed higher energies at all temperatures except at -190 °C where both materials absorbed equal energies.

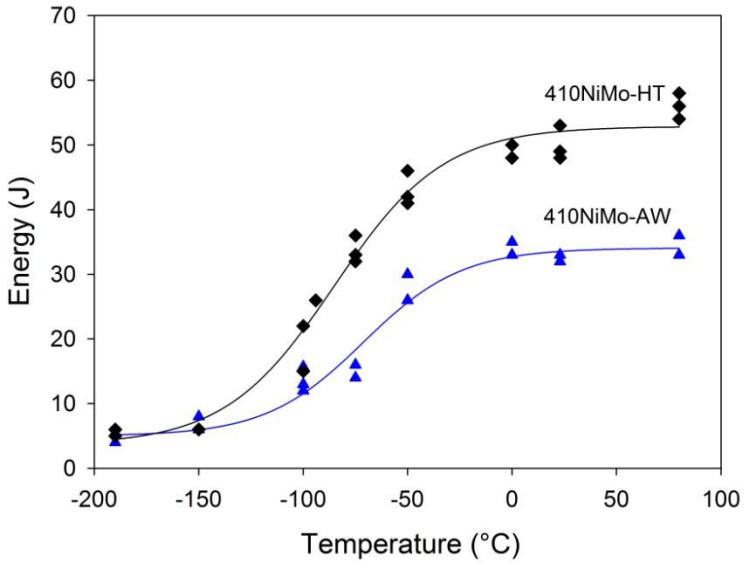

Figure 4-5: CVN ductile-brittle transition curves of the weld metal in as-welded and heat-treated conditions

Plane strain fracture toughness, room temperature CVN fracture energy and tensile properties of the weld metals in both as-welded and heat-treated conditions are provided in Table 4-5. The results show that as the tensile strength decreases, the plane strain fracture toughness and the CVN fracture energy increase. As a result of post-weld heat treatment, the fracture toughness J_{Ic} and CVN fracture energy of the weld metal in heat-treated condition increase by 90% and 56%, respectively, while there is 11% decrease in the tensile strength.

Table 4-5: Plane strain fracture toughness, room temperature CVN fracture energies, and tensile properties of the weld metals

Material	J_{Ic} (kJ/m^2)	K_{Ic} (MPa$\sqrt{m}$)	CVN (J)	σ_{UTS} (MPa)	e_f (%)
410NiMo-AW	31 ± 4	82 ± 5	32 ± 1	1007 ± 10	10.5 ± 1.2
410NiMo-HT	59 ± 0	114 ± 0	50 ± 3	895 ± 4	15.2 ± 0.4

4.4 Fractographic examinations

SEM micrographs of fracture surfaces of the tensile and J_{Ic} tests, and those of the CVN tests at room temperature of the weld metals are shown in Figures 4-6 (a) to (f). The micrographs of the as-welded condition are on the left side, and those of the heat-treated one are on the right side. The fracture mechanism observed in all micrographs is dimpled rupture. No significant differences in the fracture appearances are observed between the micrographs of the as-welded material and those of the heat-treated one. As shown in Table 4-6, the inclusion size is approximately equal in all the tests performed in both as-welded and heat-treated conditions.

Dimpled rupture was the dominant mechanism observed on the room temperature CVN fracture surfaces of the as-welded material (Figure 4-6 (e)), while some traces of cleavage fracture were also found on the fracture surfaces of the as-welded material (Figure 4-7).

CVN fractographs of the weld metal in the as-welded and the heat-treated conditions at -50 °C, -75 °C, and -190 °C are shown in Figures 4-8 (a) to (f). The fracture appearance is similar for both as-welded and heat-treated conditions at each temperature. As shown in (a) and (b), the fracture surfaces consist of a mix of dimples and cleavage. However, the dimpled rupture is still dominant at -50 °C. As shown in micrographs (c) and (d), the fracture is again a mix of dimples and cleavage at -75 °C, but the cleavage is the dominant fracture mechanism. Finally, the fracture mechanism can be considered as pure cleavage for the tests performed at -190 °C (micrographs (e) and (f)), but very small dimpled areas still observed on both micrographs.

Finally, comparing SEM micrographs of the CVN tests performed at different temperatures (Figures 4-6 (e) and (f) and Figures 4-8 (a) to (f)) with the corresponding fracture energies (Figure 4-5), it can be concluded that the fracture energy decreased as the portion of the cleavage increased.

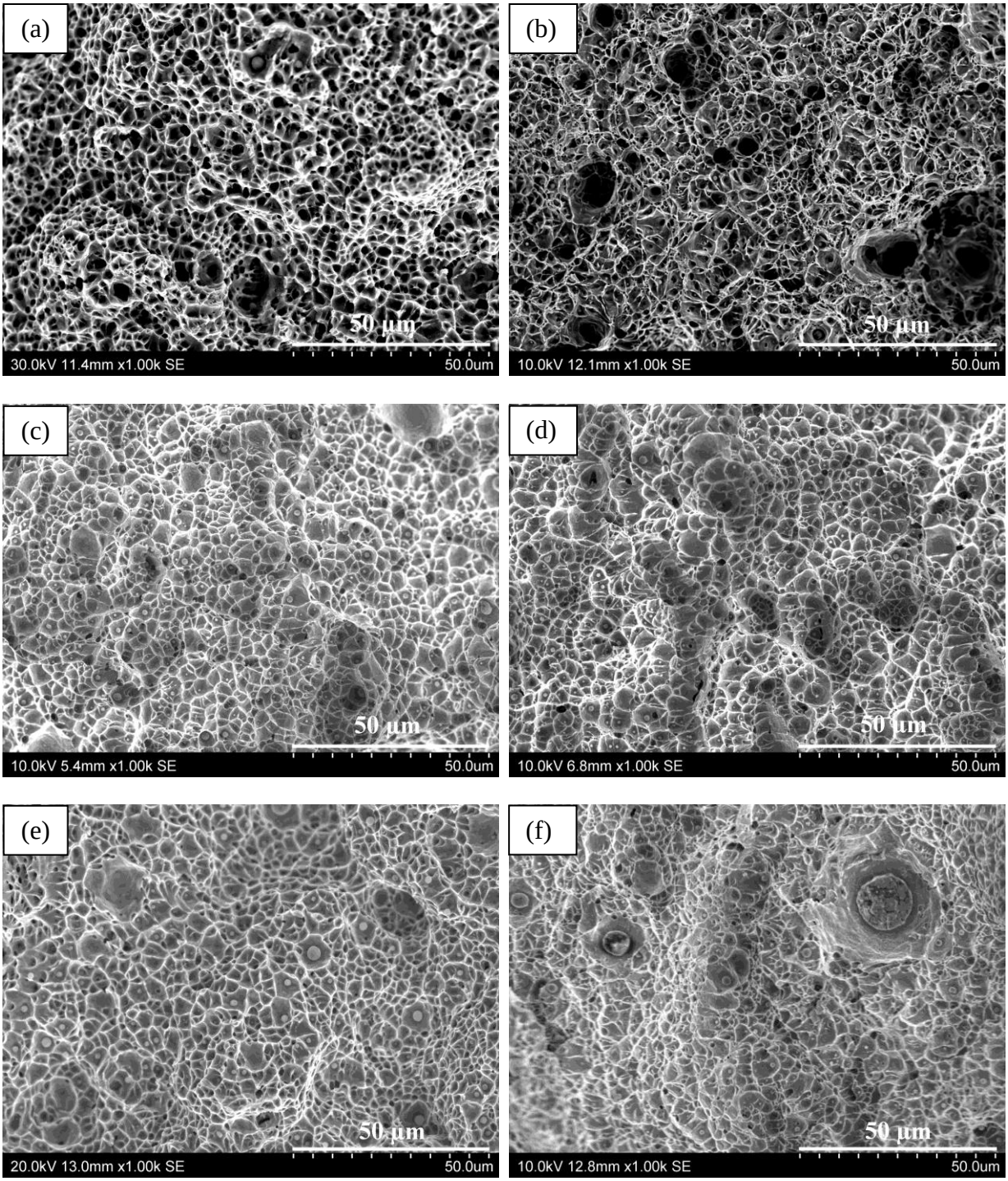

Figure 4-6: Weld metals fracture surfaces: (a, b) tensile tests, (c, d) J_{Ic} tests, and (e, f) CVN tests performed at room temperature; (a, c , e) micrographs are from the as-welded metal, and (b, d, f) micrographs are from the heat-treated one

Table 4-6: Inclusion size measured on tensile, J_{Ic} and CVN fracture surfaces

Material	Test	Number of measured inclusions	Size (mean diameter, μm)
410NiMo-AW	Tensile	35	0.86 ± 0.48
	J_{Ic}	35	0.84 ± 0.27
	CVN	35	0.94 ± 0.31
410NiMo-HT	Tensile	35	0.86 ± 0.29
	J_{Ic}	35	0.88 ± 0.37
	CVN	35	0.87 ± 0.43

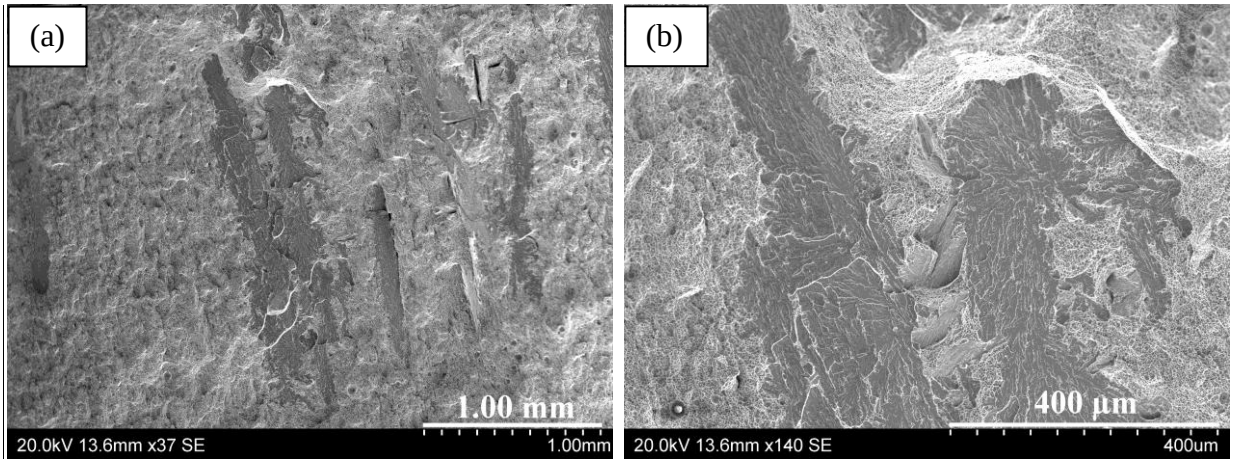

Figure 4-7: Traces of cleavage on a CVN fracture surface of the as-welded material tested at room temperature; the same location for both magnifications, (a) at 37X, and (b) at 140X.

Inclusions on the tensile, J_{Ic} and CVN tests fracture surfaces of the weld metals were examined. Inclusions detected were of complex type. The major part of these inclusions was composed of Ti, Cr, Zr, Mn and Si oxides. A complex inclusion observed on a J_{Ic} fracture surface of the weld metal in heat-treated condition as well as its EDX chemical spectrum is shown in Figure 4-9.

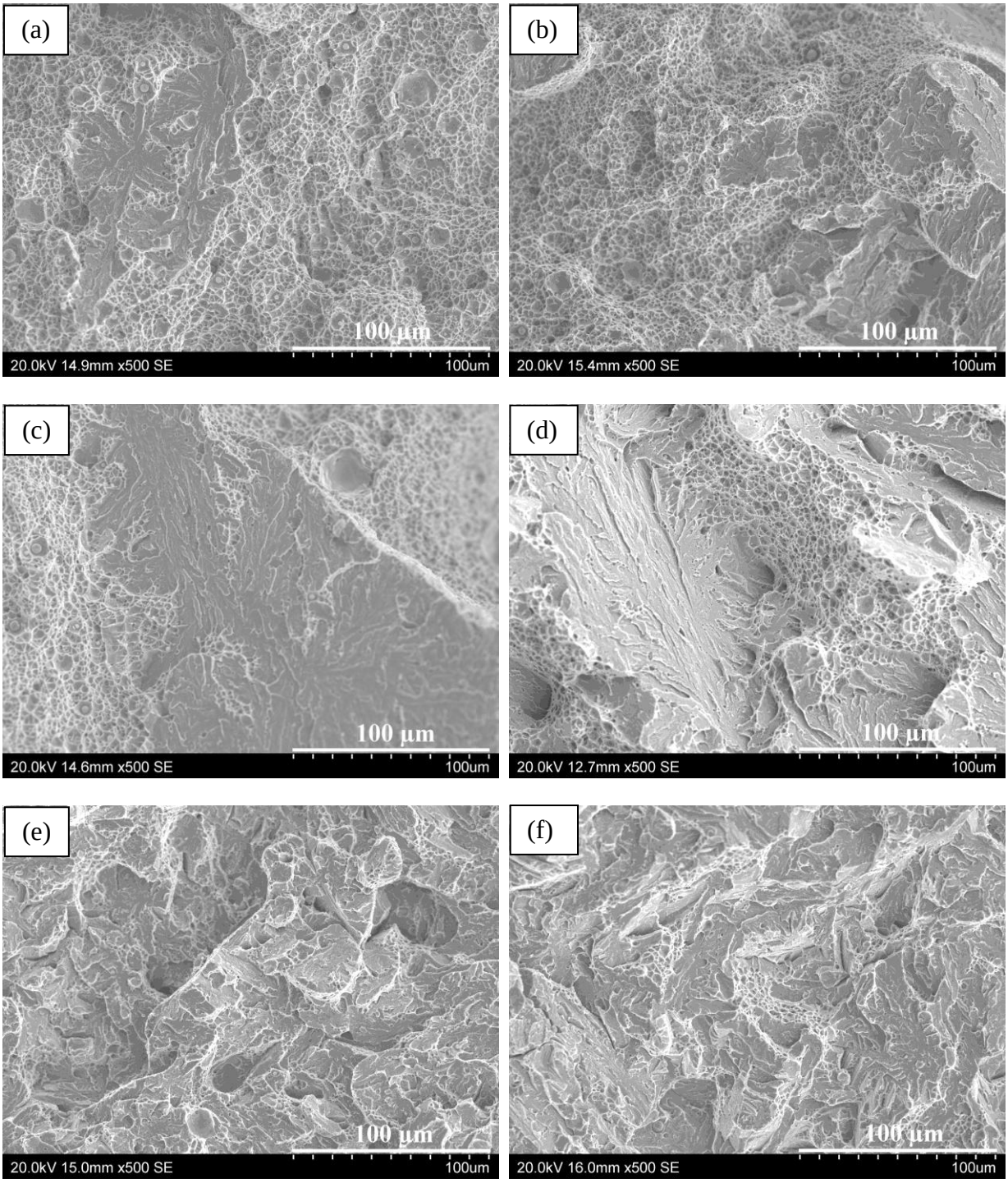

Figure 4-8: CVN fracture surfaces of the weld metal at (a, b) -50 °C, (c, d) -75 °C, and (e, f) -190 °C; (a, c, e) micrographs are from the as-welded metal, and (b, d, f) micrographs are from the heat-treated one

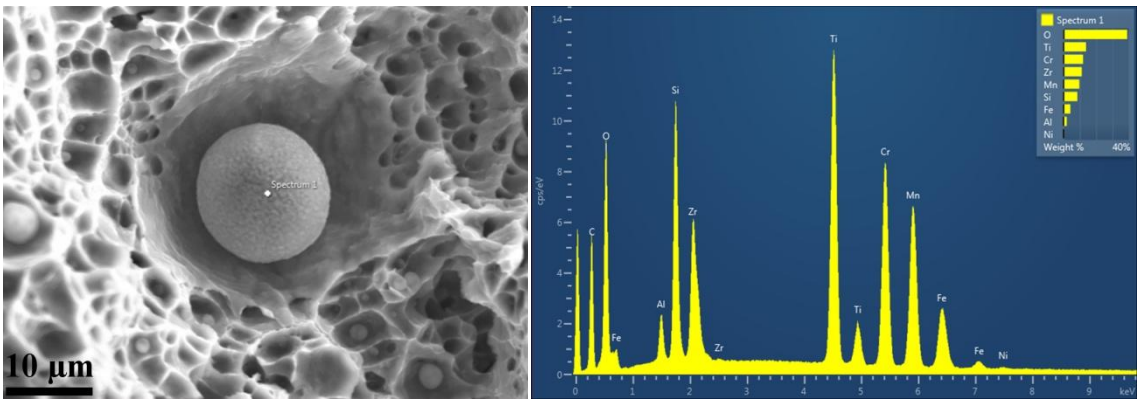

Figure 4-9: A complex inclusion observed on a J_{Ic} fracture surface of the weld metal in heat-treated condition with its EDX spectrum at the right

4.5 Discussion

As shown in Figure 4-6, the fracture mechanism was MVC for the tensile, J_{Ic}, and room temperature CVN tests in both as-welded and heat-treated weld metals. As provided in Table 4-6, the inclusion size measured on the fracture surfaces was the same for both metallurgical states, as expected. Heat treating of the weld metal did not affect the fracture appearances. Therefore, this is only the defect characteristics (Table 4-2) which affect dimpled rupture in the weld metals.

Since no carbide (broken or intact) was observed on the tensile, fracture toughness J_{Ic}, and CVN fracture surfaces of both as-welded and heat-treated weld metals, it can be concluded that these are only the inclusions that initiate the ductile rupture. As given in Table 4-2, very fine, closely spaced inclusions were found in the microstructure of the weld metal. The inclusions were smaller than one micrometer, and their spacing was lower than two micrometers. This very low inclusion spacing resulted in a premature coalescence of nucleated micro-voids during rupture. Therefore, rupture occurred without significant void growth. In other words, the void growth stage can be considered as negligible, and it can be said that MVC mechanism in the weld metal consisted of a micro-voids formation followed by a quasi-immediate coalescence.

Heat treating of the weld metal resulted in a decrease in the yield and tensile strengths by 2% and 11%, respectively (Table 4-3). On the contrary, the uniform elongation, the elongation at fracture, the fracture toughness J_{Ic}, and the room temperature CVN fracture energy were increased by 55%, 45%, 90%, and 56%, respectively (Table 4-5). Since the weld metals had the same

inclusion characteristics, the microstructural features affecting their toughnesses are the state of martensite (fresh/tempered), and the austenite content. As provided in (Table 4-1), the heat-treated weld metal had an austenite content four times higher than the as-welded one.

4.6 Conclusions

A 13% Cr-4% Ni weld metal block of 450 × 250 × 60 mm was deposited on a CA6NM steel substrate by flux cored arc welding using AWS E410NiMo tubular wire. The weld metal was tested in both as-welded and heat-treated conditions. A heat treatment process at 600 °C for two hours was used. The tensile, J_{Ic} and CVN tests were performed. The major microstructural features affecting fracture toughness J_{Ic} of the tested materials i.e., the inclusion characteristics (surface density, volume fraction, size and spacing of inclusions) and the austenite contents were examined on metallographic sections by means of optical microscopy and XRD analyses, respectively. The fracture surfaces were examined by SEM. To reveal the contribution of inclusions during rupture, inclusion sizes were also measured on the fracture surfaces. The following conclusions have been made:

- In the tensile and the J_{Ic} tests, fracture occurs totally by MVC for both as-welded and heat-treated weld metals. In the case of the CVN test, a totally dimpled rupture also occurred for the heat-treated material. Dimpled rupture was also the dominant fracture mode for the as-welded material despite traces of cleavage fracture on its CVN fracture surfaces.
- The fracture mode changes from a mix of dimples and cleavage to pure cleavage as the test temperature decreases from transition region to lower shelf region for both materials.
- There are a high volume fraction and high surface density of inclusions in the weld metal microstructure. The inclusions are very fine and very closely spaced.
- Micro-voids formed in very large numbers in both as-welded and heat-treated materials during ductile rupture. A premature coalescence of the nucleated micro-voids was observed without significant growth.
- Heat treating at 600 °C for two hours is an effective way to obtain a good combination of strength, ductility and fracture toughness; uniform elongation and elongation at fracture

are increased by 45% and 55%, respectively, while the yield stress is decreased by only 2%; fracture toughness J_{Ic} is improved by a factor of two.

- Ti-rich, Zr-rich, Si-rich and Mn-rich complex inclusions were detected on the weld metal fracture surfaces.

CHAPTER 5 CONFRONTATION OF THE RESULTS AND FRACTURE TOUGHNESS IN THE HAZ

The effect of microstructural features on the mechanical properties of the 13% Cr-4% Ni martensitic stainless steels and their matching weld metal tested in this study is discussed in this chapter. The main purpose of this chapter is to explain the large differences existing between the mechanical properties of the base metals and the weld metals despite similar chemical compositions with respect to the microstructural features mentioned above. An empirical K_{Ic}-CVN correlation covering wide ranges of CVN fracture energies and fracture toughness K_{Ic} is proposed for 13% Cr-4% Ni martensitic stainless steels. As a complement to this study, results of the fracture toughness J_{Ic} tests performed in the heat affected zone (HAZ) are added.

In this study, dimpled rupture occurred during tensile, fracture toughness J_{Ic}, and room temperature CVN tests. The inclusions play an important role during dimpled rupture, probably the most important one. Hence, a large portion of this chapter is focalized on the effects of inclusions on the mechanical properties. In addition, the formation of the austenite in both base and weld metals, especially in the case of the heat-treated weld metal, contributed to the improvement of the mechanical properties. This feature is also discussed in this chapter.

5.1 Microstructure

The microstructures and the austenite contents of the tested materials are shown in Figure 5-1 and Table 5-1, respectively. The microstructure of all the steels consisted of lath martensite (Figure 5-1), and austenite (Table 5-1). The base metals contain similar austenite percentages, whereas that of 410NiMo-HT is four times as high as the austenite content of 410NiMo-AW. The austenite content was not only increased significantly by the heat treatment process, but also its distribution is more homogeneous in the heat-treated weld metal. On the other hand, the austenite contents of the base metals were at least eight and two times as high as those of the weld metals in as-welded and heat-treated conditions, respectively.

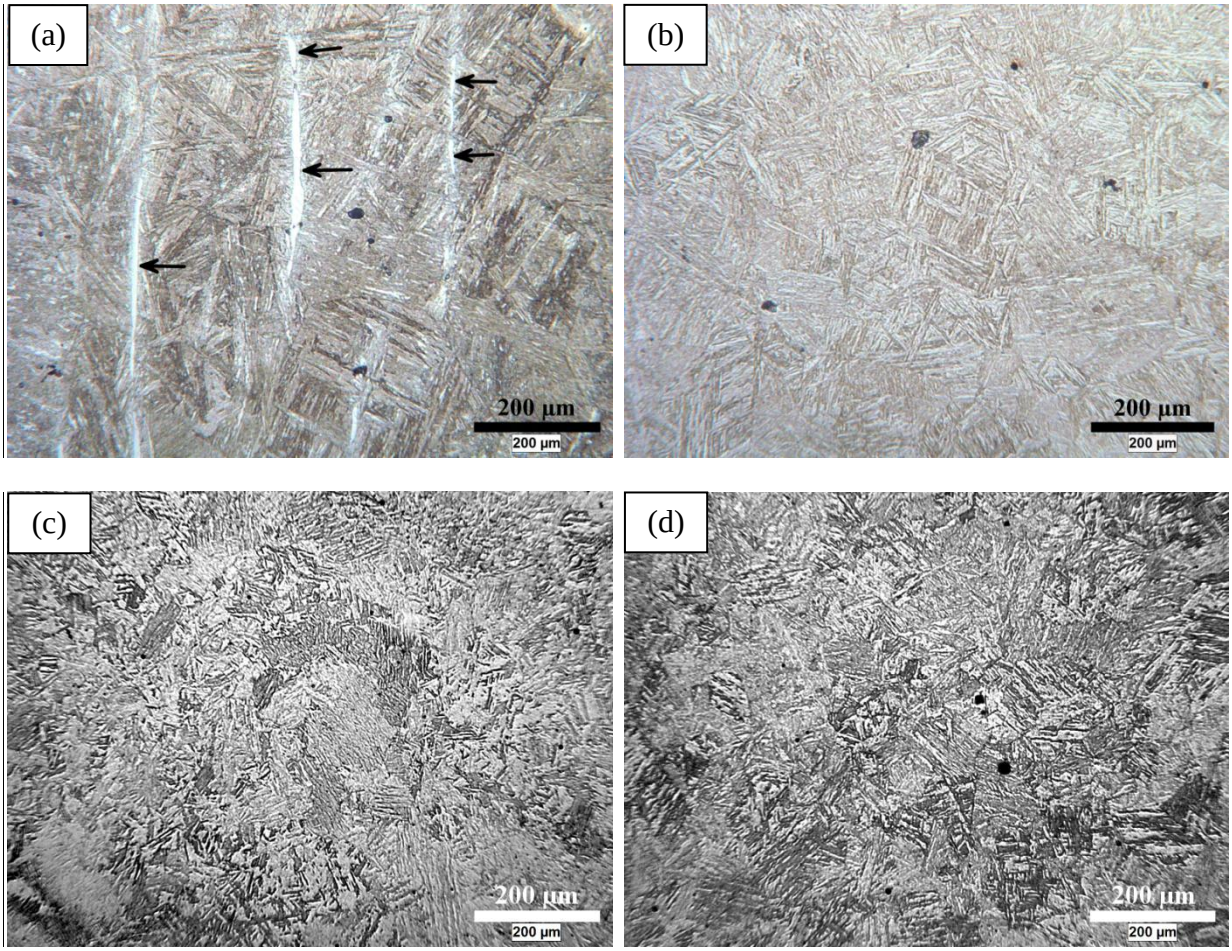

Figure 5-1: Microstructures of the tested materials: (a) CA6NM steel, (b) 415 steel, (c) 410NiMo-AW, and (d) 410NiMo-HT. The traces of delta ferrite shown by the arrows in (a)

Table 5-1: Austenite contents of the tested materials

Material	Austenite (%)
CA6NM steel	19.1 ± 6.4
415 steel	19.5 ± 2.2
410NiMo-AW	2.4 ± 1.0
410NiMo-HT	10.0 ± 0.6

As shown in Figure 5-1, the microstructure of 415 steel can be considered as a delta ferrite free one. Delta ferrite was observed in CA6NM steel and in the weld metals microstructures. As provided in Table 5-2, the differences in inclusion characteristics between the base metals and the weld metal are highly significant. The surface density of inclusions in the weld metal was at least about 800 times as much as that of the base metals, and the inclusion volume fraction was at least five times higher. The inclusion size and the inclusion spacing were at least more than nine and

19 times smaller in the case of the weld metal, respectively. On the other hand, the inclusion surface density of the CA6NM steel is about 35% higher than that of the 415 steel, and its volume fraction is about 2.5 times higher. Inclusions are about 40% larger in the CA6NM steel as compared to those in the 415 steel, and their spacing is approximately the same for both materials.

Table 5-2: Inclusion characteristics of the tested materials

Designation	Surface density (No./cm^2)	Volume fraction (%)	Size (Mean diameter, μm)	λ (μm)
CA6NM steel	1620 ± 368	0.22 ± 0.12	9.98 ± 8.62	37.07 ± 5.73
415 steel	1210 ± 242	0.09 ± 0.02	7.18 ± 6.42	36.05 ± 3.68
410NiMo	(1.29 ± 0.25) × 10^6	1.10 ± 0.14	0.76 ± 0.02	1.89 ± 0.10

5.2 Mechanical properties

5.2.1 Tensile tests

Tensile curves as well as tensile properties of the materials tested in this study are shown in Figure 5-2 and Table 5-3, respectively. As can be clearly observed, the weld metals have higher strength but lower ductility than the base metals. The weld metal in as-welded condition is the most resistant, but the least ductile material. However, its ductility was significantly improved by the heat treatment process keeping high values of yield and tensile strengths. On the other hand, the CA6NM steel is the least resistant material, but it has a relatively good ductility. The most ductile material is 415 steel. Its uniform elongation could be considered as equal as that of the CA6NM steel, but it is more than two times as much as that of 410NiMo-AW, and about 37% more than that of 410NiMo-HT.

As can be seen in Figure 5-2, the area under the stress-strain curves is approximately equal between CA6NM steel and 410NiMo-HT. However, the fracture toughness J_{Ic} of CA6NM steel is more than five times higher than that of 410NiMo-HT. It shows that the qualitative definition of fracture toughness which is based on the area under stress-strain curve of the tensile test is not valid for all materials. Separate plane strain fracture toughness K_{Ic} or J_{Ic} test should be performed to have a real idea about the toughness of a material.

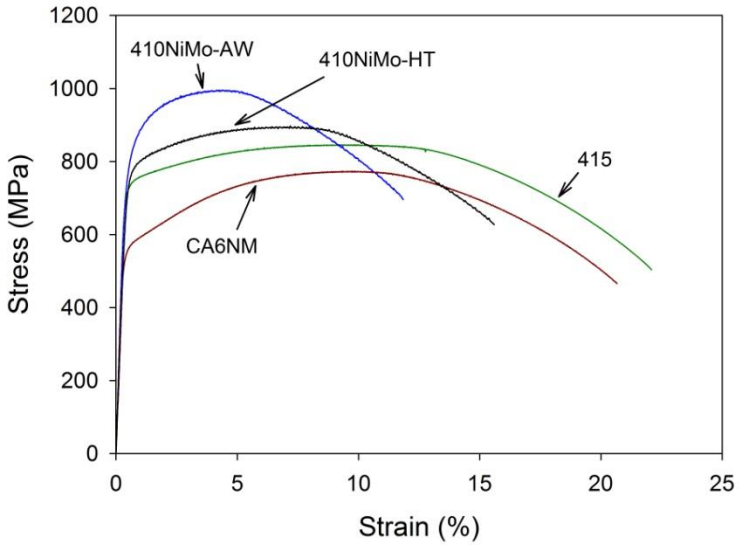

Figure 5-2: Tensile curves of the tested materials

Table 5-3: Tensile properties of the tested materials

Designation	σ_y (MPa)	σ_{UTS} (MPa)	e_u (%)	e_f (%)
CA6NM steel	575 ± 13.2	769 ± 7.4	9.5 ± 0.4	19.4 ± 1.7
415 steel	725 ± 0	843 ± 3.7	9.3 ± 0.4	21.7 ± 1
410NiMo-AW	783 ± 5.8	1007 ± 10.3	4.4 ± 0.1	10.5 ± 1.2
410NiMo-HT	765 ± 5	895 ± 4	6.8 ± 0.3	15.2 ± 0.4

5.2.2 Fracture toughness J_{Ic} tests

The J-R curves and plane strain fracture toughness properties of the base metals and the weld metals are shown in Figure 5-3 and Table 5-4, respectively. A comparison of the shapes of the J-R curves between the base metals and the weld metals shows that their crack propagation behaviors are different. As the J_{Ic} crack advances, the stress triaxiality at the crack tip decreases, and J increases by increasing Δa until the final data point is obtained for both steels. However, as compared to the base metals, it can be said that J increases by increasing Δa at the early stages of the test, but the curves reach a quasi-plateau for higher crack growths for the weld metals. This is because the stability of the J_{Ic}-crack extension is much less in the weld metals, and it can be explained by the very low tearing modulus of the weld metals (Table 5-4).

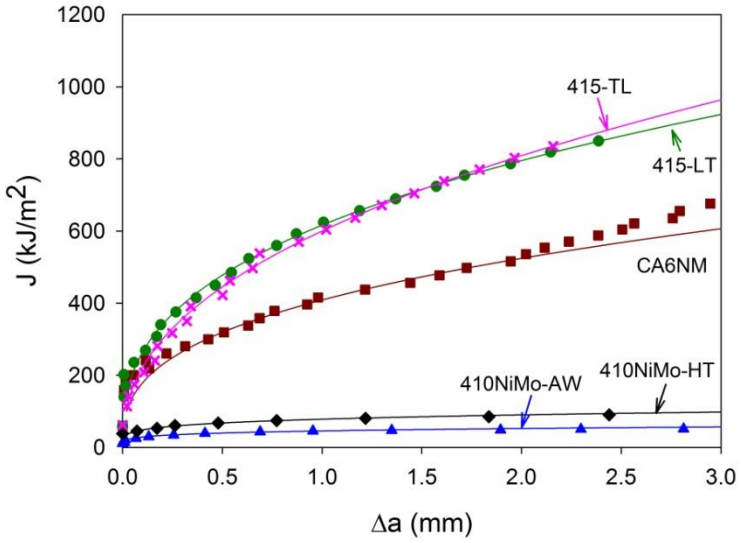

Figure 5-3: J-R curves of the base metals and weld metals

Table 5-4: Plane strain fracture toughness properties of the tested materials

Designation	J_{Ic} (kJ/m^2)	dJ/da (MPa)	T	K_{Ic} (MPa$\sqrt{m}$)
CA6NM steel	299 ± 13	153 ± 2	92 ± 1	256 ± 6
415 steel (LT)	416 ± 71	221 ± 4	84 ± 1	302 ± 25
415 steel (TL)	437	249	100	310
410NiMo-AW	31 ± 4	14.5 ± 2	5 ± 0.7	82 ± 5
410NiMo-HT	59 ± 0	21.6 ± 0.9	7 ± 0.3	114 ± 0

As mentioned in the section 1.3.3, the tearing modulus values were calculated using the following equation:

$$T = \frac{E}{\sigma_y^2}\frac{dJ}{da} \tag{5-1}$$

The slopes of the J-R curves (dJ/da) were calculated using the parts of the curves located between the exclusion lines. As provided in Table 5-4, slope of the J-R curve of 415 steel (LT) is 44% higher than that of CA6NM steel. Inversely, despite of higher fracture toughness of 415 steel (LT), tearing modulus of CA6NM steel is 9% higher. However, fracture toughness J_{Ic}, slope of the resistance curve, and tearing modulus of 415 steel (TL) were higher than those of both CA6NM steel and 415 steel (LT).

On the other hand, both slopes of the J-R curve and tearing modulus of the heat-treated weld metal were higher than those of the as-welded material (57% and 40%, respectively). Therefore,

the crack propagation resistance of the weld metal was considerably improved by the heat treatment process. This could be because of its higher austenite content which has led to a stronger TRIP effect closing the crack front [89], and its softer microstructure (tempered martensite as compared to fresh martensite).

In most cases, higher tearing modulus values resulted from higher slopes of the resistance curves (Table 5-4). One exception to this observation is the tearing modulus of 415 steel (LT) that is lower than that of CA6NM steel. This is because dJ/da of 415 steel (LT) is not high enough to compensate the effect of its high yield strength since tearing modulus is inversely proportional to the square of the yield strength (equation (5-1)).

The tearing modulus of the base metals was at least about 12 times as high as that of the weld metals; however, this proportion reduced to 5 if the fracture toughness J_{Ic} is compared. Therefore, as compared to the base metals, the crack initiation starts not only at much lower J values, but its propagation is also drastically faster in the weld metals.

5.2.3 CVN tests

CVN ductile-brittle transition curves as well as DBTT (Ductile-Brittle Transition Temperature) and fracture energies of the tested materials are shown in Figure 5-4 and Table 5-5, respectively. DBTT was defined as the temperature corresponding to the average of fracture energies absorbed at upper shelf and lower shelf of each material. As can be seen in Figure 5-4, 415 steel and 410NiMo-AW have the highest and the lowest rates of transition from ductile to brittle fracture, respectively.

As provided in Table 5-5, 415 steel has the highest, and 410NiMo-HT has the lowest DBTT. Room temperature fracture energies of the base metals are at least about three times more than those of the weld metals. On the other hand, 415 steel and 410NiMo-HT absorbed 49% and 56% more energies than CA6NM steel and 410NiMo-AW, respectively. For the weld metals, heat treatment has resulted to improvement of DBTT, and CVN fracture energies from 80 °C to about -150 °C.

As shown in Figure 5-4, the curves merged together at low temperatures i.e., from about -60 °C to -190 °C for the base metals. In the contrary, the as-welded and the heat-treated weld metals absorbed different energies from 80 °C to -150 °C. This is because the base metals have equal

austenite contents (Table 5-1), and cleavage becomes dominant at low temperatures. However, higher austenite content as well as the softer matrix (tempered martensite) of the heat-treated weld metal resulted in higher fracture energies even though cleavage was also dominant at low temperatures in the weld metals. All the fracture energies could be considered as equal at -190 °C for the tested materials. This is because rupture occurred by pure cleavage, and different microstructural features didn't affect it.

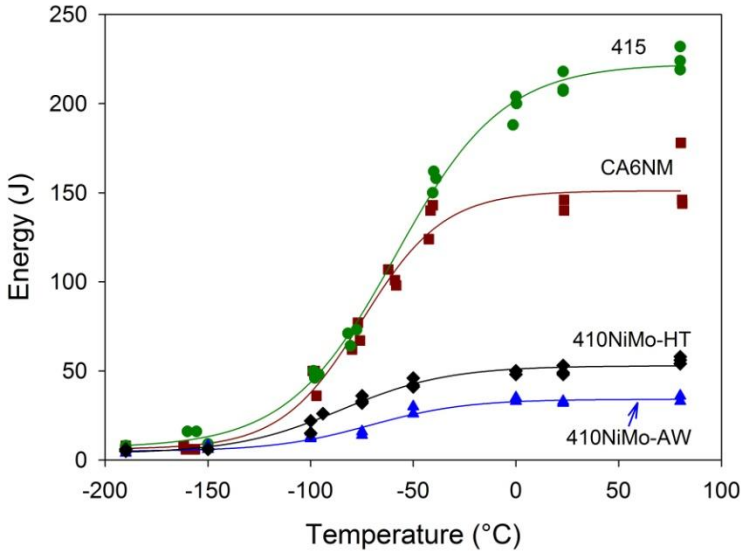

Figure 5-4: Charpy transition – temperature curves of the tested materials

Table 5-5: DBTT and CVN fracture energies of the tested materials

Designation	DBTT (°C)	CVN at room temperature (J)
CA6NM steel	-75	142 ± 3.5
415 steel	-59	211 ± 6.1
410NiMo-AW	-71	32 ± 0.6
410NiMo-HT	-85	50 ± 2.6

5.3 Fractography

5.3.1 Tensile, J_{Ic}, and CVN tests of the base metals and the weld metals

In this study, fracture occurred by dimpled rupture for all the tests performed at room temperature. For each of the tested materials, very similar fracture appearances were observed for the tensile, J_{Ic}, and room temperature CVN tests in terms of inclusion size and dimples

nucleation. Therefore, to prevent repetition of the results and interpretations, only the J_{Ic} fracture surfaces were chosen to be discussed in this section. The same interpretations can be presented for the tensile and room temperature CVN fracture mechanisms.

SEM micrographs of J_{Ic} fracture surfaces of the tested materials are shown in Figure 5-5. All of the fracture surfaces show dimpled rupture, but differences in terms of the dimple size, the inclusion size, and the existence of intact/broken inclusions are observed. A comparison between micrographs (a) and (b) shows that large dimples as well as very fine ones existed on CA6NM steel J_{Ic} fracture surface (micrograph (a)), but the size of dimples seems to be much more uniform in the case of 415 steel (micrograph (b)). On the contrary, no significant differences are observed between the J_{Ic} fracture surfaces of the weld metals (micrographs (c) and (d)), and the majority of the inclusions and their resulted dimples are more or less of the same size.

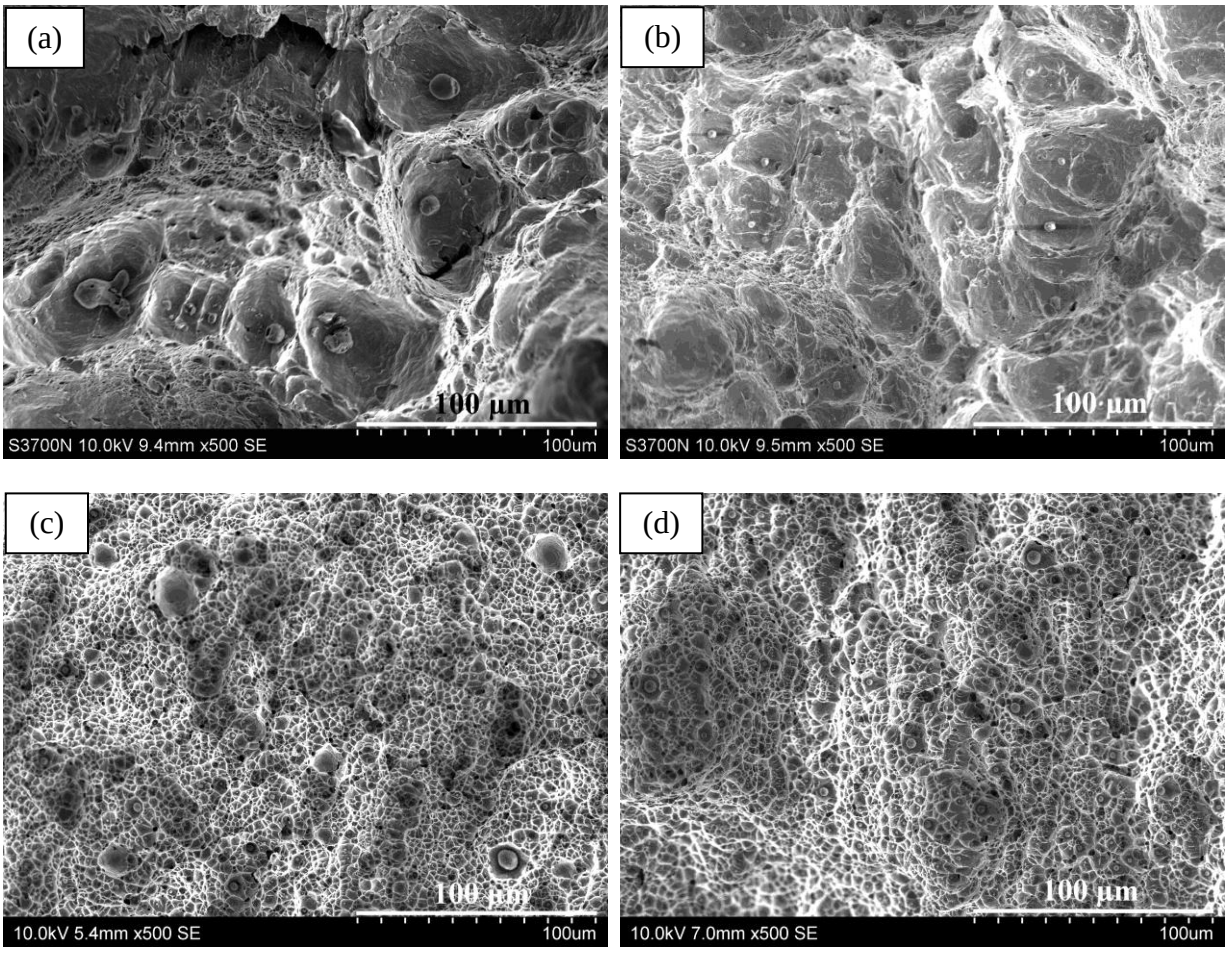

Figure 5-5: J_{Ic} fracture surfaces of the tested materials: (a) CA6NM steel, (b) 415 steel, (c) 410NiMo-AW and, (d) 410NiMo-HT

Table 5-6: Inclusion sizes measured on J_{Ic} fracture surfaces of the tested materials

Material	Number of measured inclusions	Size (Mean diameter, µm)
CA6NM steel	40	12.7 ± 6.7
415 steel	46	3.9 ± 2.7
410NiMo-AW	35	0.8 ± 0.3
410NiMo-HT	35	0.9 ± 0.4

However, large differences existed between the base metals and the weld metals fracture surfaces: inclusions and dimples are very finer and much more numerous in the case of the weld metals. As provided in Table 5-6, the largest inclusions were observed on the J_{Ic} fracture surfaces of CA6NM steel. The second largest inclusion size was observed on 415 steel J_{Ic} fracture surfaces, and finally, the finest inclusions were found on the weld metals J_{Ic} fracture surfaces for both as-welded and heat-treated conditions. In addition, a large number of inclusions were broken on CA6NM steel J_{Ic} fracture surfaces, whereas all inclusions observed on 415 steel and the majority of the ones detected on the weld metals (in both as-welded and heat-treated conditions) J_{Ic} fracture surfaces were found to be intact.

As provided in Table 5-2, the surface density of inclusions was at least 800 times higher in the weld metals. The very large number of inclusions resulted to a much lower inclusion spacing of less than 2 µm. As a result, much more dimples very closely spaced were formed in the weld metals, as shown in Figures 5-5 (c) and (d). Accordingly, it can be concluded that micro-voids nucleation sites are so numerous in the weld metals that the growth of dimples is limited by their coalescence. That is, the coalescence stage occurred without significant void growth for both as welded and heat-treated weld metals. It can also be said that the majority of inclusions have approximately the same chance for micro-voids nucleation in the weld metals since the inclusion size measured on metallographic sections (Table 5-2) is very close to those measured on fracture surfaces (Table 5-6).

Inversely, the inclusion sizes measured on metallographic sections are different from those measured on the fracture surfaces of the base metals (Table 5-2 vs. Table 5-6). This is because micro-voids nucleated from inclusions larger than 10 µm in diameter are much more numerous for CA6NM steel resulting to the larger inclusion size of the fracture surfaces. It shows that the inclusion size play an important role in the case of CA6NM steel. On the contrary, inclusions smaller than 10 µm in diameter are much more numerous on 415 steel fracture surfaces

indicating that this is the local frequency of inclusions which control the fracture mechanism in 415 steel, and the frequency of inclusions smaller than 10 μm in diameter is more numerous on fracture surfaces than on a random surface in the material. That is why the inclusion size measured on the fracture surfaces is smaller than that measured on the metallographic section.

Additionally, it seems that rupture of inclusions also play also a role in ductile rupture of this steel as many ruptured inclusions were observed on the fracture surfaces of CA6NM steel facilitating the micro-void formation. No ruptured inclusion was observed on 415 steel fracture surfaces, and micro-voids were formed as a result of matrix-inclusion decohesion. On the other hand, nearly all of inclusions observed on fracture surfaces of the weld metals, for both as-welded and heat-treated conditions, were intact (not broken).

Finally, the high frequency of inclusions smaller than 10 μm in diameter, as well as having more resistant inclusions improved ductility, fracture toughness J_{Ic}, and CVN fracture energy of 415 steel. The key parameter that made decrease the ductility, fracture toughness J_{Ic}, and CVN fracture energy values of the weld metals was the very low inclusion spacing (about 2 μm) comparing with that of the base metals (about 40 μm). This is because micro-void nucleation occurs in very large numbers in the weld metals and rupture occurred before void growth could take place.

5.3.2 Inclusion types

Inclusion types detected in the materials tested in this study are summarized in Table 5-7. Si oxide, Mn oxide, Al oxide, and Cr oxide exist in the majority of inclusions of the base metals and the weld metal, but their proportions are different for each steel. Si-rich and Mn-rich inclusions were observed in CA6NM steel and in the weld metal, whereas Al-rich inclusions were only detected in 415 steel. However, Ti-rich and Zr-rich components were only detected in the weld metal. It has to be mentioned that all Si, Mn, Ti, Zr, and Cr components existed together in approximately all of the inclusions detected in the weld metal, and it is more appropriate to refer them as Si-Mn-Ti-Zr-Cr-rich inclusions to be recognized from Si/Mn-rich inclusions existing in CA6NM steel.

Table 5-7: Types of inclusions detected in the studied materials

Material	Inclusion type					
	Si-rich component	Mn-rich component	Al- rich component	Ti- rich component	Zr- rich component	Cr- rich component
CA6NM steel	✓	✓				
415 steel			✓			
410NiMo	✓	✓		✓	✓	✓

In addition, traces of non-melted chromium were detected in the weld metal (Figure 5-6). However, it has to be said that only these two small islets of non-melted chromium were detected all over the examined weld metal fracture surfaces. These islets could be related to the presence of non-melted Cr-rich particles as found in a previous study on 410NiMo cold cracking [90].

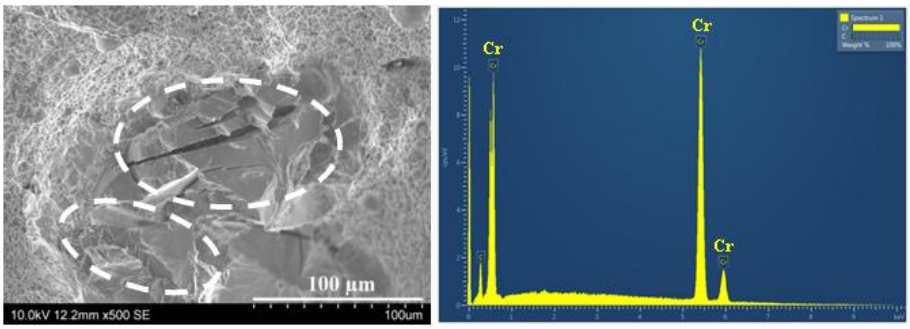

Figure 5-6: Traces of non-melted chromium on CVN fracture surface of the heat-treated weld metal

5.3.3 Quantitative estimation of the void growth

As given in the section 1.5.5, the following equations can be used to calculate the required deformation for the growth of an isolated spherical void in a perfectly plastic matrix:

$$\varepsilon_R = 2.342 \ln\left(\frac{R}{R_0}\right) \exp\left(-\frac{3}{2} S_T\right) \qquad \text{for} \quad S_T \geq 1 \tag{5-2}$$

and

$$\varepsilon_R = 2.342\, S_T^{(-1/4)} \ln\left(\frac{R}{R_0}\right) \exp\left(-\frac{3}{2} S_T\right) \qquad \text{for} \quad 1/3 \leq S_T \leq 1 \tag{5-3}$$

where R_0 is the initial, and R is the final radius of the void, and S_T is defined as the stress triaxiality.

The calculated ε_R for the tested materials during tensile testing is provided in Table 5-8. Half of the inclusion size measured on the fracture surfaces was used as the R_0 for each material, and half of the inclusion spacing calculated from metallographic sections was used as R. The calculated inclusion spacing on the metallographic sections gives a good estimation of the average of the final size of dimples on the fracture surfaces. Since metallurgical parameters such as the hardness of martensite and the content of austenite were not considered in this model, the same ε_R is obtained in the case of the weld metal for both as-welded and heat-treated conditions.

Table 5-8: Equivalent strain calculated for tensile samples

Material	R_0 (μm)	R (μm)	S_T	ε_R
CA6NM	6.23	18.53	0.33	2.04
415	1.80	18.02	0.33	4.31
410NiMo	0.43	0.94	0.33	1.47

True strains at fracture obtained in tensile testing are provided in Table 5-9. As can be seen in this table, the true strains are lower than the estimated ε_R values (Table 5-8). Similar to the calculated ε_R values, 415 steel has the largest ε value, and the weld metals have the smallest ε value.

Table 5-9: True strains obtained in tensile testing of the tested materials

Material	True strain (ε)
CA6NM	0.99
415	1.22
410NiMo-AW	0.64
410NiMo-HT	0.75

5.4 K_{Ic}-CVN correlation

As mentioned in section 1.6, there is a practical interest to predict fracture toughness K_{Ic} using CVN fracture energy, and up to now, K_{Ic}-CVN correlations were developed for different grades of steels having different ranges of yield strength and CVN fracture energy. In this section, in order to propose the most precise K_{Ic}-CVN correlation for both the base metals and weld metals of 13% Cr-4% Ni martensitic stainless steels, the existing correlations are evaluated and new correlations will be developed.

The yield strength, uniform elongation, fracture toughness K_{Ic}, and CVN fracture energies of the tested materials are provided in Table 5-10. The CA6NM-A and CA6NM-B steels were

fabricated in two different commercial foundries. The mechanical characterization of these steels was performed in order to obtain a more precise correlation.

Chemical compositions, as well as austenite content and prior austenite mean grain size of CA6NM-A and CA6NM-B are provided in Table 5-11 and Table 5-12, respectively. For comparison purposes, CA6NM data was added to the tables. As provided in Table 5-10, the dispersion of the results is not significant for the uniform elongation, fracture toughness K_{Ic}, and CVN fracture energy in the cases of CA6NM, CA6NM-A, and CA6NM-B steels. However, some differences are observed for the yield strengths. This could be due to the carbon content, austenite

Table 5-10: Room temperature tensile strength, uniform elongation, fracture toughness K_{Ic}, and CVN fracture energy of the tested materials

Designation	σ_y (MPa)	e_u (%)	K_{Ic} (MPa$\sqrt{m}$)	CVN (J)
CA6NM steel	575 ± 13	9.5 ± 0.4	256 ± 6	142 ± 3.5
CA6NM-A steel	613 ± 5.8	9.6 ± 0.6	265 ± 32	172 ± 10.8
CA6NM-B steel	745 ± 0	8.6 ± 1.1	242 ± 8.1 [81]	162 ± 5.6
415 steel (LT)	725 ± 0	9.3 ± 0.4	302 ± 25	211 ± 6.1
Weld metal-AW	783 ± 5.8	4.4 ± 0.1	82 ± 5	32 ± 0.6
Weld metal-HT	765 ± 5	6.8 ± 0.3	114 ± 0	50 ± 2.6

Table 5-11: Chemical compositions of CA6NM-A and CA6NM-B

Designation	C	Mn	P	S	Si	Cr	Ni	Mo
CA6NM steel	0.016	0.50	0.019	0.007	0.26	12.79	3.49	0.55
CA6NM-A [19]	0.013	0.61	0.026	0.002	0.65	13.1	4.3	0.51
CA6NM-B [19]	0.020	0.58	0.026	0.0025	0.41	13.6	4.1	0.61

Table 5-12: Austenite content and prior austenite mean grain size of CA6NM-A and CA6NM-B

Designation	Austenite (%)	Prior austenite mean grain size (µm)
CA6NM steel	19.1	163
CA6NM-A [19]	17.1	77
CA6NM-B [19]	11.6	93

content, and prior austenite grain size. The CA6NM steel which has the lowest yield strength indeed has the highest austenite content and the largest prior austenite grain size.

In a similar way to that of the correlation of Rolfe and Novak [69], $(K_{Ic}/\sigma_y)^2$ was plotted versus (CVN/σ_y) in Figure 5-7. As can be seen in this figure, a power low relationship does exist between these normalized fracture toughness K_{Ic} and CVN absorbed energies:

$$\left(\frac{K_{Ic}}{\sigma_y}\right)^2 = 0.90\left(\frac{CVN}{\sigma_y}\right)^{1.27} \tag{5-4}$$

This relation can be rearranged in order to predict the fracture toughness directly as follows:

$$K_{Ic} = 0.95\frac{(CVN)^{0.63}}{(\sigma_y)^{-0.37}} \tag{5-5}$$

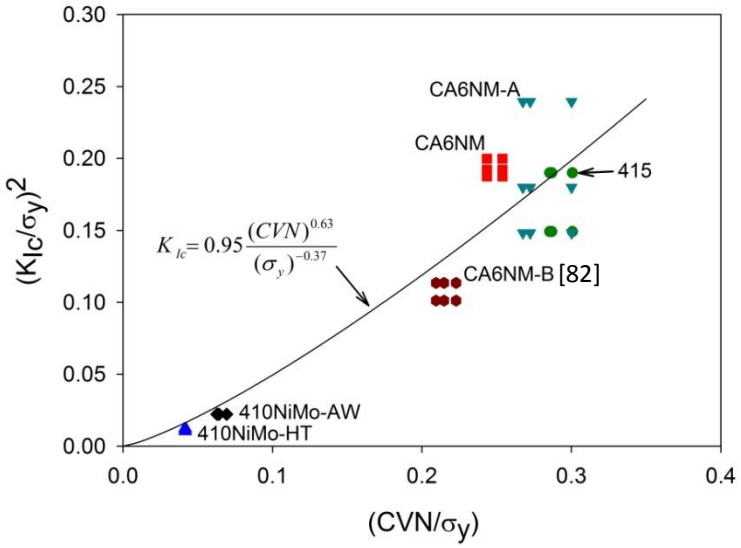

Figure 5-7: Relationship between normalized fracture toughness K_{Ic} and CVN absorbed energies

In addition, the K_{Ic} values were plotted versus CVN room temperature fracture energies in Figure 5-8. As can be seen in this figure, an empirical power law K_{Ic}-CVN correlation was obtained simply by developing a non-linear regression curve of the data points:

$$K_{Ic} = 9.22(CVN)^{0.65} \tag{5-6}$$

Now, in order to evaluate the different correlations proposed in the literature, a preliminary analysis was made using the results obtained on the base metal CA6NM-B (preliminary J_{Ic} testing, section 2.2.2). The measured K_{Ic} values were compared with the predictions made by the different correlation functions proposed in the literature.

The comparison between these predicted values and the measured K_{Ic} ones is provided in Table 5-13. The measured K_{Ic} value was taken from [81] as being 242 MPa√m. Its yield strength, uniform elongation, and room temperature CVN fracture energy were 745 MPa, 8.6%, and 162 J, respectively, measured in this study. The yield strength of CA6NM-B was not in the range of those provided in Table 1-2. Therefore, large differences between the measured K_{Ic} values and predicted ones (Table 5-13) were expected.

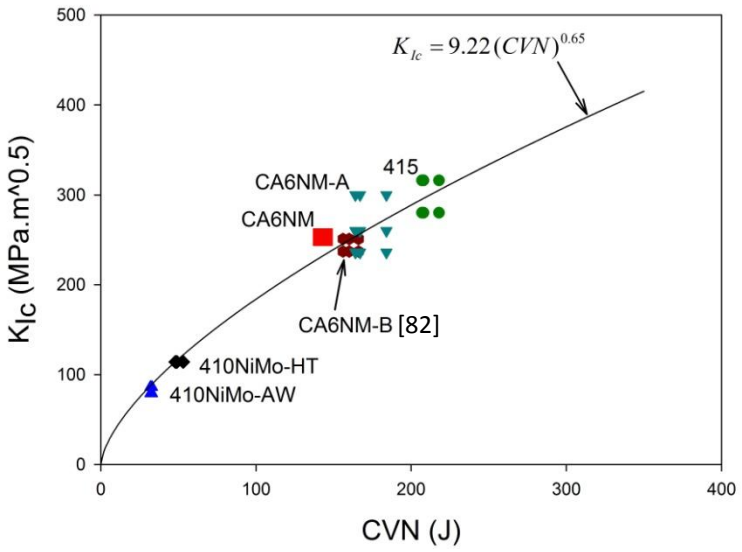

Figure 5-8: K_{Ic}-CVN correlation obtained from non-linear regression curve of the data points

However, as can be seen in Table 5-13, the correlation of Ault-Wald-Bertolo gives an error of 40%, the correlation of Turby-Ferguson, and that proposed in British standard (Table 5-13) give very large errors. This is because these correlations are not developed for the same yield strength and CVN fracture energy limit ranges as those of CA6NM-B (see Table 1-2). On the other hand, the correlation of Rolfe-Novak gives a much lower error of 12% for the predicted K_{Ic} value. This could be because the yield strength and CVN fracture energy of CA6NM-B can be used for this correlation as shown respectively by Begley and Toolin [70], and Iwadate et al. [71].

The most precise predicted K_{Ic} value was obtained from Schindler's correlation by an error of just 2%. The predicted K_{Ic} obtained by Wallin's correlation, had an error of 7%. Please note that Schindler and Wallin correlations were not developed for special ranges of yield strength. Schindler's correlation was developed using an analytical approach and Wallin tested 112 materials using curve fitting to develop his correlation. Therefore, Schindler's correlation could

be used theoretically for all steel categories of any yield strength range, but unfortunately Wallin et al. didn't mention which kind of material/yield strength range could be used (see section 1.6).

Table 5-13: Comparison between predicted K_{Ic} values of a cast 13% Cr-4% Ni martensitic stainless steel and that of 242 MPa√m measured in [81]

Author	Predicted K_{Ic} (MPa√m)	Relative difference between measured and predicted K_{Ic} (%)
Rolfe-Novak [69]	271	+12
Ault-Wald-Bertolo [72]	145	-40
Thorby-Ferguson [73]	22	-91
Schindler [74]	248	+2
Wallin et al. [66]	258	+7
British Standard [76]	142	-41

To illustrate and evaluate the correlation predicting the most precise fracture toughness K_{Ic} of the materials tested in this study, plots of the measured K_{Ic} values vs. predicted ones were traced (see Figure 5-9). Note that correlations of Rolfe-Novak, Schindler, and Wallin, as well as correlations (5-5) and (5-6), were only considered. The correlations of Rolfe-Novak, Schindler, and Wallin, presented in the section 1.6, are respectively:

$$K_{Ic} = \sqrt{0.64(CVN)\sigma_y - 0.0064\sigma_y^2} \qquad \text{Rolfe-Novak [69]} \qquad (5\text{-}7)$$

$$K_{Ic} = \sqrt{\frac{3.92 e_u^{1/3} (CVN) E}{(1-\nu^2)}} \qquad \text{Schindler [74]} \qquad (5\text{-}8)$$

$$K_{Ic} = \sqrt{0.53 E (CVN^{1.38}) 0.2^m} \qquad \text{Wallin [75]} \qquad (5\text{-}9)$$

$$m = 0.133(CVN^{0.256}) - \frac{\sigma_y}{4664} + 0.03$$

As shown in Figures 5-9 (a) to (e), the fracture toughness K_{Ic} values predicted by the correlation of Rolfe-Novak [69], the Wallin's correlation [66], correlation (5-5), Shindler's correlation [74], and correlation (5-6) were compared with the measured ones, respectively. The predicted K_{Ic} values are in good agreements with measured ones for all five correlations. Figures 5-9 (a) to (e) are ordered from the least precise correlation (correlation of Rolfe-Novak) to the most precise

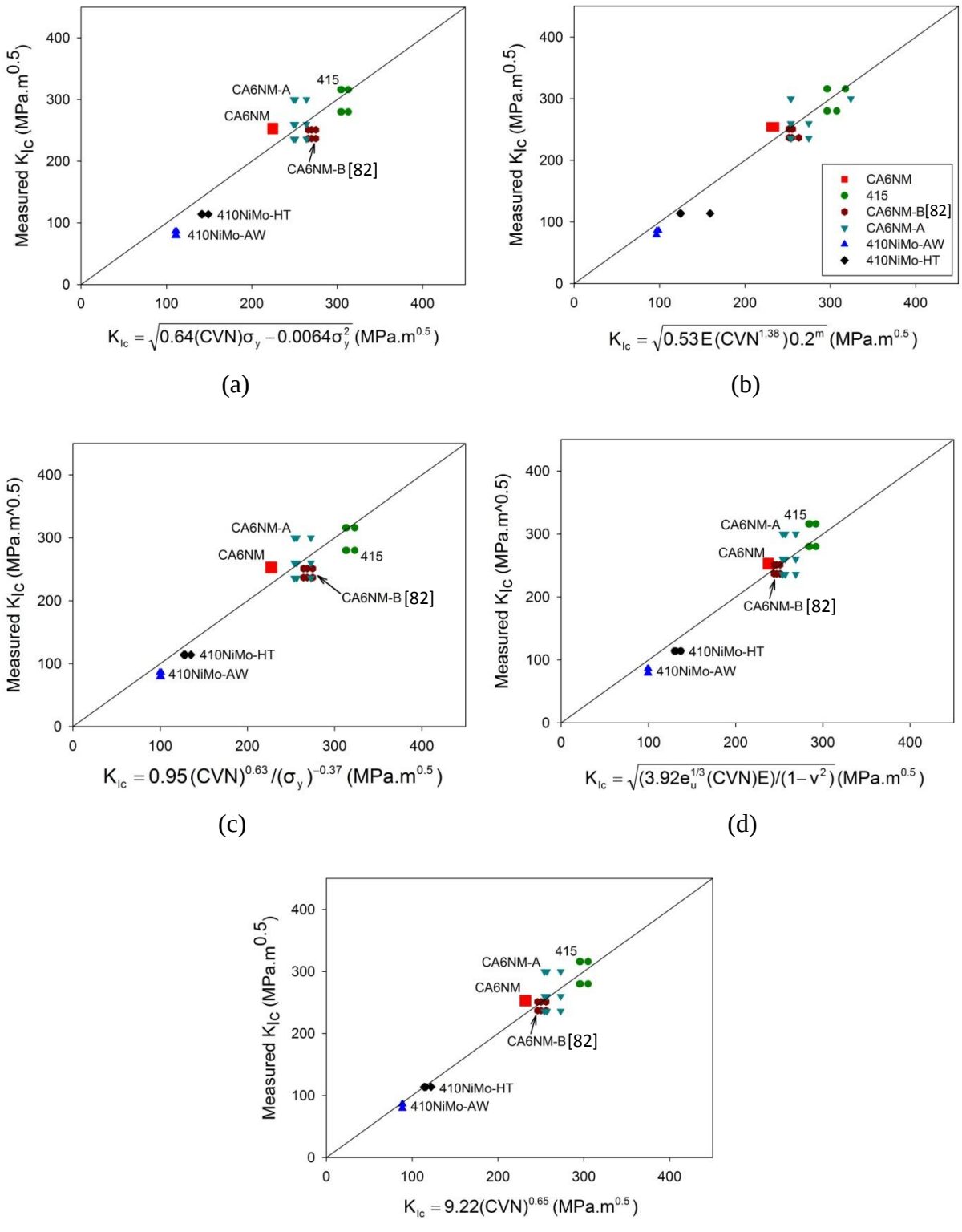

Figure 5-9: Measured K_{Ic} values versus predicted ones using (a) correlation of Rolfe-Novak, (b) Wallin's correlation, (c) correlation (5-5), (d) Schindler's correlation, and (e) correlation (5-6)

one (correlation (5-6)), using R^2 (coefficient of determination) [91] and Chi square (χ^2) goodness of fit [92]. Note that correlation (5-6) covers wide ranges of CVN fracture energies and fracture toughness K_{Ic} of 32-218 J and 79-316 MPa$\sqrt{m}$, respectively.

5.5 Additional results in the HAZ

The fracture behaviors of the base and weld metals of 13% Cr-4% Ni martensitic stainless steels were respectively studied in the chapters 3 and 4. However, in the case of a welded joint, the microstructure of the HAZ is more complex than those of the base and weld metals as it is subjected to very high temperatures during welding (see section 1.2.1). Therefore, it is interesting to shed light on the fracture behavior of a welded joint in the presence of a very sharp crack produced by fatigue cycling. In this section, the fracture behavior of the 13% Cr-4% Ni martensitic stainless steels welded joints is studied for both as-welded and heat-treated conditions. For this purpose, fracture toughness J_{Ic} tests were performed in the HAZ using CT samples with the crack starter notch located along the fusion line, and one millimetre in the HAZ.

5.5.1 Fracture toughness J_{Ic} tests performed in the HAZ

Ruptured J_{Ic} sample of the first test, crack starter notch located along the fusion line, is shown in Figure 5-10. As shown in (a), crack deviation starts as soon as the fatigue crack gets out of the starter notch reaching at a distance of 2 mm from the fusion line at the end of the fatigue pre-cracking process. Hence, the J_{Ic} test was performed in a distance of 2 mm from the fusion line in the HAZ. As can be seen in this figure, the crack also continued to deviate during J_{Ic}-test crack extension. After the J_{Ic}-test, fatigue cycling was performed to mark the crack front. As can be seen in (b) and (c), the fatigue crack has propagated from the edges of the J_{Ic} crack front and the J_{Ic} crack was only extended at the center of the specimen. This is because triaxial stress state condition exists only at the center (the edges of the sample were in the plane stress condition since side-grooves were not machined).

Obviously, this test has to be rejected as per ASTM E1820, since the J_{Ic} crack front was not straight. Therefore, side-groves were machined for further tests to prevent crack deviation, and plane stress condition on the edges. The crack starter notch was machined at a distance of 1 mm from fusion line in the base metal.

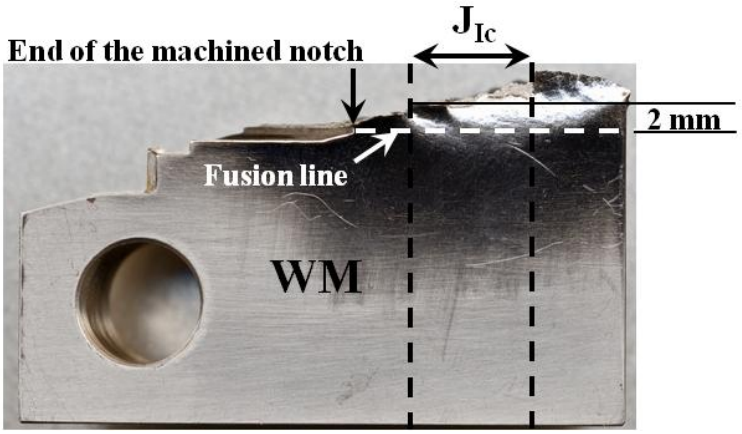

(a)

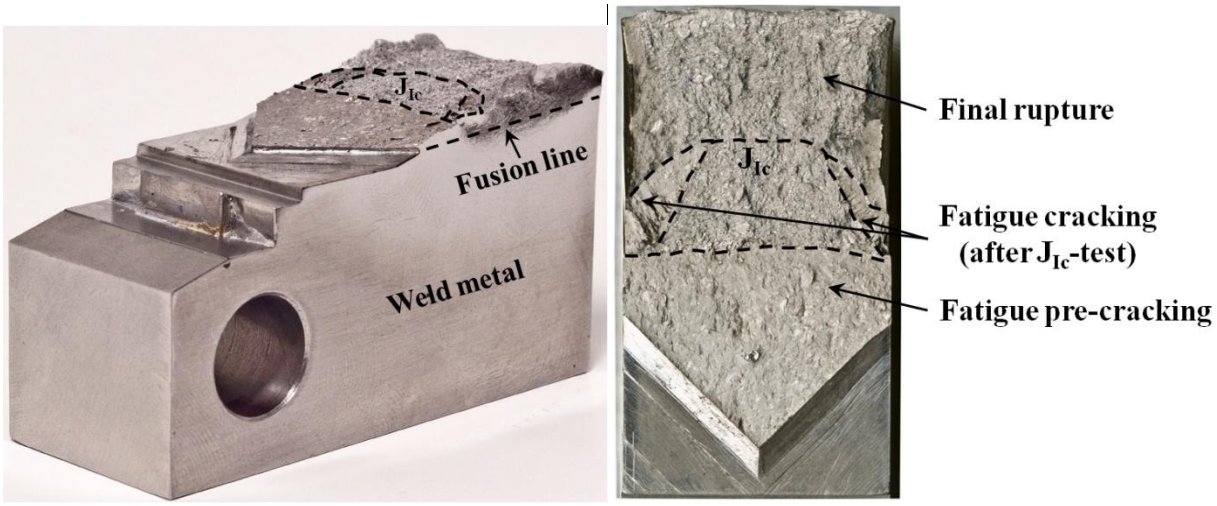

(b) (c)

Figure 5-10: Fractured J_{Ic} sample, crack starter notch located along fusion plane, (a) side view, (b) overview, and (c) top view

J-Δa plots of fracture toughness J_{Ic} performed in the HAZ, in both as-welded and heat-treated conditions, are shown in Figure 5-11. Except the first and the third tests performed in the as-welded condition (HAZ-AW-1 and HAZ-AW-3, respectively), complete J-R curves could not be developed for the other tests since not enough data points were obtained. This is due to the crack path deviation. Just after a short stable propagation smaller than one millimeter, the crack propagates along the fusion line in an unstable manner. The ASTM E1820 crack straightness requirements were not satisfied for any of these tests, and candidate values of fracture toughness, K_Q, were only determined.

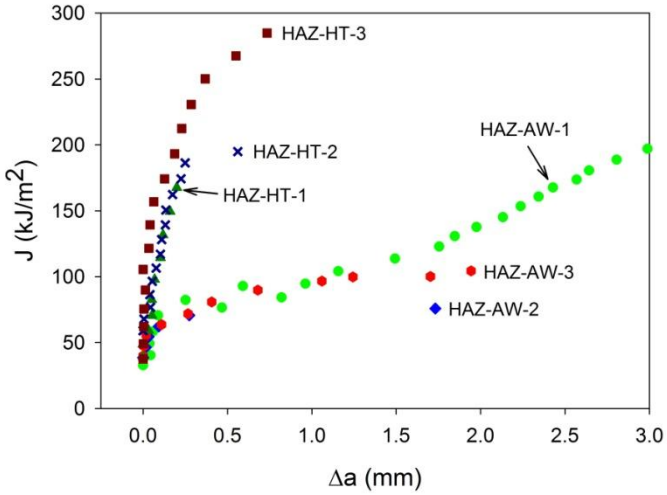

Figure 5-11: J-Δa plots of fracture toughness J_{Ic} tests performed in the HAZ in as-welded and heat-treated conditions. HAZ-AW-1 was performed at 2 mm from fusion line

Fracture toughness J_Q and the equivalent K_Q values of the tests performed in the HAZ in the as-welded and the heat-treated conditions are provided in Table 5-14. J_Q values measured in the heat-treated condition are at least 2 times as high as those measured in the as-welded condition.

Table 5-14: Fracture toughness J_Q and the equivalent K_Q values of the tests performed in the HAZ, 1 mm far from the fusion line, in the as-welded and the heat-treated conditions

HAZ-AW	J_Q (kJ/m^2)	K_Q (MPa√m)	HAZ-HT	J_Q (kJ/m^2)	K_Q (MPa√m)
HAZ-AW-1*	82	134	HAZ-HT-1	168	192
HAZ-AW-2	71	125	HAZ-HT-2	189	204
HAZ-AW-3	72	126	HAZ-HT-3	249	234
Mean	75 ± 6	128 ± 5	Mean	202 ± 42	210 ± 22

* This test was performed using a specimen without side grooves; J_{Ic} test started at 2 mm from fusion line.

J_{Ic} fracture surface of the HAZ-AW-3 specimen is shown in Figure 5-12. The J_{Ic} stable crack front was marked by fatigue cracking. As shown in Figure 5-11, enough data points were obtained to develop a complete J-Δa plot, but since ASTM E1820 crack straightness conditions were not satisfied, a candidate value of fracture toughness, K_Q, was only determinated. As can be seen in Figure 5-12, unstable crack propagation was not observed during the J_{Ic}-test, however, the specimen was broken from the fusion plane after tearing the specimen at the final stage of the

test. Different crack paths i.e., J_{Ic} stable crack and crack propagation along the fusion line are clearly observed in this figure.

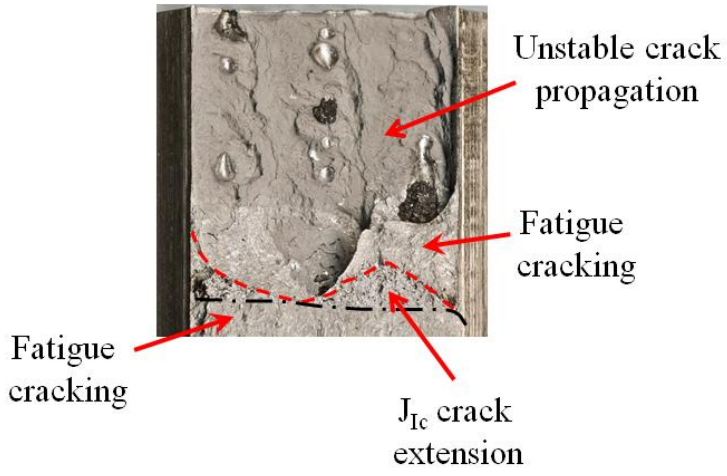

Figure 5-12: Fracture toughness J_{Ic} test fracture surface of the third test performed in the HAZ in as-welded condition (HAZ-AW-3 sample)

The J-R curves and fracture toughness properties of the tests carried out in the HAZ are respectively shown in Figure 5-13, and Table 5-15. Fracture toughness (J_Q), slope of the J-R curve, and tearing modulus of the tests performed in heat-treated condition were about 2.5 times as high as those performed in as-welded condition.

A simple comparison between Figure 5-13 and Figure 5-3, shows that the resistance curves of the tests performed in the HAZ are located between those of the base and weld metals. Fracture toughness (J_Q) obtained in the HAZ is at least 32% lower, and 27% higher than fracture toughness (J_{Ic}) of the base metals, and that of the weld metals, respectively. The tearing modulus was at least a quarter of that of the base metals, and at least 14% higher than that of the weld metals. The stable crack growth behaviors are very similar to those of the weld metals. It shows that even if sudden crack propagation does not occur along the fusion line (the case of HAZ-AW-3), larger crack growths (Δa) will occur in the HAZ as compared to those in the base metals.

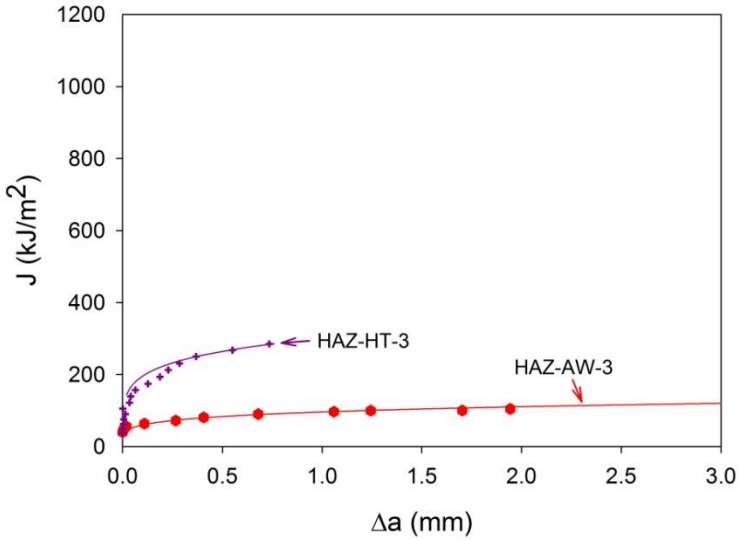

Figure 5-13: J-R curves of the tests performed in the HAZ

Table 5-15: Fracture toughness properties of the tests performed in the HAZ

Designation	J_Q(kJ/m^2)	dJ/da (MPa)	T	K_Q (MPa√m)
HAZ-AW	75 ± 6	19.0 ± 13.5	8 ± 6	128 ± 5
HAZ-HT	202 ± 42	46.2 ± 26.2	21 ± 12	210 ± 22

5.5.2 Fractography of the Fracture toughness J_{Ic} performed in the HAZ

5.5.2.1 J_{Ic} stable crack extension

Fracture surfaces of J_{Ic} stable crack extensions occurred at 2 mm and 1 mm far from the fusion line in as-welded condition are shown in Figures 5-14 (a) and (b), respectively. The fracture mode is semi-cleavage for both samples, and no significant differences are observed. That is why these two samples have similar fracture toughness J_Q (Table 5-14).

Figure 5-15 shows fracture surface of J_{Ic} test carried out at 1 mm far from fusion line in heat-treated condition. A totally dimpled rupture is observed. The fracture surface characteristics are similar to those of CA6NM steel dimpled ruptures as discussed in Chapter 4 in detail.

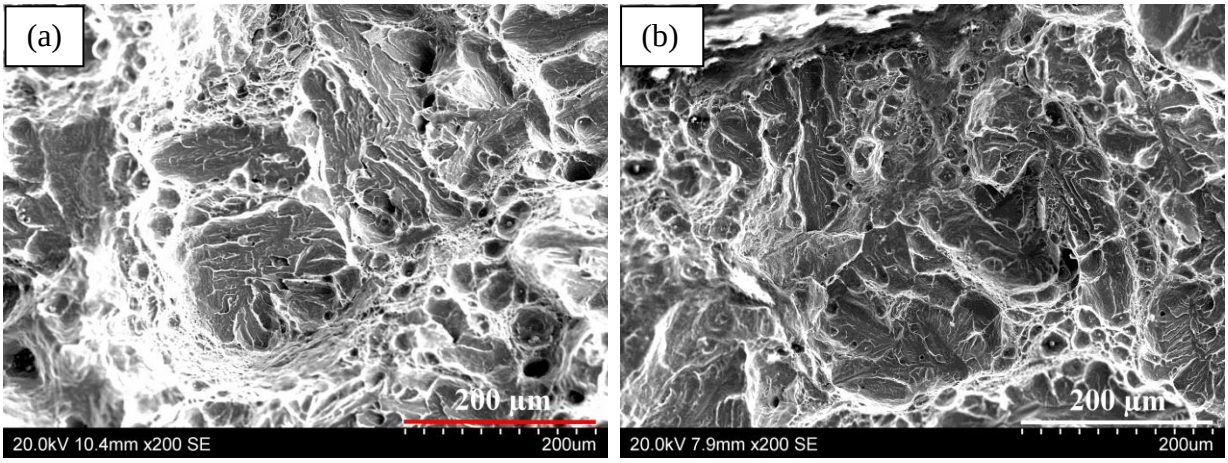

Figure 5-14: SEM micrographs of J_{Ic} stable crack extensions occurred at (a) 2 mm and (b) 1 mm from fusion line in as-welded condition

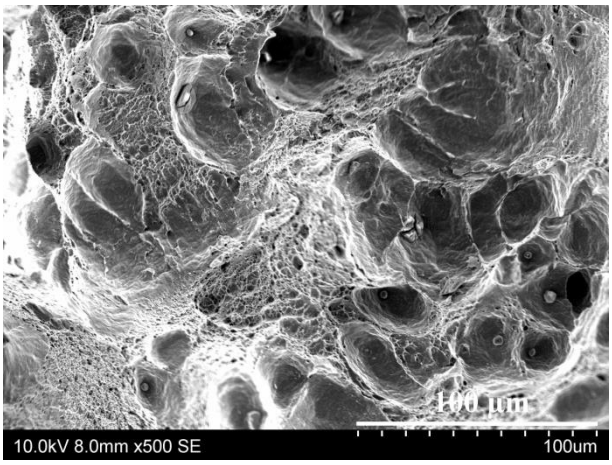

Figure 5-15: SEM micrograph of fracture surface of J_{Ic} test performed at 1 mm from fusion line in heat-treated condition

5.5.2.2 Unstable crack propagation

Unstable crack propagations occurred along the fusion plane in both as-welded and heat-treated conditions. J_{Ic} unstable crack propagation path in heat-treated condition is shown in Figure 5-16. As can be seen in (a), the dimpled rupture is the dominant fracture mode, however, small facets of cleavage fracture were observed. Two cleavage facets of about 80 µm in diameter are shown by the arrows in this figure. In (b), a cleavage facet surrounded by very small dimples is shown at a higher magnification (420X).

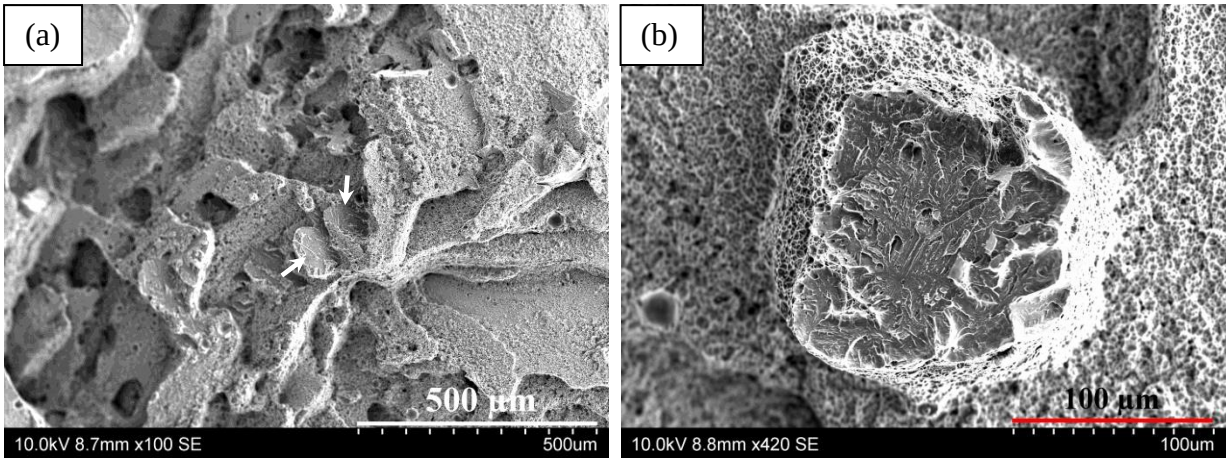

Figure 5-16: SEM micrographs of J_{Ic} unstable crack propagation path on fusion plane in heat-treated condition at (a) 100X and (b) 420X magnifications

A typical region of unstable crack propagation path in heat-treated sample is shown in Figure 5-17. Rupture occurred totally by dimpled rupture. The dimpled rupture appearance was very similar for both as-welded and heat-treated samples. In addition, the unstable crack propagation paths are also very similar to the J_{Ic} fracture surfaces of the weld metals (see section 4.4). The same inclusion types as those existed in the weld metal were detected in this region as well.

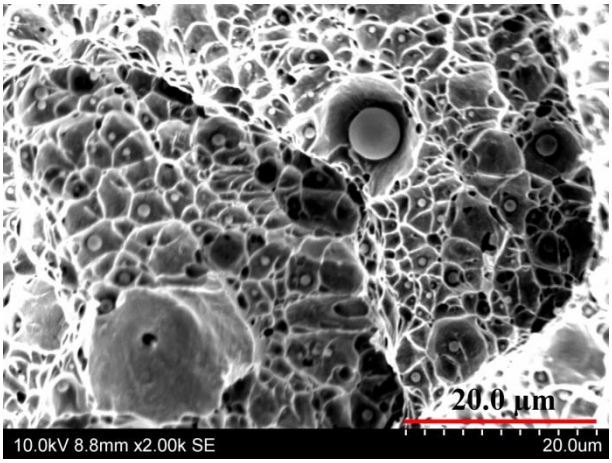

Figure 5-17: Unstable crack propagation fracture surface

Inclusions detected on unstable crack propagation paths of the J_{Ic} tests performed in the HAZ, were of the Si-Mn-Ti-Zr-Cr-rich type for both as-welded and heat-treated conditions. It confirms that the unstable crack propagations took place in the weld metal.

Finally, regarding the microstructural aspect of the unstable crack propagations in the tests performed in the HAZ, it can be argued that the crack deviation toward the weld metal was due to the very sharp differences in the inclusion characteristics existing between the weld metal and the base metals (Table 5-2). More specifically, this can be linked to the very small inclusion spacing in the weld metal, comparing with that in the base metals, as discussed in 5.3.1.

CHAPTER 6 CONCLUSIONS AND RECOMMENDATIONS

To date, there is no complete data base for fracture toughness J_{Ic}, and CVN fracture energy of 13% Cr-4% Ni martensitic stainless steels, especially for the wrought version and the wed metal. The fracture behavior of the HAZ is not examined as well. Additionally, there is no comprehensive research on the effect of the microstructural features including distribution, size, and types of inclusions on the mechanical properties of the cast, the wrought, and the weld metal of 13% Cr-4% Ni martensitic stainless steels. On the other hand, no estimation does exist about the size of TRIP effect region in these stainless steels. Moreover, despite the complex and time-consuming procedure of plane strain fracture toughness measurement, no correlation exists to predict this property by means of CVN fracture energy for this category of stainless steels.

In this study, the J-R curves of a cast, and for the first time in the literature that of a wrought, as well as those of the weld metal (in both as-welded and heat-treated conditions) of 13% Cr-4% Ni martensitic stainless steels were developed and the fracture toughness J_{Ic} values were determined. CVN ductile-brittle transition temperature curves were developed. The main microstructural features of the studied materials were characterized, and in-depth discussions on the relationships between the microstructure and the mechanical properties (tensile, fracture toughness J_{Ic}, and CVN fracture energy) were provided. The spread of the TRIP effect region perpendicular to J_{Ic} crack plane was estimated (in the case of the wrought steel), a precise upper shelf K_{Ic}-CVN correlation was proposed, and the fracture behavior of the HAZ was examined. The major conclusions are:

6.1 Conclusions

- In a general manner, the weld metals have a higher tensile strength but are less ductile than the base metals. The wrought steel has the highest ductility, fracture toughness J_{Ic}, and CVN fracture energy. Overall, the wrought steel has the best combination of strength-ductility/fracture toughness among materials tested in this study. The tensile strength of the weld metals is at least 6% higher, but their ductility is at least 22% lower than the base metals. The ductility, fracture toughness J_{Ic}, and CVN fracture energy of 415 steel are at least 12%, 39%, and 49% higher than those of the tested materials, respectively.

- The fracture occurs by dimpled rupture for the tests performed at room temperature, but some differences existed between the weld metals and the base metals in terms of the MVC mechanism. The growth stage is negligible in the weld metals, and premature micro-void coalescence takes place just after the micro-voids nucleation. In the base metals, nucleated micro-voids grow, and the rupture finally occurs by their coalescence. The growth of the nucleated micro-voids led to the higher ductility, fracture toughness K_{Ic}, and CVN fracture energy of the base metals by at least 27%, a factor of 2, and a factor of 3, respectively.
- The fracture modes for low temperature CVN tests are a mix of dimples and cleavage, and pure cleavage for both the base metals and the weld metals. The base metals absorb the same fracture energies, whereas the heat-treated weld metal absorbs higher fracture energies until -150 °C.
- As compared to the wrought steel, the inclusion size measured on fracture surfaces is at least three times larger in the cast steel. For this cast steel, the majority of inclusions detected on fracture surfaces of tensile, J_{Ic}, and CVN tests were larger than 10 µm. On the contrary, almost all the inclusions on the wrought steel fracture surfaces had diameters smaller than 10 µm. However, inclusions observed on fracture surfaces of tensile, fracture toughness J_{Ic}, and CVN tests of the weld metals, had nearly the same size.
- Si/Mn-rich and Al-rich complex inclusions are the two main types of defects detected on the fracture surfaces of the cast and the wrought steels, respectively. On the other hand, Si-Mn-Ti-Zr-Cr-rich complex inclusions were detected on the weld metal fracture surfaces.
- Many Si/Mn-rich inclusions were found to be ruptured, whereas Al-rich inclusions (only found in the wrought steel) were found to be intact in the case of the wrought steel. Some ruptured Si-Mn-Ti-Zr-Cr-rich inclusions were also observed on the weld metal fracture surfaces. The Al-rich inclusions seem to have the highest resistance against rupture. Ruptured Si/Mn-rich inclusions and those having diameters larger than 10 µm are the main sites of micro-void nucleation in the cast steel. Inversely, micro-voids nucleate from intact Al-rich inclusions (which are almost always smaller than 10 µm in diameter) in the

case of the wrought steel. Both large inclusions and small ones were the nucleation sites for micro-voids formation.

- Heat treating at 600 °C for two hours is a way to obtain a good combination of strength/ductility and fracture toughness for the weld metal; uniform elongation and elongation at fracture were increased by 45% and 55%, respectively. The fracture toughness J_{Ic} is improved by a factor of two, while the yield strength is decreased only by 2%. In addition, the CVN fracture energy is also improved by 56%.
- Similar crack growth behaviors are observed between the as-welded and the heat-treated weld metals, as well as between CA6NM and 415 steels. However, the weld metals and the base metals show different behaviors against crack growth. As compared to the base metals, the J-R curve reaches a quasi-plateau for crack extensions larger than about 0.5 mm, whereas it continues to increase significantly until the final crack extension in the base metals.
- As compared to the base metals, the surface density and the volume fraction of inclusions are at least 800 times and 5 times higher for the weld metal, respectively. However, its inclusion size and inclusion spacing are at least 9 times and 19 times lower, respectively. These significant differences are thought to be the major reasons for the sharp decreases of the fracture toughness J_{Ic} and tearing modulus of the weld metals.
- The higher ductility, fracture toughness, and CVN fracture energy of the wrought steel seem to be related to its lower inclusion volume fraction, and a more resistant inclusion type (Al-rich) against rupture and against micro-void formation.
- Among inclusion characteristics, the very low inclusion spacing of the weld metal (as compared to the base metals) is the key parameter that makes decrease ductility and fracture toughness.
- At the crack tip in a J_{Ic} specimen, the spread of the zone where the TRIP effect occurs in the wrought steel is about 6 mm in a direction perpendicular to the fracture surface. Outside this zone, the strains are not high enough to transform the austenite into martensite.

- Fracture toughness (K_Q) of the tests performed in the HAZ was higher than that of the weld metals, but lower than that of the base metals. Unstable crack propagation toward the weld metal occurred just after a stable crack growth of about one millimeter. Their stable crack growth resistance was similar to that of the weld metal.
- A K_{Ic}-CVN correlation is proposed for 13% Cr-4% Ni martensitic stainless steels. This correlation is obtained simply by plotting K_{Ic} values versus CVN fracture energies fitting a non-linear regression curve to the data points. Wide ranges of fracture toughness K_{Ic} and CVN fracture energies are covered, and precise fracture toughness K_{Ic} is predicted for these steels.
- Based on the results obtained from J_{Ic} testing of the base metals, the weld metals, and the HAZ, it can be said that the most critical area in terms of unstable crack propagation in a welded joint is the weld metal rather than the HAZ.

6.2 Recommendations

As a general recommendation to consider in the choice of 13% Cr-4% Ni martensitic stainless steels, it is recommended to use the steels with the lowest inclusion volume fraction. The distribution of inclusions is also important, and steels with the smallest size and the largest spacing of inclusions get the first priority.

Cracks located in the HAZ, especially the ones located in the vicinity of the fusion line are very dangerous, and shall be avoided; if these cracks start to grow, a total breakdown of the in-operation component could suddenly take place. This is due to the fact that the fracture toughness of the weld metal is much less than that of the base metal. A way to resolve this problem is to improve the fracture toughness of the weld metal.

Post weld heat treatment at 600 °C for two hours is highly recommended as it improves significantly the fracture toughness and the resistance against crack growth while keeping high yield and tensile strengths. Accordingly, the critical crack length needed for unstable propagation increases. Generally, the whole turbine runner is heat treated before the first launch. However, the turbine runner is directly used after each reparation process without having undergone any heat treatment. Therefore, catastrophic crack propagations are risky in this case, and heat treatment after reparation is particularly recommended as well.

BIBLIOGRAPHY

[1] S. Antolovich, "Alloy Design for Fatigue and Fracture," in *ASM Handbook.* vol. 19, ed: ASM International, 1996, pp. 27-41.

[2] P. Bilmes, C. Llorente, and J. Pérez Ipina, "Toughness and Microstructure of 13Cr4NiMo High-Strength Steel Welds," *Journal of Materials Engineering and Performance,* vol. 9, pp. 609-615, 2000.

[3] P. Bilmes, M. Solari, and C. Llorente, "Characteristics and effects of austenite resulting from tempering of 13Cr-NiMo martensitic steel weld metals," *Materials characterization,* vol. 46, pp. 285-296, 2001.

[4] W. M. Garrison Jr, "Controlling inclusion distributions to achieve high toughness in steels," *Iron & steel technology,* vol. 4, pp. 132-139, 2007.

[5] D. Broek, "A study on ductile fracture," TU Delft, Delft University of Technology, 1971.

[6] T. L. Anderson, *Fracture mechanics: fundamentals and applications*: CRC press, 2005.

[7] P. Choudhary and W. M. Garrison Jr, "The Effect of Inclusion Type on the Toughness of 4340 Steel," *Materials and Manufacturing Processes,* vol. 25, pp. 180-184, 2010.

[8] S. Lee, L. Majno, and R. Asaro, "Correlation of microstructure and fracture toughness in two 4340 steels," *Metallurgical Transactions A,* vol. 16, pp. 1633-1648, 1985.

[9] J. Gurland and J. Plateau, "The mechanism of ductile rupture of metals containing inclusions," *Transactions of the ASM,* vol. 56, pp. pp. 442-454, 1963.

[10] W. J. P. Casas, S. L. Henke, and N. Novicki, "Fracture toughness of CA6NM alloy, quenched and tempered, and of its welded joint without PWHT," *Welding International,* vol. 23, pp. 166-172, 2009.

[11] H. K. D. H. Bhadeshia and S. R. Honeycombe, "5 - Formation of Martensite," in *Steels (Third Edition)*, S. R. Honeycombe and H. K. D. H. Bhadeshia, Eds., ed Oxford: Butterworth-Heinemann, 2006, pp. 95-128.

[12] D. A. Porter, K. E. Easterling, and M. Y. Sherif, *Phase transformations in metals and alloys*, 3rd ed. Boca Raton, FL: CRC Press, 2009.

[13] J. C. Lippold and D. J. Kotecki, *Welding metallurgy and weldability of stainless steels*. Hoboken, N.J.: Wiley-Interscience, 2005.

[14] ASM-Handbook, "Selection of cast stainless steels," in *Welding, brazing, and soldering*. vol. 6, ed: ASM-International, 1993, pp. 495-499.

[15] E. Folkhard and G. Rabensteiner, *Welding metallurgy of stainless steels*. Wien ; New York: Springer-Verlag, 1988.

[16] L. Colombier and J. Hochmann, *Aciers inoxydables, aciers réfractaires*, 2e éd. entièrement refondue. -- ed. Paris: Dunod, 1965.

[17] F. B. Pickering, *Physical metallurgy and the design of steels*. London: Applied Science Publishers, 1978.

[18] C. Das, S. Albert, A. Bhaduri, G. Srinivasan, and V. Ramasubbu, "Effect of minor change in composition on toughness of weldmetal for repair of turbine blades made of martensitic stainless steel," *Science and Technology of Welding &# 38; Joining*, vol. 13, pp. 159-166, 2008.

[19] D. Thibault, P. Bocher, M. Thomas, J. Lanteigne, P. Hovington, and P. Robichaud, "Reformed austenite transformation during fatigue crack propagation of 13%Cr–4%Ni stainless steel," *Materials Science and Engineering: A*, vol. 528, pp. 6519-6526, 2011.

[20] A. Trudel, "Étude expérimentale de la propagation de fissures de fatigue dans la zone affectée thermiquement de joints soudés de roues de turbines hydrauliques," École Polytechnique de Montréal, 2013.

[21] R. W. Messler Jr, *Principles of welding: processes, physics, chemistry, and metallurgy*: John Wiley & Sons, 2008.

[22] T. Kannan and N. Murugan, "Effect of flux cored arc welding process parameters on duplex stainless steel clad quality," *Journal of Materials Processing Technology*, vol. 176, pp. 230-239, 2006.

[23] B. Senthilkumar, T. Kannan, and R. Madesh, "Optimization of flux-cored arc welding process parameters by using genetic algorithm," *The International Journal of Advanced Manufacturing Technology*, pp. 1-7, 2014.

[24] B. Senthilkumar and T. Kannan, "Effect of flux cored arc welding process parameters on bead geometry in super duplex stainless steel claddings," *Measurement,* vol. 62, pp. 127-136, 2015.

[25] S. Kou, "Welding metallurgy," *New York,* 1987.

[26] D. Carrouge, "Phase transformations in welded supermartensitic stainless steels," University of Cambridge, 2002.

[27] D. Thibault, P. Bocher, and M. Thomas, "Residual stress and microstructure in welds of 13% Cr–4% Ni martensitic stainless steel," *Journal of Materials Processing Technology,* vol. 209, pp. 2195-2202, 2009.

[28] M. Mokhtabad Amrei, "Characterization of microstructure and texture of 13Cr4Ni martensitic stainless steel weld before and after tempering," École de technologie supérieure, 2016.

[29] ASTM-International, "Standard specification for castings, iron-chromium, iron-chromium-nickel, corrosion resistant, for general application," in *A743/A743M,* ed. U.S.A: ASTM International, 2010.

[30] G. V. Voort, G. Lucas, and E. Manilova, "Metallography and microstructures of stainless steels and maraging steels," in *ASM Handbook.* vol. 9, ed, 2004, pp. 670-700.

[31] D. Carrouge, H. Bhadeshia, and P. Woollin, "Effect of δ-ferrite on impact properties of supermartensitic stainless steel heat affected zones," *Science and Technology of Welding and Joining,* vol. 9, pp. 377-389, 2004.

[32] S. Godin, "Effet d'un enrichissement en nickel sur la stabilité mécanique de l'austénite de réversion lorsque soumise à de la fatigue oligocyclique," École de technologie supérieure, 2014.

[33] P. Robichaud, "Caractérisation de la stabilité de l'austénite résiduelle du 415 soumis à un cyclage en fatigue oligocylique," Master's thesis, École de technologie supérieure, Université du Québec, Montréal, 2007.

[34] Y. Iwabuchi, "Factors affecting on mechanical properties of soft martensitic stainless steel castings," *JSME International Journal Series A,* vol. 46, pp. 441-446, 2003.

[35] ASTM-International, "Standard Specification for Steel Castings Suitable for Pressure Service," in *A487/A487M*, ed. U.S.A: ASTM International, 2007.

[36] N. E. Dowling, *Mechanical behavior of materials : engineering methods for deformation, fracture, and fatigue*, 4th ed. Boston ; Montréal: Pearson, 2013.

[37] D. François, "Essai de rupture, essai par choc," *Techniques de l'Ingénieur, traité Matériaux métalliques, M 4 166*, 2007.

[38] J.-P. Baïlon and J.-M. Dorlot, *Des matériaux*, 3e éd. -- ed. [Montréal]: Presses internationales Polytechnique, 2000.

[39] M. A. Meyers and K. K. Chawla, *Mechanical behavior of materials*, 2nd ed. Cambridge: Cambridge University Press, 2009.

[40] R. W. Hertzberg, *Deformation and fracture mechanics of engineering materials*, 4th ed. New York ; Toronto: Wiley, 1996.

[41] ASTM-International, "Standard test method for measurement of fracture toughness," in *E1820 - 11*, ed. U.S.A.: ASTM, 2011.

[42] H. Rogers, "The tensile fracture of ductile metals," *AIME trans*, vol. 218, pp. 498-506, 1960.

[43] R. E. Reed-Hill, *Physical metallurgy principles*, 2d ed. New York: Van Nostrand, 1972.

[44] D. Broek, *Elementary engineering fracture mechanics*, 4th rev. ed. Dordrecht, The Netherlands: Martinus Nijhoff, 1986.

[45] V. Kerlins and A. Phillips, "Modes of fracture," in *ASM Handbook*. vol. 12, ed: ASM International, 1987, pp. 12-71.

[46] N. H. Heo, "Sulfur segregation and intergranular fracture in α-iron," *Scripta Materialia*, vol. 51, pp. 339-342, 8// 2004.

[47] A. Zehnder, "Fracture Mechanics (Lecture Notes in Applied and Computational Mechanics)," ed: Springer, London, 2012.

[48] B. L. Bramfitt, "Effects of composition, processing, and structure on properties of irons and steels," *Materials Park, OH: ASM International, 1997.*, pp. 357-382, 1997.

[49] H. Kitahara, R. Ueji, N. Tsuji, and Y. Minamino, "Crystallographic features of lath martensite in low-carbon steel," *Acta Materialia,* vol. 54, pp. 1279-1288, 3// 2006.

[50] S. Morito, H. Tanaka, R. Konishi, T. Furuhara, and T. Maki, "The morphology and crystallography of lath martensite in Fe-C alloys," *Acta Materialia,* vol. 51, pp. 1789-1799, 2003.

[51] F. R. Stonesifer and R. W. Armstrong, "The Physical Metallurgy of fracture," in *Advances in Research on the Strength and Fracture of Materials*. vol. 2A, D. M. R. Taplin, Ed., ed: Pergamon Press, 1977, pp. 1-6.

[52] J. Wang, C. Enloe, J. Singh, and C. Horvath, "Effect of Prior Austenite Grain Size on Impact Toughness of Press Hardened Steel," *SAE International Journal of Materials and Manufacturing,* vol. 9, pp. 488-493, 2016.

[53] J. Aquino, C. Della Rovere, and S. Kuri, "Intergranular corrosion susceptibility in supermartensitic stainless steel weldments," *Corrosion Science,* vol. 51, pp. 2316-2323, 2009.

[54] D. Kotecki, "Welding of stainless steels," *ASM International, ASM Handbook.,* vol. 6, pp. 677-707, 1993.

[55] L. Schäfer, "Influence of delta ferrite and dendritic carbides on the impact and tensile properties of a martensitic chromium steel," *Journal of nuclear materials,* vol. 258–263, Part 2, pp. 1336-1339, 1998.

[56] Y. Iwabuchi and I. Kobayashi, "A study of toughness degradation in CA6NM stainless steel," *Materials Science Forum,* vol. 654-656, pp. 2515-2518, 2010.

[57] D. Webster, "Optimization of strength and toughness in two high-strength stainless steels," *Metallurgical Transactions,* vol. 2, pp. 1857-1862, 1971.

[58] F. Huang and D. Gelles, "Influence of specimen size and microstructure on the fracture toughness of a martensitic stainless steel," *Engineering Fracture Mechanics,* vol. 19, pp. 1-20, 1984.

[59] S. D. Antolovich and B. Singh, "Observations of martensite formation and fracture in TRIP steels," *Metallurgical and Materials Transactions B,* vol. 1, pp. 3463-3465, 1970.

[60] A. A. Griffith, "The phenomena of rupture and flow in solids," *Philosophical transactions of the royal society of london. Series A, containing papers of a mathematical or physical character,* vol. 221, pp. 163-198, 1921.

[61] T. Cox and J. R. Low, "An investigation of the plastic fracture of AISI 4340 and 18 Nickel-200 grade maraging steels," *Metallurgical Transactions,* vol. 5, pp. 1457-1470, 1974.

[62] D. Firrao and R. Roberti, "Interrelation among microstructure, crack-tip blunting, and ductile fracture toughness in mild steels," in *Advances in fracture research* vol. 2, ed. New Delhi, India, 1984, pp. 1311-1319.

[63] J. R. Rice and D. M. Tracey, "On the ductile enlargement of voids in triaxial stress fields∗," *Journal of the Mechanics and Physics of Solids,* vol. 17, pp. 201-217, 1969.

[64] Y. Huang, "Accurate dilatation rates for spherical voids in triaxial stress fields," *Journal of Applied Mechanics,* vol. 58, pp. 1084-1086, 1991.

[65] D. François, "Essais de mesure de la ténacité, Mécanique de la rupture," *Techniques de l'Ingénieur, traité Matériaux métalliques, M 4 166,* 2007.

[66] K. Wallin, "A simple theoretical Charpy V-KIc correlation for irradiation embrittlement," *Technical research center of Finland (VTT), Metals laboratory,* 1989.

[67] D. Norris, J. Reaugh, and W. Server, "A fracture-toughness correlation based on Charpy initiation energy," in *Fracture mechanics: Thirteenth conference, ASTM STP 743,* 1981, pp. 207-217.

[68] J. Barsom and S. Rolfe, "Correlations Between KIc and Charpy V-Notch Test Results in the Transition Temperature Range," *Impact Testing of Metals, ASTM STP 466,* pp. 281-302, 1970.

[69] S. Rolfe and S. Novak, "'Slow Bend KIc Testing of Medium Strength High Toughness Steels," *ASTM STP 463,* pp. 124-159, 1970.

[70] J. Begley and P. Toolin, "Fracture toughness and fatigue crack growth rate properties of a Ni-Cr-Mo-V steel sensitive to temper embrittlement," *International Journal of Fracture,* vol. 9, pp. 243-253, 1973.

[71] T. Iwadate, T. Karaushi, and J. Watanabe, "Prediction of fracture toughness KIc of 21/4 Cr-1Mo pressure steels from Charpy V-notch test results," *ASTM STP 631*, pp. 493-506, 1977.

[72] R. Ault, G. Wald, and R. Bertolo, "Development of an Improved Ultra-High Strength Steel for Forged Aircraft Components," Defense Technical Information Center Document1971.

[73] P. N. Thorby and W. G. Ferguson, "Fracture toughness of HY60 steel," *Transactions of the New Zealand Institution of Engineers*, vol. 2, p. 185, 1975.

[74] H. J. Schindler, "Relation between fracture toughness and Charpy fracture energy: An analytical approach," *ASTM special technical publication*, vol. 1380, pp. 337-353, 2000.

[75] K. Wallin, P. Nevasmaa, T. Planman, and M. Valo, "Evolution of the Charpy-V test from a quality control test to a materials evaluation tool for structural integrity assessment," *European Structural Integrity Society*, vol. 30, pp. 57-68, 2002.

[76] British-Standard, "Guide to methods for assessing the acceptability of flaws in metallic structures," in *Annex J: Use of Charpy V-notch impact tests to estimate fracture toughness*, ed. England: British Standard, 2005.

[77] ASTM-International, "Standard Specification for Chromium and Chromium-Nickel Stainless Steel Plate, Sheet, and Strip for Pressure Vessels and for General Applications," in *A240/A240M*, ed. U.S.A.: ASTM-International, 2011.

[78] AWS, "Specification for Stainless Steel Flux Cored and Metal Cored Welding Electrodes and Rods," in *A5.22/A5.22M*, ed. U.S.A.: AWS, 2010.

[79] ASTM-International, "Standard Test Methods for Tension Testing of Metallic Materials," in *E8/E8M – 09*, ed. U.S.A.: ASTM, 2009.

[80] ASTM-International, "Standard Test Methods for Notched Bar Impact Testing of Metallic Materials," in *E23 – 07*, ed. U.S.A.: ASTM, 2007.

[81] J. Chen, Y. Verreman, F. Foroozmehr, and J. Lanteigne, "Fracture toughness of 13Cr4NiMo high-strength steels used in hydraulic turbine runners," in *Materials Science and Technology (MS&T) 2013*, Montreal, Quebec, Canada, 2013, pp. 702-711.

[82] J. Chen, Y. Verreman, and J. Lanteigne, "On fracture toughness JIC testing of martensitic stainless steels," in *ICF13*, 2013.

[83] J. Chen, "Finite element analysis of JIc specimens of different geometries," *Private Communication*, 2013.

[84] R. A. Young, "Introduction to the Rietveld method," in *The Rietveld method*, R. A. Young, Ed., ed UK: Oxford University Press, 1993, pp. 1-38.

[85] ASM-Handbook, "Quantitative Characterization and Representation of Global Microstructural Geometry," in *Metallography and Microstructures*. vol. 9, ed: ASM-International, 2004, pp. 428-447.

[86] F. C. Campbell, *Fatigue and fracture: understanding the basics*: ASM International, 2012.

[87] J. L. Maloney and W. M. Garrison, "The effect of sulfide type on the fracture behavior of HY180 steel," *Acta materialia*, vol. 53, pp. 533-551, 2005.

[88] ASTM-International, "Standard test method for linear-elastic plane-strain fracture toughness KIc of metallic materials," in *E399 - 09* ed. U.S.A.: ASTM, 2009.

[89] A. S. M. I. H. Committee, "ASM Handbook, Volume 19 - Fatigue and Fracture," ed: ASM International, pp. 5-14.

[90] M. Paquin, "Essais de fissuration à froid appliqués aux métaux d'apport inoxydables martensitiques 410NIMO," École de technologie supérieure, 2014.

[91] O. Renaud and M.-P. Victoria-Feser, "A robust coefficient of determination for regression," *Journal of Statistical Planning and Inference*, vol. 140, pp. 1852-1862, 2010.

[92] M. E. Magnello, "Chapter 56 - Karl Pearson, paper on the chi square goodness of fit test (1900) A2 - Grattan-Guinness, I," in *Landmark Writings in Western Mathematics 1640-1940*, R. Cooke, L. Corry, P. Crépel, and N. Guicciardini, Eds., ed Amsterdam: Elsevier Science, 2005, pp. 724-731.

APPENDIX A – CUTTING PLAN OF SAMPLES TO BE CUT FROM THE WELD METAL BLOCK

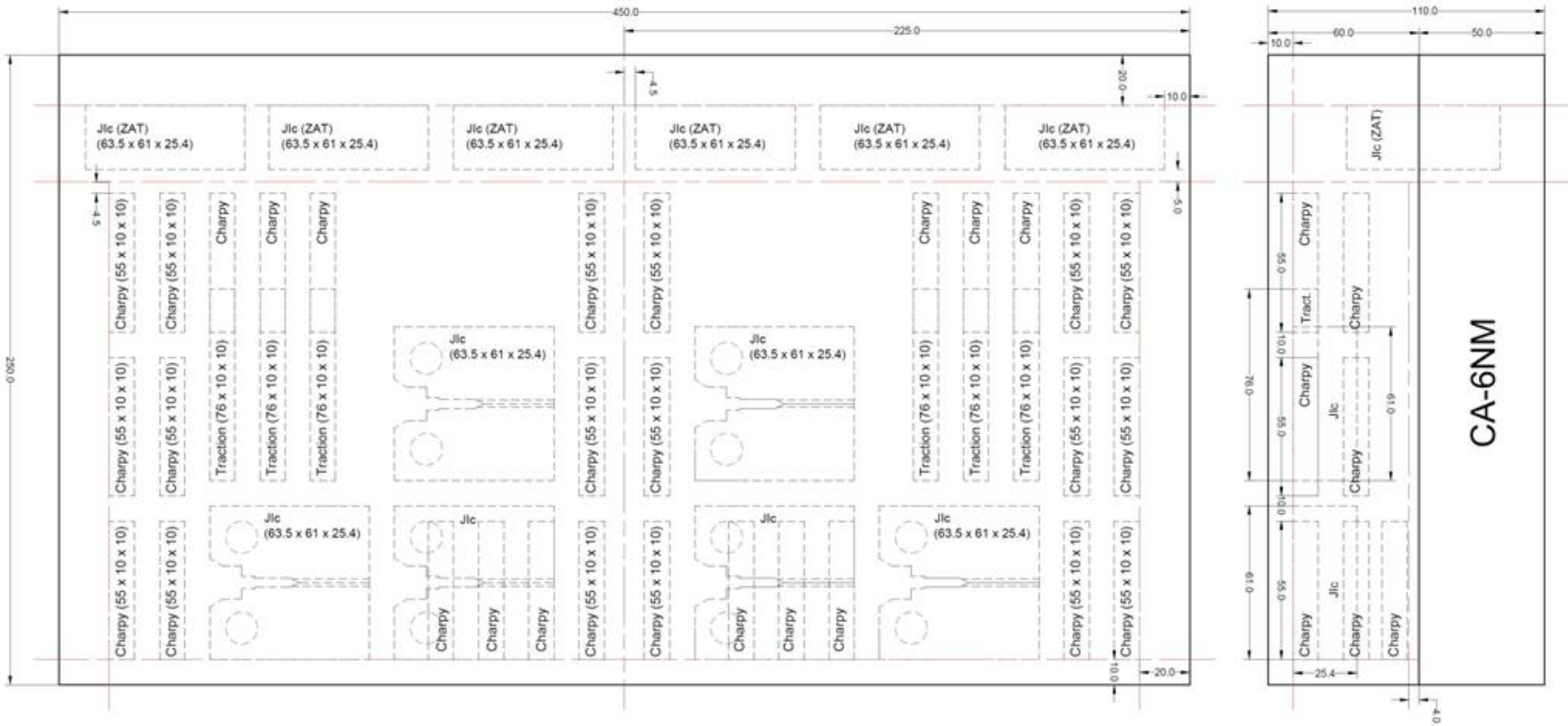

Figure A. 1: Cutting plan of samples to be cut from the weld metal block for both as-welded and heat treated conditions.

APPENDIX B – AUTOMATIC AREAL ANALYSIS OF INCLUSIONS

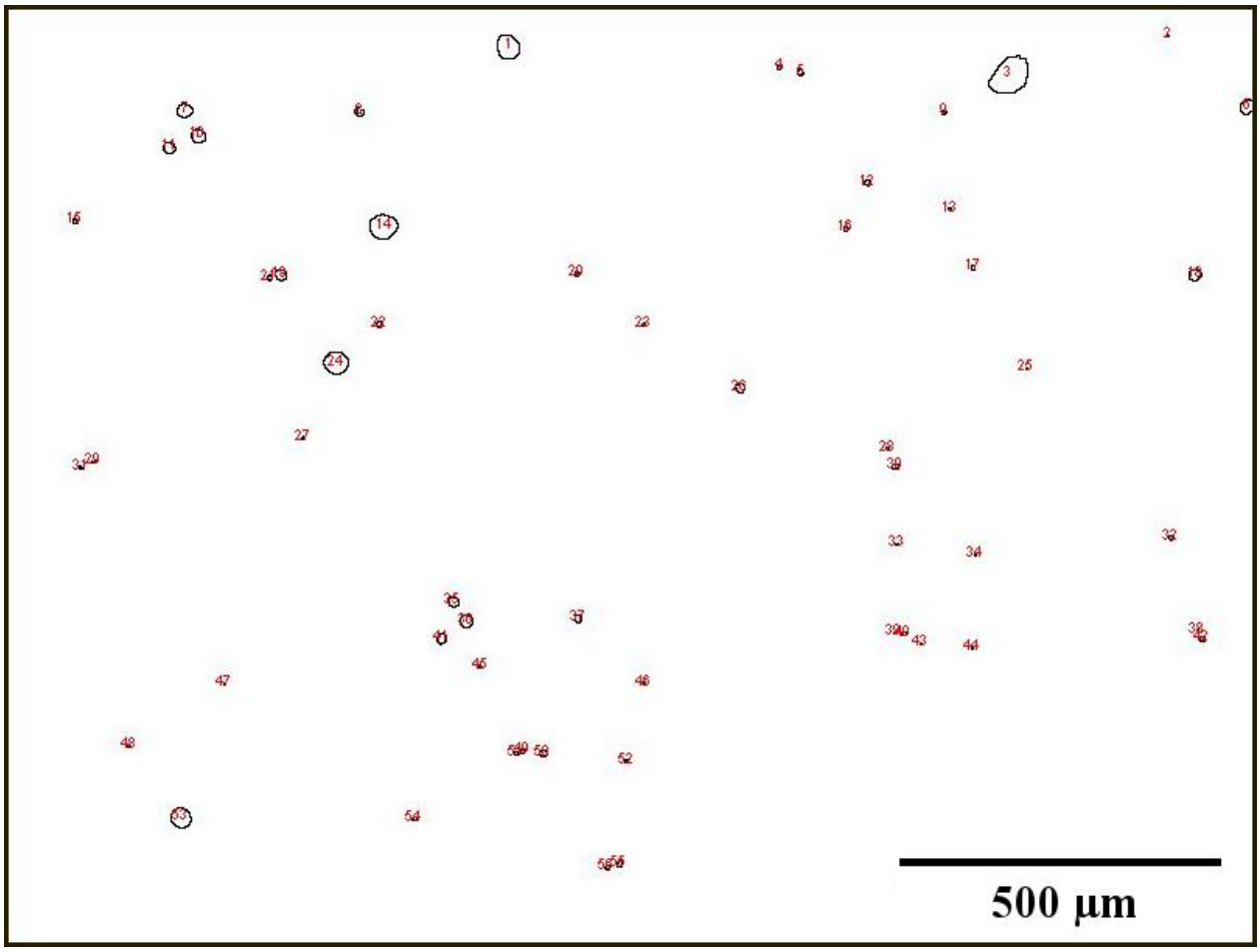

Figure B. 2: Automatic areal analysis of inclusions on CA6NM steel metallographic section. The numbered circles are the measured inclusions.

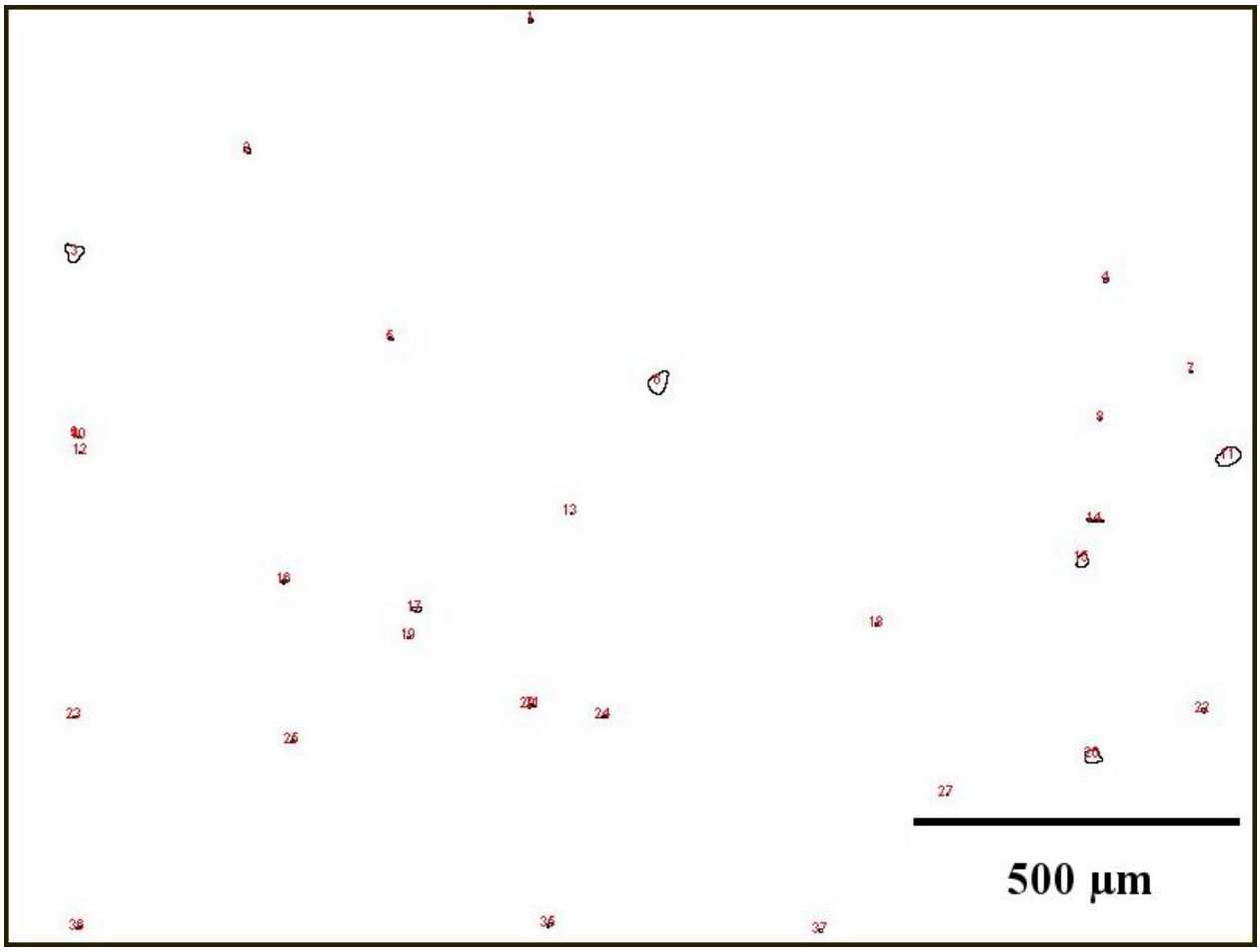

Figure B. 3: Automatic areal analysis of inclusions on 415 steel metallographic section.

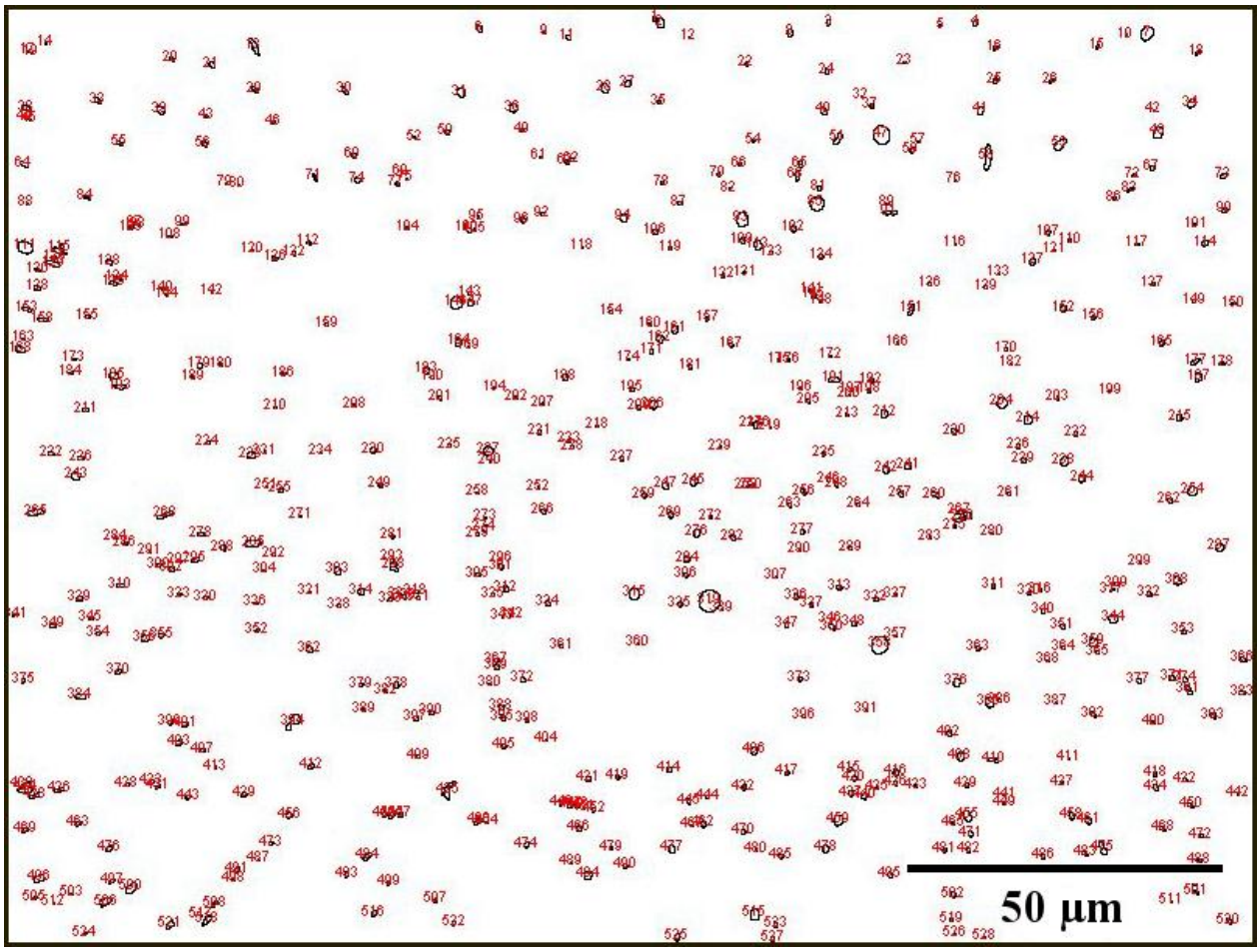

Figure B. 4: Automatic areal analysis of inclusions on 410NiMo steel metallographic section.

APPENDIX C – PRIOR AUSTENITE GRAIN BOUNDARIES

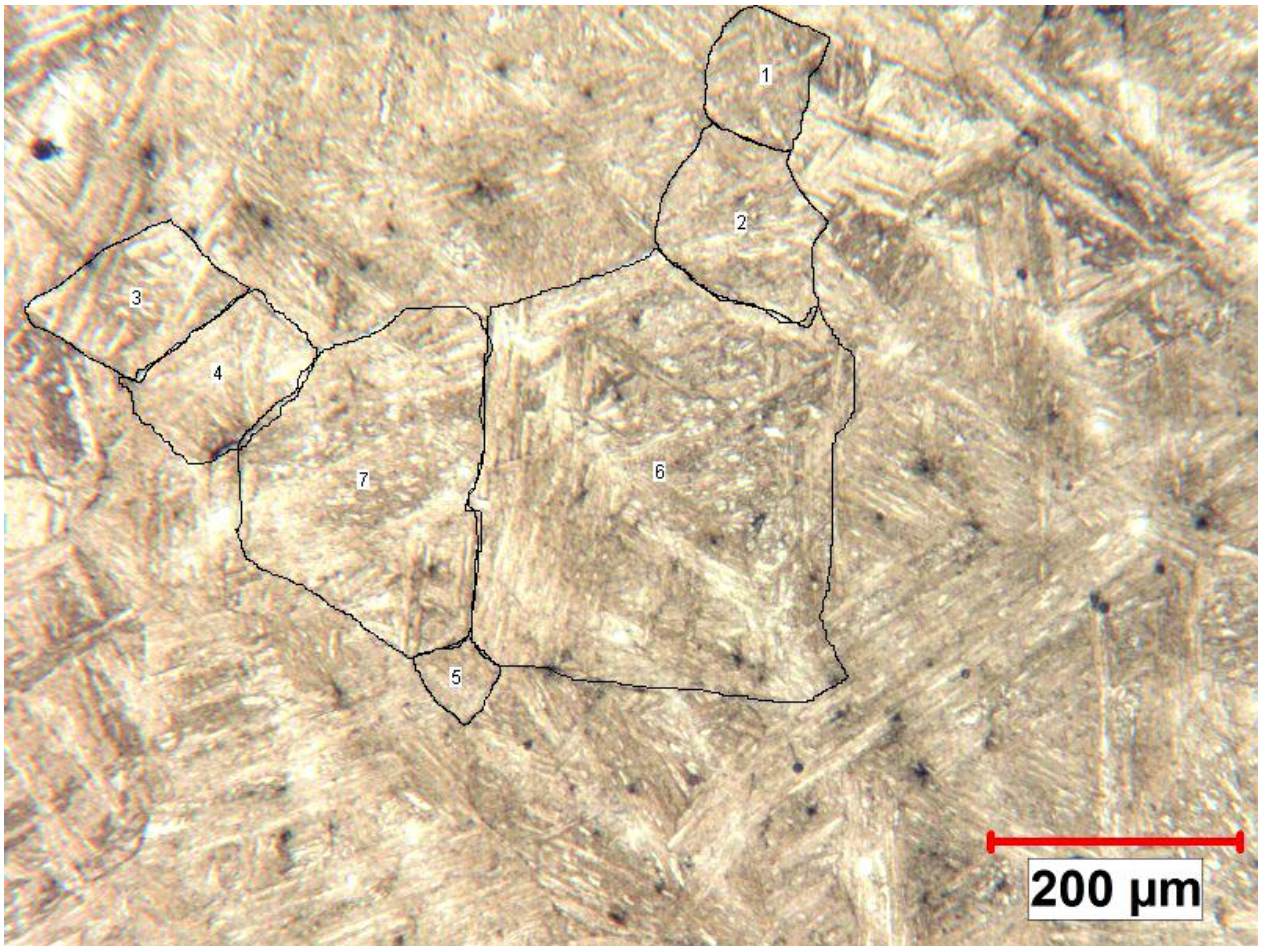

Figure C. 1: Prior austenite grain boundaries revealed in CA6NM steel.

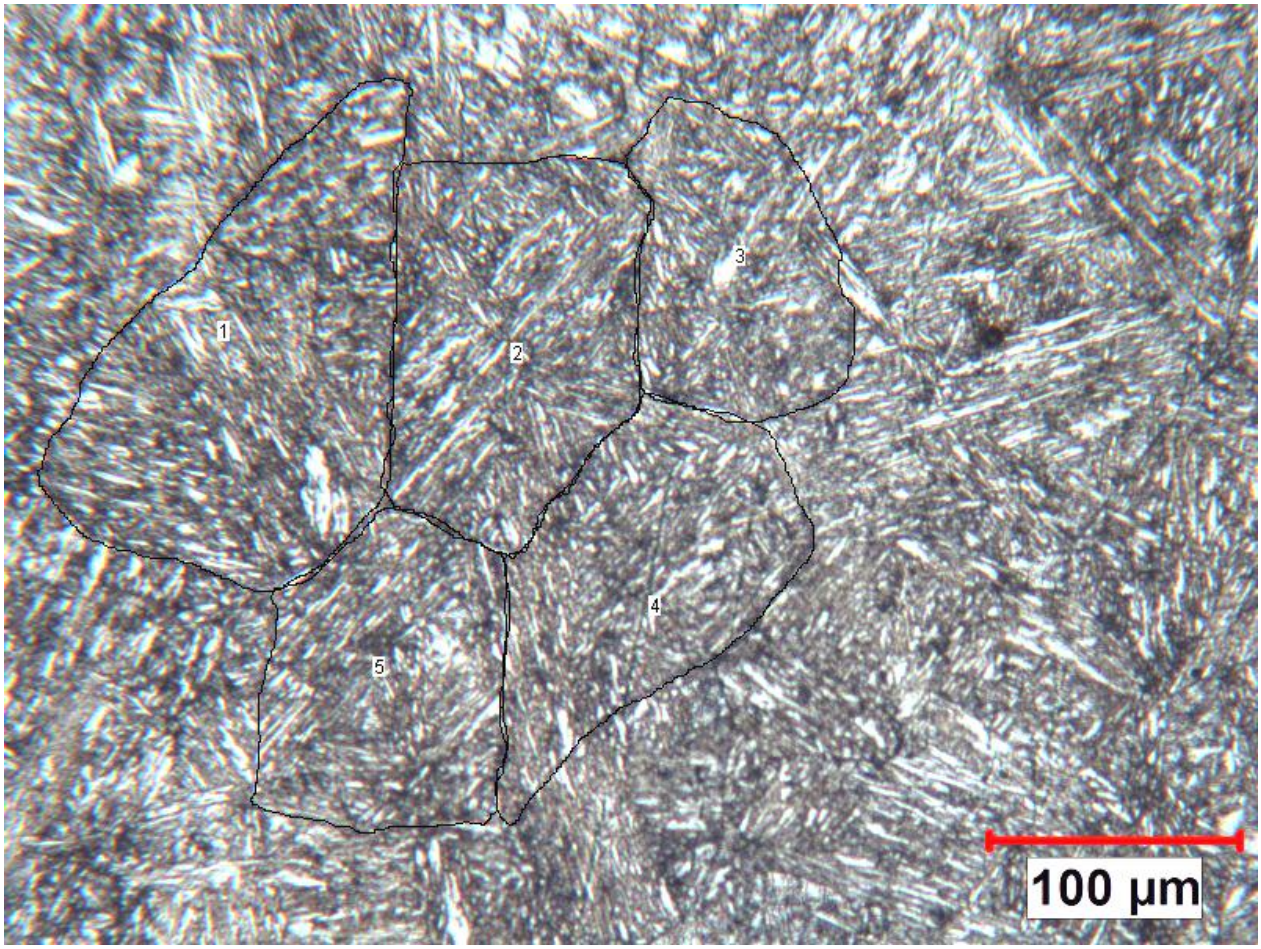

Figure C. 2: Prior austenite grain boundaries revealed in 415 steel (T-S).